Title
Studies on Structures and Dynamics of Polarizable Crystalline Solids

Author
Liu, Zhiyu

Publication Date
2022

Peer reviewed|Thesis/dissertation

UNIVERSITY OF CALIFORNIA

Los Angeles

Studies on Structures and Dynamics of Polarizable Crystalline Solids

A dissertation submitted in partial satisfaction

of the requirements for the degree

Doctor of Philosophy in Chemistry

by

Zhiyu Liu

2022

ABSTRACT OF THE DISSERTATION

Studies on Structures and Dynamics of

Polarizable Crystalline Solids

by

Zhiyu Liu

Doctor of Philosophy in Chemistry

University of California, Los Angeles, 2022

Professor Miguel A. Garcia-Garibay, Chair

Molecular machines have become the focus in field of physical organic chemistry given the advances in synthesis and characterization in recent decades. Identifying motions in molecular machines thus become key knowledge that researchers need in order to design and understand molecular machines. Even though molecular machines such as ATP synthase are universal in nature, designing molecular machines with complex functions remains a great challenge. To achieve such goals, one must explore basic machine functions, such as gearing, translation, locking and rotation, at the molecular level. In this dissertation, rotations are investigated under different scenarios. By virtual of modern solid-state characterization techniques and computer programs, fast rotations of molecular components in several Metal-Organic Frame-

works and molecular crystals have been identified. Such knowledge is necessary to further explore emergent properties in crystalline materials and complex molecular machine functions.

Chapter One is introduction of polarizable amphidynamic crystals, characterization methods, mechanisms and applications.

Chapter Two describes an investigation of an open-pore Zn Metal-Organic Frameworks featuring difluorophenylene dipole and triptycene dicarboxylic acid. After discovering that the Zn MOF cannot maintain its structure upon removal of guest molecules, we sought to explore another more stable MOF system.

Chapter Three describes an air-stable interpenetrated zirconium MOFs with dipoles. Solid-state NMR data and dielectric data are analyzed in depth to reveal the unique dynamics in such system. To further enhance the dipolar self ordering and simplify the structure, a dinitro derivative is also synthesized the results are recorded.

Chapter Four includes the dynamics of a dumb-bell shape tribenzotriquinacene crystalline molecular rotor both experimentally and computationally.

Chapter Five describes explorations on amphidynamic MOFs towards different topologies in order to achieve lattice of lower symmetry or frustrated dipolar array.

The dissertation of Zhiyu Liu is approved.

Philippe Sautet

Richard B. Kaner

Alexander Michael Spokoyny

Miguel A. Garcia-Garibay, Committee Chair

University of California, Los Angeles

2022

To my family and Bei...

who gave me guidance, support and love through this long journey

TABLE OF CONTENTS

LIST OF FIGURES

LIST OF TABLES

LIST OF SCHEMES

ACKNOWLEDGMENTS

First of all, I am deeply grateful to my advisor Prof. Miguel Garcia-Garibay. The first week I joined the group, I was surprised by the energy he devotes into projects of everyone despite his duty as Dean. Miguel always encourages us to think critically and provides his insight and expertise whenever needed. I feel extremely fortunate to conduct research in his group where I can explore things freely without limitations. To me, Miguel is not only a respected scientist and a knowledgeable advisor, but also a role model in many aspects. He is a patient, compassionate and positive person who I always look up to.

I want to thank my committee members, Prof. Richard Kaner, Prof. Phillipe Sautet and Prof. Alex Spokoyny for advices and reviewing my dissertation. I am thankful to the guidance Prof. Sautet gave me on how I could start doing DFT computation with almost zero background. It not only enabled me to make progress at home but also expanded the scope of my research and interest. I was fortunate to be in Prof. Kaner's Solid State Chemistry course. The lectures were both insightful and intriguing. The knowledge has been instrumental in my research. I invited Prof. Spokoyny to my committee in a later stage, I am thankful for his interest in my research and his thoughtful input. It is my pleasure to work with Prof. Louis Bouchard, Prof. Shih-Ching Chuang, Prof. Braulio Rodríguez-Molina Dr. Yangyang Wang and Dr. Erik Leonhardt in graduate school. They are experts in their fields and I learn things from every discussion with them. I am also grateful for mentorship of Prof. Hexiang Deng and Dr. Xiaohui Xu who gave me an opportunity to do research

at Wuhan University. Their passion for science is what lead me to pursue a PhD degree in chemistry.

And my pursuit would not be successful without assistance from many people in UCLA. Therefore, I want to say thank you to Dr. Ta-Chung Ong, Dr. Robert Taylor, Dr. Ignacio Martini, Ricky Ruiz and Jose Gonzalez. They have always been professional and enthusiastic whenever I bring them a problem. I want extend my sincere thanks to my colleagues and friends, Dr. Nanette Jarenwattananon, Dr. Jeffery McCormick, Dr. Edris Rivera, Roberto Chavez, Dr. Guangyan Zhong, Dr. Peiqi Wang, Dr. Ieva Liepuoniute, Dr. Chen Zhang, Dr. Trevor Chang, Tiange Chen, Bohan Zhang, Yulong Chen, Yucong Wei, Dr. Weilai Yu, Dr. Marcus Jellen, Dr. Ruxi Dai for their friendship and support.

Both being teachers in school, my parents, Hongbo Pang and Pengfei Liu, take my education seriously and foster me to be a person who I am. It is hard to find words to express my gratitude to their tremendous sacrifice and wholeheartedly love. My grandparents also gave me unwavering trust and support since I was a kid. Although I may never know how emotionally difficult it is for them to be thousands of miles away from their only son/grandson for years, their love is always my motivation in graduate school and the path ahead. I am so lucky to have my love, Bei Luo, in my life. Through all the years we spent together, Bei gave me endless motivation, trust, inspiration and love, to which I am grateful forever.

Chapter Two describes unpublished studies.

Chapter Three includes Liu, Z., Wang, Y., Garcia-Garibay, M. A., 2021."Rota-

tional Dynamics of an Amphidynamic Zirconium Metal-Organic Frameworks Determined by Dielectric Spectroscopy". *Journal of Physical Chemistry Letters*, 12(24): 5644-5648. and unpublished materials in collaboration with Rodríguez-Molina.

Chapter Four is a manuscript in preparation by Liu, Garcia-Garibay and Chuang.

Chapter Five describes unpublished studies in collaboration with Leonhardt.

VITA

2012–2016 Bachelor of Science in Chemistry, Wuhan University, Wuhan, China.

2016–2022 Department of Chemistry, University of California, Los Angeles, Los Angeles, California.

PUBLICATIONS

1. Liu, Z., Raju, S., Chen,C. Y., Chuang, S. C., Garcia-Garibay, M. A., Rotational dynamics of tribenzotriquinacene-capped dumbbell-shaped phenylene rotors. In manuscript.

2. Liu, Z., Wang, Y., Garcia-Garibay, M. A., 2021. Rotational dynamics of an amphidynamic zirconium Metal- Organic Framework determined by dielectric spectroscopy. *The Journal of Physical Chemistry Letters*, 12, pp.5644-5648.

3. McCormick, J., Korchak, S., Mamone, S., Ertas, Y.N., Liu, Z., Verlinsky, L., Wagner, S., Glöggler, S. and Bouchard, L.S., 2018. More than 12% polarization and 20-minute lifetime of 15N in a choline derivative. utilizing parahydrogen and a rhodium nanocatalyst in water. *Angewandte Chemie*, 130(33), pp.10852-10856.

4. Xu, X., Li, S., Liu, Q., Liu, Z., Yan, W., Zhao, L., Zhang, W., Zhang, L., Deng, F., Cong, H. and Deng, H., 2018. Isolated *pi*-interaction sites in mesoporous MOF

backbone for repetitive and reversible dynamics in water. *ACS Applied Materials & Interfaces*, 11(1), pp.973-981.

5. Zhou, L., Lu, H. and Liu, Z., 2016. Mechanism and dynamic thermomechanical analysis of ZIF-61/bisphenol- A cyanate ester (BCE) composites. *Materials Letters*, 175, pp.48-51.

CHAPTER 1

Introduction

1.1 Amphidynamic Crystals

An amphidynamic crystal is a class of crystals with components undergoing fast motion in a highly ordered crystalline environment.[1] Due to internal motions of certain components, amphidynamic crystals possess more degrees of freedom than classic solid state crystals. In amphidynamic crystals, locations and surroundings of motions can be mapped out from crystal structure. Therefore the structure-performance relation can be predicted and analyzed. Also, the ordered structure also provides convenience to computational analysis. The combination of rigidity and fluidity makes amphidynamic crystals interesting systems to study molecular machines and functional materials.

Among all types of motions in molecular machine, rotation is a basic mechanism to achieve more complex functions. In a typical rotor-stator system, the stator is considered the frame of reference while the rotor undergoes thermally activated rotational motion. For example, a 1,4-bisethynylphenylene in molecular crystals can function as rotor and the triple bonds provide the axis of rotation. The rotor-stator

connection can also be noncovalent as seen in hydrogen-bonded co-crystals with amphidynamic properties. Moreover, when the mobile components behave collectively in an ordered arrangement, more phenomena or emergent properties such as ferromagnetism[2], acoustic[3], photoluminescence[4] and dielectric properties[5], [6] will occur.

Over the years, the Garcia-Garibay group and others have studied a series of amphidynamic crystals that featured engineered dynamics in solid state[7]–[9]. The dynamics of rotors are investigated both experimentally and computationally. Obviously, open volume is needed to enable fast rotations in amphidynamic crystals, therefore crystals with bulk stator groups have been investigated due to their preferred low-density packing.[10] Besides low-density packing, porous materials such as Metal-Organic Frameworks are promising candidates.

1.2 Amphidynamic Metal-Organic Frameworks

MOFs have been proved to be an excellent platform for applications in gas storage, drug delivery, catalysis, photochemistry, water purification and many other fields.[11] Additionally, the porosity in the ordered structure and variabilities in the constituting ligand or metal bring numerous possibilities to rotor systems.

Specifically, one can incorporate field-responsive dipoles into ligand and adjust the their spatial arrangement utilizing different topology.[12] The collective behavior of dipoles will reflect dynamics of the crystal. For example, if reorienting strong

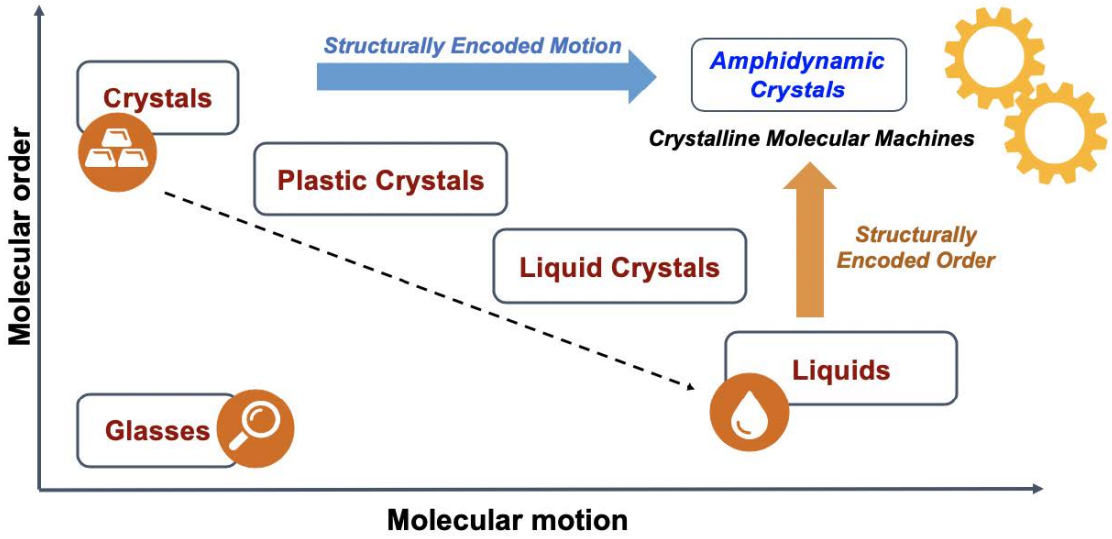

Figure 1.1: Phase order–molecular motion phase diagram illustrating possible forms of condensed-phase matter. Copyright 2020 Royal Society of Chemistry.

electric dipoles (which are often bulky) can freely rotate(low barrier) in open space, a spontaneous ordering could happen thus ferroelectricity will appear. While such reorientation is hindered if the rotation is not volume-conserved in closed-packed crystalline molecular rotors, MOFs could incorporate low-intrinsic-barrier rotary groups in an ordered way and, meanwhile, provide open volume.[13] Such amphidynamic MOFs show promises in achieving precise control over molecular machines.

To investigate amphidynamic MOFs, one need more tools to understand the motion of MOFs components than conventional characterizations for porous materials. An early example reveals dynamic in a classic MOF-5, several NMR techniques are used to confirm the rotation of benzenedicarboxylate.[14] The rotational barrier, as an apparent parameter to describe a dynamic behavior, is modulated by many fac-

tors. Intrinsic barrier has a major influence. The inertia of the rotor fundamentally decides how fast the rotors can rotate. The barrier is also influenced by its bonding environment. As showed in many investigations in Garcia-Garibay group, a triple-bond-linked molecular rotor can have very low energy barrier. Crystal environment can also affect the barrier by steric effect, hydrogen bonding and guest molecules.

For electric dipoles to align collectively in absence of an external field, the dipole-dipole interaction must be greater than thermal barrier(i.e. $E_{DD} > E_a$). This gives us hints on how to approach such inequality. On one hand, the arrangement of stronger dipoles at a proper distance is required, as too small a distance will hinder the rotation. On the other hand, rotary dipoles with lower intrinsic energy barrier are preferred. If RT(when T is room temperature) falls in between E_{DD} and E_a, a room temperature long-range ordering of dipoles will be observed. Furthermore, if the dipoles are arranged in a non-centrosymmetric system, ferroelectricity arising from reorienting dipoles will occur.

1.3 Methods to Study Rotational Dynamics in Crystalline Solids

X-ray diffraction (XRD) analysis gives important structural information for crystalline materials but the XRD data is based on averaged electron density thus only averaged atomic positions are obtained. To probe the dynamics, one needs more tools to understand the dynamics with atomic temporal resolution.

In NMR spectra of solutions, sharp signals are observed because rapid isotropic tumbling averages out the dipolar interactions and chemical shift anisotropy. In solid state, such tumbling is not effective any more and the lines become very broad. Even though information of dipolar coupling strength or chemical shift anisotropy are still accessible from wideline spectra sometimes, special instruments and pulse sequences are still needed to probe structures and dynamics in solid state.

In this section, several solid state NMR techniques and dielectric spectroscopy suitable for investigation of dynamics will be introduced. They are all based on electromagnetic response of the materials to external electric or magnetic field. Therefore, due to distinct response from dipoles/nuclei, their dynamic behaviors can be interpreted. DFT simulations are also discussed as they are a fast-developing powerful tool to simulate wide range of dynamics without limitations of the aforementioned instruments.

1.3.1 CPMAS Solid State NMR

Early-stage studies on solid state NMR focused on proton or fluorine relaxation time. Andrew and Lowe showed that by spinning the sample at a certain angle(MAS, magical angel spinning) to the main field, the dipolar interactions are suppressed and chemical shift anisotropy is averaged thus a sharp line can be observed.[15]

In a solid state NMR experiment, Hamiltonian of a non-quadrupolar spin can be described as sum of chemical shielding Hamiltonian H_{CS}, truncated heteronuclear

dipolar couplings Hamiltonian H_{D}^{IS}, and truncated homonuclear dipolar couplings Hamiltonian H_{D}^{II}:

$$H = H_{CS} + H_{\mathrm{D}}^{IS} + H_{\mathrm{D}}^{II} \tag{1.1}$$

$$H_{\mathrm{CS}} = \left\{ \sigma_{\mathrm{iso}} \gamma B_0 + \frac{1}{2}\delta \left[3\cos^2\theta - 1 - \eta \sin^2\theta \cos(2\phi) \right] \right\} I_z \tag{1.2}$$

$$H_{\mathrm{D}}^{IS} = -\frac{\mu_0}{4\pi}\hbar \sum_i \sum_j \frac{\gamma^I \gamma^S}{r_{ij}^3} \frac{1}{2} (3\cos^2\theta_{ij} - 1) 2 I_z^i S_z^j \tag{1.3}$$

$$H_{\mathrm{D}}^{II} = -\frac{\mu_0}{4\pi}\hbar \sum_i \sum_j \frac{\gamma^2}{r_{ij}^3} \frac{1}{2} (3\cos^2\theta_{ij} - 1)(3 I_z^i I_z^j - \mathbf{I}^i \cdot \mathbf{I}^j) \tag{1.4}$$

where σ_{iso} is the isotropic value, δ is the anisotropy, and η is the asymmetry parameter, γ is gyromagnetic ratio. I represents abundant spins, S represents dilute spins. r_{ij} is the magnitude of the distance vector $\mathbf{r}_{ij}$ between the nuclei i and j, andθ_{ij} is the angle between r_{ij} and the z-axis. Note that All three Hamiltonians share a factor $(3\cos^2\theta_{ij} - 1)$. This means when the sample is spun at $54.74°$(magic angle spinning, $3\cos^2\theta_{ij} - 1 = 0$) and the spin rate is fast enough, all anisotropic interactions are averaged thus sharp-line spectra can be obtained.

Magic angle spinning(MAS) technique is often used together with ^{1}H-^{13}C cross polarization(CP). The reason is two-fold. Strong proton homonuclear coupling ,which is common in organic/polymer samples, still significantly broaden spectral lines. On the other hand, NMR sensitivity of ^{13}C is intrinsically low due to low natural abundance and extremely long relaxation times. However, ^{13}C spectra are still needed to provide important structural information. Cross polarization can transfer ^{1}H magnetization to ^{13}C (or other nuclei) when the Hartmann-Hahn condition is satisfied.[16]

The Hartmann-Hahn condition is described as:

$$\gamma_{\mathrm{H}} B_{1,\mathrm{H}} = \gamma_{\mathrm{C}} B_{1,\mathrm{C}}, \tag{1.5}$$

where B_1 represents rf pulse strength. During a Hartmann-Hahn echo, rf pulses for ^{1}H and ^{13}C are turned on simultaneously and the ratio between them is equal to the inverse ratio of their gyromagnetic ratio. The duration when both rf pulses are turned on is called contact time. It can range from 1 to 10 ms. It is important to find optimal contact time for each experiment. Cross polarization builds up fast at the beginning of contact. However, if contact time is set too long, magnetization starts to lose due to ^{1}H $T_1\rho$. Additionally, a long pulse at high power can damage circuits. It should also be noted that protonated carbons benefit more from CP process than quaternary carbons. Such a phenomenon is observed in studies of Chapter Four.

The variable temperature ^{1}H-^{13}C CPMAS technique can be used to probe dynamics at the range of 0.1 to 10 kHz based on change in chemical shifts between 'frozen' state and thermally activated state. Therefore the change is only observed for fairly slow motions with high barriers (>10 kcal/mol). However, it still provides important information because the sharp carbon signals can be accurately assigned with high power proton decoupling.

Dipolar dephasing pulse sequences are commonly used to assign peaks in solid state CPMAS experiment.[17] In the pulse sequence, a delay is placed between the end of contact time and acquisition (Figure 1.2). Given a proper delay, carbons with strong dipolar coupling to protons will decay while signals of weakly coupled carbons remain. Moreover, dipolar coupling can also be averaged by the fast rota-

tion. Therefore, dipolar dephasing technique can also be used to give preliminary information on molecular motion along with chemical shift.

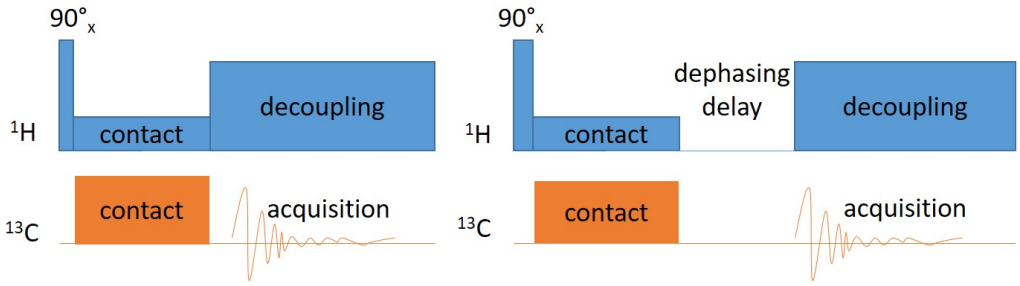

Figure 1.2: Pulse sequences of a regular CPMAS pulse sequence(left) and a dipolar dephasing CPMAS(right).

1.3.2 Deuterium Quadrupolar Lineshape Analysis

Quadrupolar nuclei have spin>1/2. Unlike spin-1/2 nuclei, which have spherical distributions of electric charge, quadrupolar nuclei possess asymmetric distributions of charge. As advances in electronics make higher power pulse more available, the information hidden in the complicated quadrupolar interaction is better understood by researchers.[18], [19] Among many quadrupolar nuclei, deuterium is the most studied for many reasons. First, hydrogen exists in so many compounds that a selective deuteration can be very informative. In studies such as organic ferroelectrics, deuterium ssNMR become a perfect tool to reveal structural origin of ferroelectricity as deuterium has different hydrogen bonding behaviors. Second, it is the most available isotope for researchers. At a reasonable cost, one can selectively deuterate certain positions during the synthesis and get information of C-D motions that are

otherwise indifferent to all other C-H motions. Most importantly, these are made possible by the intrinsic property of deuterium. Static quadrupole coupling constant of deuterium falls between 150 and 200 kHz. It is greater than dipole-dipole coupling and chemical shift anisotropy so the effects of local motion can be studied without interference from those two mechanisms, while the entire frequency range is still accessible by standard high power NMR pulse sequences.[20]

When a deuterium nucleus experiences an external magnetic field B_0, it undergoes a nuclear Zeeman spiltting and its energy level becomes nondegenetrate (+1, 0 and -1). The energy gap ΔE is proportional to the filed strength:

$$\Delta E = -\frac{h}{2\pi}\gamma B_0, \tag{1.6}$$

where γ is called gyromagnetic ratio and is a characteristic value for isotopes(for deuterium, $\gamma_D = 6.536$ MHz/T). Interaction between electric field gradient(EFG) of the quadrupolar nuclei and B_0 will further shift the energy levels so that two transitions can be observed. The frequency of resonance of deuterium in the absence of molecular motion under first perturbation regime is given by

$$\nu_Q = \pm\frac{3}{8}\frac{e^2qQ}{h}(3\cos^2\theta - 1 - \eta\sin^2\theta\cos 2\psi) \tag{1.7}$$

where e is the electron charge, Q is the nuclear quadrupole moment, $\frac{e^2qQ}{h}$ is usually referred as Quadrupole Coupling Constant(Q_{CC}). θ and ψ are the polar and azimuthal angles of the C-D vector with respect to B_0 in the principal axis frame (PAS). asymmetry parameter η is equal to $\frac{(\partial^2V/\partial^2X)_0-(\partial^2V/\partial^2Y)_0}{(\partial^2V/\partial^2Z)_0}$, V being EFG tensor in PAS, X,Y,Z being three axis in PAS. η is a number usually less than 0.1.

The quadrupole frequency is dependent on spin orientations. For an amorphous powder sample, the observed spectrum has contributions from all orientations and typically shows a classic Pake pattern. The most statistically probable orientation is perpendicular to magnetic field ($\theta = 90°$) therefore its intensity is highest.The shoulders of the pattern is when the principal axis of the nuclei is aligned with magnetic field($\theta = 0°$), which is the least probable situation.

In presence of rapid molecular motion, one can imagine that the previous distribution of orientations would change. In fact, the lineshape is modified by reduced EFG tensor depending on the rate of reorientation and the orientations of the principal axes of the EFG tensor relative to the rotation axis.

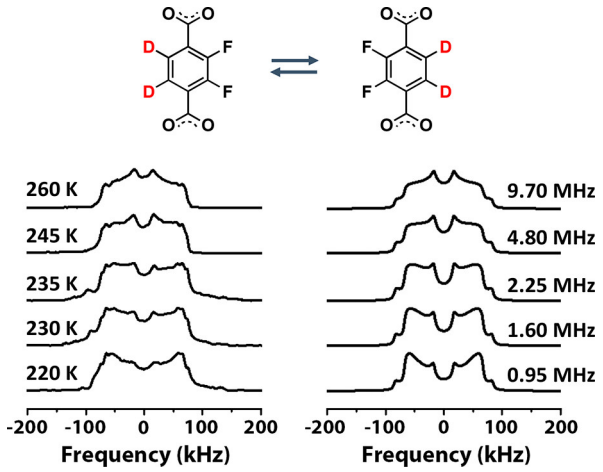

Figure 1.3: (left) Experimental 2H NMR quadrupolar echo spectra and (right) spectra simulated assuming rotational trajectories for the phenylene group of 180° jumps. Reprinted with permission from J. Phys. Chem. C 2020, 124, 28, 15391–15398. Copyright 2020 American Chemical Society.

By comparing experimental lineshape with simulated lineshape. They molecular

motion at rates 10^3-10^7 can be characterized. One example from previous research of our group can be seen in Figure 1.3 [21]. A MOF bearing deuterated difluorophenylene rotor was studied using deuterium quadrupolar lineshape analysis. The simulation successfully reproduces the experimental spectra with a model featuring 180° jumps between two equilibrium positions. The jumping frequency increases as temperature rises and reaches fast exchange regime at 260 K. One can use the Arrhenius equation to obtain an activation barrier of 6.8 ± 0.1 kcal/mol and an attempt frequency of 5.4×10^{12} s^{-1}.

1.3.3 ^{1}H Spin-Lattice Relaxation

Spin-lattice relaxation time(T_1) is sensitive to motions in crystalline solids. When the correlation time of motion is equal to $1/\omega$(ω is Larmor frequency of the nucleus), the relaxation becomes most effective and T_1 is shortest. Kubo-Tomita theory is widely used to explain relation between temperature and relaxation time in the case of isotropic reorientation with dynamics described by a single correlation time.[22] The Kubo-Tomita relation, published in 1954, is given by:

$$1/T_1 = C[\tau_c(1+\omega_0^2)\tau_c^2)^{-1} + 4\tau_c(1+4\omega_0^2\tau_c^2))^{-1}] \tag{1.8}$$

$$\tau_c = \tau_0 \exp E_a/RT \tag{1.9}$$

$$C = (n/N)(9/40)(\mu_0/4\pi)2\gamma 4\hbar^2/r^6 \tag{1.10}$$

C is the strength of the dipolar interactions, ω_0 is proton Larmor frequency, τ_c is characteristic correlation time, τ_0 is rotation time constant which is equal to inverse

of attempted frequency. E_a is activation energy, n is the number of mobile protons in such relaxation process out of the total number of protons N, μ_0 is Vacuum permeability, γ is proton gyromagnetic ratio, r is distance between adjacent rotors. By fitting the experimental temperature dependency of T_1, one can extract E_a and ω_0, which are key elements to understand a dynamic process. Even though C can be obtained for a well-defined structure, it is convenient to extract C as a fitting parameter for a complicated rotor system.

A good example is shown in a bicyclo[2.2.2]octane dicarboxylic acid (BODCA)-MOF in Figure 1.4.[23] The relaxation process was captured between 6 and 298 K, which revealed the ultrafast rotation of the bicyclo[2,2,2]octane rotor with a barrier as low as 0.185 kcal/mol.

^{1}H spin-lattice relaxation can measure a frequency range of 10^7 to 10^9 Hz, depending on frequency and variable-temperature capability of NMR spectrometers.It is a vary powerful tool when it comes to ultrafast rotation that exceeds the range of ^{2}H quadrupolar lineshape analysis. Even though it does not require isotope enrichment which could be time-consuming or even impossible for some molecules, the contribution to the wideline ^{1}H spectra from non-rotor protons still presents a significant challenge to researchers while illustrating data.

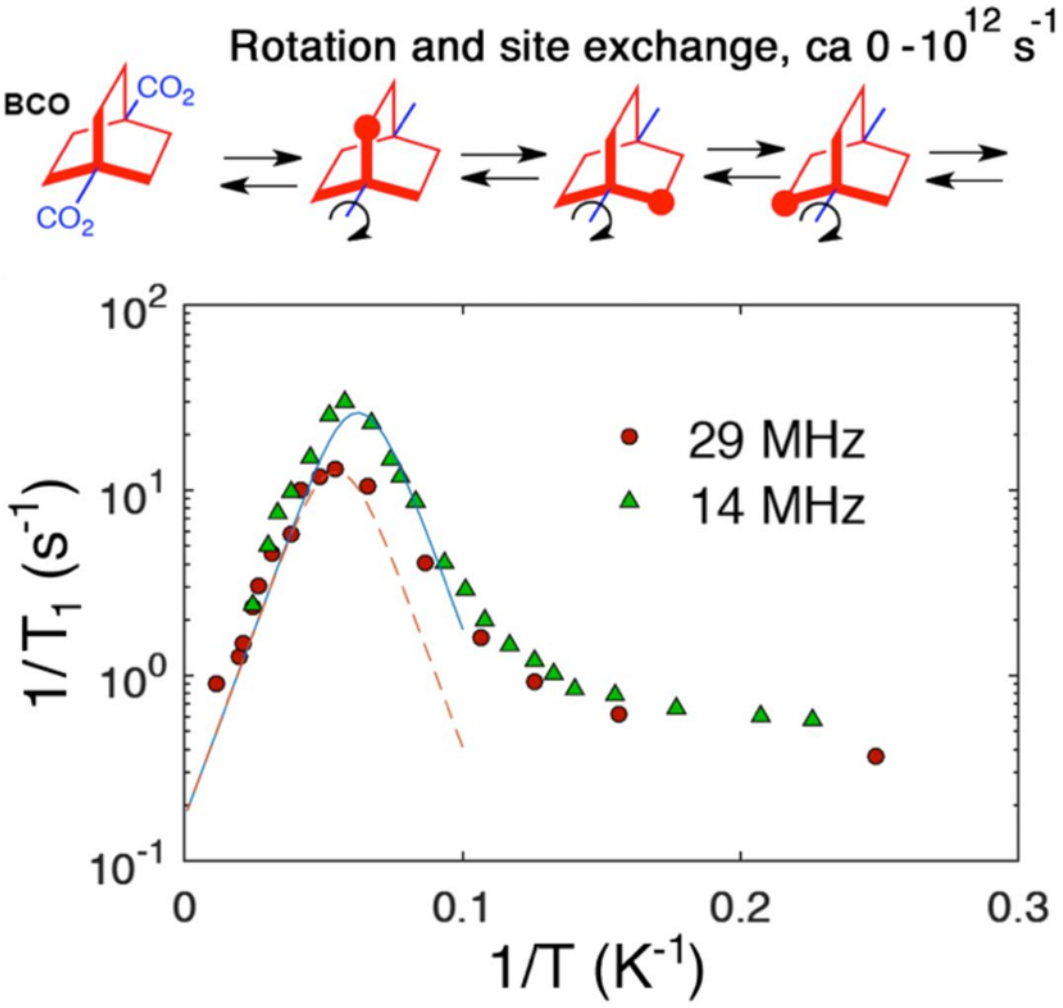

Figure 1.4: 1H T1 relaxation data of the natural abundance BODCA-MOF from T = 2.3–80 K. Copyright 2017 National Academy of Sciences.

1.3.4 Broadband Dielectric Spectroscopy

Broadband dielectric spectroscopy(BDS) is used to probe the movement of dipoles when external AC field is applied. Since its invention by Peter Debye in 1912, it has been be widely applicable in polymers, biomolecules and nanomaterials.[24] Responses of various polarization of electric dipoles fall into a wide range and contain huge amount of information about the microscopic dynamic behaviors of the dipoles.

When an electric field is applied, electric dipoles are polarized. By measuring capacitance, BDS measures polarization due to the number and strength of dipoles. In a parallel-plate electrodes with cross area of A and distance d, the capacitance C is given by

$$C = \epsilon\,\epsilon_0\,\frac{A}{d} \tag{1.11}$$

where $\epsilon_0$is the vacuum permittivity, ϵ is relative permittivity of the material in between electrode.And polarization P of the material is given by

$$P = \epsilon_0\,\chi\,E \tag{1.12}$$

$$\chi = \epsilon - 1 \tag{1.13}$$

χ is susceptibility of the material, E is eletric field strength. Such polarization undergoes exponential decay when E instantly drops to zero. Therefore we have

$$P(t) = P(0)\exp\left(-t/\tau\right) \tag{1.14}$$

τ is relaxation time constant, inverse of reorientation frequency. And after a fourier

transform it becomes

$$P(\omega) = \int_0^\infty P(0)\, \exp\left(-t/\tau\right)\, \exp\left(i\omega t\right) dt \tag{1.15}$$

$$= P(0)\, \frac{\tau}{1 + i\omega\tau} \tag{1.16}$$

Combine (1.12) and (1.16), a complex susceptibility can be obtained by:

$$\epsilon_0 \cdot \chi = \frac{\chi_s}{1 + \omega^2\tau^2} + i \cdot \frac{\chi_s\, \omega\tau}{1 + \omega^2\tau^2} \tag{1.17}$$

where $\chi_s = P_0/E_0$. Then plug (1.13) back in here, we have a complex dielectric constant(permittivity), which is proportional to capacitance measured by BDS under the same configuration:

$$\epsilon^* = \epsilon^{'} - i\, \epsilon^{''} \tag{1.18}$$

$$\epsilon^{'} = \epsilon_\infty + \frac{\epsilon_s - \epsilon_\infty}{1 + \omega^2\tau^2} \tag{1.19}$$

$$\epsilon^{''} = \frac{\omega\tau\left(\epsilon_s - \epsilon_\infty\right)}{1 + \omega^2\tau^2} \tag{1.20}$$

The complex dielectric constant indicates the strength of the relation between an electric field and polarization induced by it. And similar to NMR raw data, both its real and imaginary part both have their physical meanings. The real part is the in-phase response which represents the ability of the material to store the electric energy. The imaginary part is related to dissipation of energy and therefore mentioned as dielectric loss at times. For the purpose of this text, dielectric loss or dissipation factor ($\tan\delta = \epsilon^{''}/\epsilon^{'}$) is used to describe dipole reorientation. The response of an ideal dipole to external field can be seen in Figure 1.5. When $\omega\,\tau = 1$,(i.e. the reorientation frequency matches the AC field frequency), the material

dissipates the most electric field energy, which means dipole relaxation is the most effective. Therefore, by varying the temperature of the measurement, one can obtain the reorienting frequency profile at various temperatures and extract energy barrier and attempted frequency.

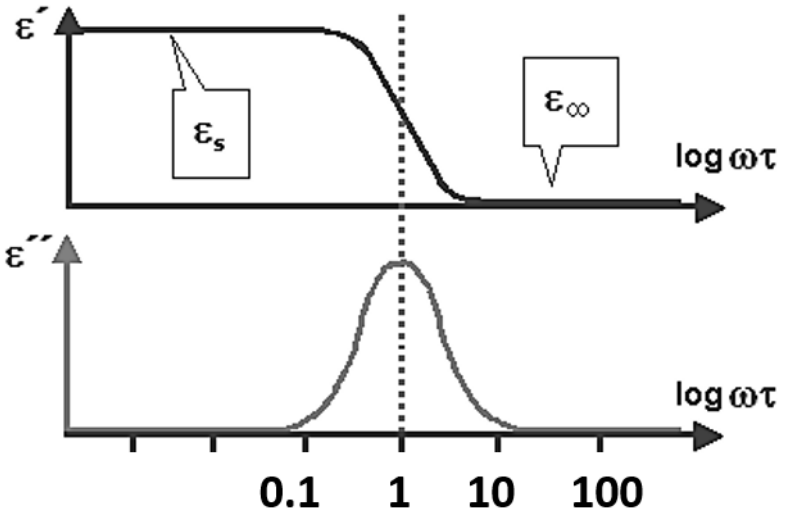

Figure 1.5: Real and imaginary dielectric constant of an ideal electric dipole

The same amphidynamic MOF showed in Figure 1.4 was also characterized by dielectric spectroscopy at various temperatures and the result is shown in Figure 1.6. From Arrhenius fitting of the data, an activation barrier of 7.2 kcal/mol and pre-exponential factor of 2.8×10^{11} Hz were obtained, which agreed with fitting from deuterium lineshape analysis (6.8 kcal/mol and 5.4×10^{12}Hz).

One major limit in measuring powders/nanocrystals with BDS is that the solid-air interface creates significant hindrance to data analysis. And another is that since all dipoles contribute to the electric response, it cannot directly tell the response of one electric dipoles from another, especially in structures with multi polar com-

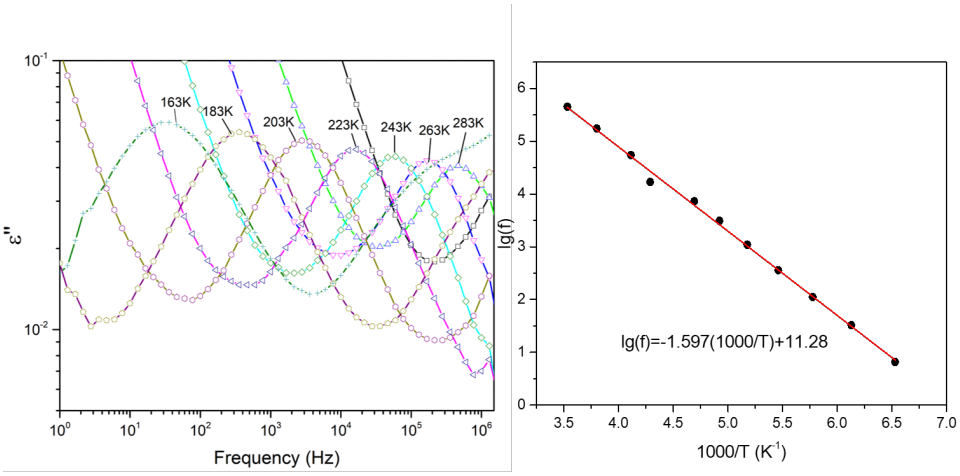

Figure 1.6: Experimental dielectric loss plotted vs. frequency (left) and Arrhenius fitting with loss peak and corresponding temperature(right) of F2BDC MOF. Reprinted with permission from J. Phys. Chem. C 2020, 124, 28, 15391–15398. Copyright 2020 American Chemical Society.

ponents. Nonetheless, with lower temperature(liquid helium cryostat) and higher frequency spectrometer(in tetrahertz regime), a more complete depiction of faster dynamic in sub 1 kcal/mol level will be made possible. Even though such dielectric spectrometers are still not commonly found applying to nanomaterials, they will play a more important role in explorations of molecular machines.

1.3.5 Computational Methods to Study Rotational Dynamics in Crystalline Solids

Computational investigation is needed to understand experimental data of a dynamic characterization. Moreover, experimental methods mentioned above rely on

magnetic resonance or dielectric relaxation. For such phenomenon to occur, a match between rotational frequency and nuclear Larmor frequency/electric field frequency is required. Therefore, computational analysis is also essential when studying dynamic processes that fall out of the range of instruments. Based on single-crystal structural data, modeling of crystalline molecular rotors can start from single molecule. An intrinsic energy barrier can be obtained from energy profile. To mimic real environment, one can build a cluster of molecules to consider both intra- and inter-molecular forces for the target molecule.

Density Functional Theory(DFT) calculation is an excellent method to simulate rotations in such an environment. In traditional electronic structure calculations, approximate solutions to a 3N dimensional Schrödinger equation for a system with N electrons becomes prohibitively difficult as number of electrons increases. DFT simulation, a method to avoid such solutions of the Schrödinger equation, treats the electron density as a function of only three spatial coordinates. In essence, DFT is an approximate method and its accuracy relies on the quality of approximation of exchange-correlation energy. Nonetheless, it significantly simplifies simulations of large systems and provides reliable ground-state energy predictions. More fundamentals on DFT theory is out of the scope of this dissertation and can be found in [25], [26]. In our study, we use DFT computation in Wavefunction Spartan software to predict ground state energy of different configuration during rotation thus an energy profile can be plotted.

References

[1] S. D. Karlen and M. A. Garcia-Garibay, "Amphidynamic crystals: Structural blueprints for molecular machines," in *Molecular Machines*, Springer, 2005, pp. 179–227.

[2] L. Shen, S.-W. Yang, S. Xiang, *et al.*, "Origin of long-range ferromagnetic ordering in metal–organic frameworks with antiferromagnetic dimeric-cu (ii) building units," *Journal of the American Chemical Society*, vol. 134, no. 41, pp. 17 286–17 290, 2012.

[3] A. Glowacz, "Recognition of acoustic signals of synchronous motors with the use of mofs and selected classifiers," *Measurement Science Review*, vol. 15, no. 4, p. 167, 2015.

[4] L. E. Kreno, K. Leong, O. K. Farha, M. Allendorf, R. P. Van Duyne, and J. T. Hupp, "Metal–organic framework materials as chemical sensors," *Chemical reviews*, vol. 112, no. 2, pp. 1105–1125, 2012.

[5] M. Guo, H.-L. Cai, and R.-G. Xiong, "Ferroelectric metal organic framework (mof)," *Inorganic Chemistry Communications*, vol. 13, no. 12, pp. 1590–1598, 2010.

[6] K. Asadi and M. A. van der Veen, "Ferroelectricity in metal–organic frameworks: Characterization and mechanisms," *European Journal of Inorganic Chemistry*, vol. 2016, no. 27, pp. 4332–4344, 2016.

[7] M. Jin, S. Yamamoto, T. Seki, H. Ito, and M. A. Garcia-Garibay, "Anisotropic thermal expansion as the source of macroscopic and molecular scale motion in phosphorescent amphidynamic crystals," *Angewandte Chemie International Edition*, vol. 58, no. 50, pp. 18 003–18 010, 2019.

[8] P. Naumov, S. Chizhik, M. K. Panda, N. K. Nath, and E. Boldyreva, "Mechanically responsive molecular crystals," *Chemical reviews*, vol. 115, no. 22, pp. 12 440–12 490, 2015.

[9] A. Colin-Molina, D. P. Karothu, M. J. Jellen, *et al.*, "Thermosalient amphidynamic molecular machines: Motion at the molecular and macroscopic scales," *Matter*, vol. 1, no. 4, pp. 1033–1046, 2019.

[10] M. A. Garcia-Garibay and C. E. Godinez, "Engineering crystal packing and internal dynamics in molecular gyroscopes by refining their components. fast exchange of a phenylene rotator by 2h nmr," *Crystal Growth and Design*, vol. 9, no. 7, pp. 3124–3128, 2009.

[11] H. Furukawa, K. E. Cordova, M. O'Keeffe, and O. M. Yaghi, "The chemistry and applications of metal-organic frameworks," *Science*, vol. 341, no. 6149, p. 1 230 444, 2013.

[12] M. J. Jellen, M. J. Ayodele, A. Cantu, M. D. Forbes, and M. A. Garcia-Garibay, "2d arrays of organic qubit candidates embedded into a pillared-paddlewheel metal–organic framework," *Journal of the American Chemical Society*, vol. 142, no. 43, pp. 18 513–18 521, 2020.

[13] D.-W. Fu, W. Zhang, H.-L. Cai, *et al.*, "A multiferroic perdeutero metal–organic framework," *Angewandte Chemie International Edition*, vol. 50, no. 50, pp. 11 947–11 951, 2011.

[14] S. Horiuchi and Y. Tokura, "Organic ferroelectrics," *Nature materials*, vol. 7, no. 5, pp. 357–366, 2008.

[15] L. B. Alemany, D. M. Grant, T. D. Alger, and R. J. Pugmire, "Cross polarization and magic angle sample spinning nmr spectra of model organic compounds. 3. effect of the carbon-13-proton dipolar interaction on cross polarization and carbon-proton dephasing," *Journal of the American Chemical Society*, vol. 105, no. 22, pp. 6697–6704, 1983.

[16] S. Hartmann and E. Hahn, "Nuclear double resonance in the rotating frame," *Physical Review*, vol. 128, no. 5, p. 2042, 1962.

[17] M. Emshwiller, E. Hahn, and D. Kaplan, "Pulsed nuclear resonance spectroscopy," *Physical Review*, vol. 118, no. 2, p. 414, 1960.

[18] J. H. Simpson, D. M. Rice, and F. E. Karasz, "2h nmr characterization of phenylene ring flip motion in poly (p-phenylene vinylene) films," *Journal of Polymer Science Part B: Polymer Physics*, vol. 30, no. 1, pp. 11–18, 1992.

[19] H. W. Spiess, "Molecular dynamics of solid polymers as revealed by deuteron nmr," *Colloid and Polymer Science*, vol. 261, no. 3, pp. 193–209, 1983.

[20] M. R. Hansen, R. Graf, and H. W. Spiess, "Solid-state nmr in macromolecular systems: Insights on how molecular entities move," *Accounts of Chemical Research*, vol. 46, no. 9, pp. 1996–2007, 2013.

[21] I. Liepuoniute, C. M. Huynh, S. Perez-Estrada, *et al.*, "Enhanced rotation by ground state destabilization in amphidynamic crystals of a dipolar 2, 3-difluorophenylene rotator as established by solid state 2h nmr and dielectric spectroscopy," *The Journal of Physical Chemistry C*, vol. 124, no. 28, pp. 15 391–15 398, 2020.

[22] R. Kubo and K. Tomita, "A general theory of magnetic resonance absorption," *Journal of the Physical Society of Japan*, vol. 9, no. 6, pp. 888–919, 1954.

[23] C. S. Vogelsberg, F. J. Uribe-Romo, A. S. Lipton, *et al.*, "Ultrafast rotation in an amphidynamic crystalline metal organic framework," *Proceedings of the National Academy of Sciences*, vol. 114, no. 52, pp. 13 613–13 618, 2017.

[24] F. Kremer and A. Schönhals, *Broadband dielectric spectroscopy*. Springer Science & Business Media, 2002.

[25] R. M. Dreizler and E. K. Gross, *Density functional theory: an approach to the quantum many-body problem*. Springer Science & Business Media, 2012.

[26] W. Koch and M. C. Holthausen, *A chemist's guide to density functional theory*. John Wiley & Sons, 2015.

CHAPTER 2

Structrue and Dynamics of Open Volume Pillar-Layered Zn Metal-Organic Frameworks

2.1 Abstract

In this project we aim to develop a new kind of Metal-Organic Frameworks with functions that rely on the engineered rotational motion of their molecular components. When rotary dipolar arrays are introduced to the framework, ferroelectricity can arise from collective behaviors of dipoles. We designed and synthesized a series of zinc MOFs which feature open cavities and low intrinsic barrier. X-ray structure suggests the rotary motion of the dipoles. Even though dynamic parameters cannot be determined due to stability of the MOF upon removal of solvent guest molecules, it provides knowledge for our further explorations on amphidynamic MOF systems.

2.2 Introduction

Due to its wide applications in oscillators, random access memory(RAM), capacitors optics etc, ferroelectricity is an intriguing property which has been reported extensively. Ferroelectricity arises when the material has a non-zero spontaneous polarization and non-centrosymmetry. Ferroelectricity in most of previous studies arises from displacement[1], order-disorder transition[2] and host-guest interactions[3], which had been observed before in conventional inorganic and organic ferroelectrics.[4] However, as a class of hybrid material, MOFs have potentials to bridge the gap and bring more possibilities. Specifically, by utilizing the porous structures of MOFs, we can introduce rotary dipoles with low barriers to amphidynamic MOFs and explore its electric properties originating solely from orientational polarization, one of the four basic polarization mechanisms. Compared to displacement and order-disorder type ferroelectrics, polar functional groups in rotary dipole arrays can bring stronger orientational polarization hence stronger ferroelectric effects.

In traditional close-packed solids, it was intrinsically difficult due to such rotation barriers are significantly higher than dipole-dipole interaction. While in amphidynamic MOFs, dipoles with low rotational barriers arranged in a porous framework are likely to give rise to exceptional orientational polarization for two reasons. 1) A porous structure has smaller steric effect. 2) The intrinsic energy barrier can be controlled by ligand structure without altering crystal topology/packing.To advance the understanding of dynamics of such rotary dipoles in frameworks, we designed, synthesized and characterized a series of Zn MOFs withtriptycene dicarboxylic acid

as in-layer ligand[5] and bis(pyridylethynyl)benzene (BPB)or functionalized bispyridalbenzene (BPEB) as pillar ligand.

2.3 Results and Discussion

2.3.1 Dynamics of $Zn_2(TDC)_2$(BPEB-2F)

The strategy is to incorporate functionalized bisenthynylphenylene rotor in a Zn paddle-wheel MOF. Because Zn can coordinate with both oxygen and nitrogen. Triptycenedicarboxylic acid is selected as in-layer ligand as its bulkiness will prevent interpenetration which is common in Zn paddle-wheel MOFs with long linear ligand.(Figure 2.1 left)

The $Zn_2(TDC)_2$(BPEB-2F) MOF was synthesized via solvothermal method: Ligand and MOFs are dissolved in DMF and heated to 100° for 24 hours. Near cubic crystals are obtained as seen in microscopic pictures. Unfunctionalized $Zn_2(TDC)_2$-(BPEB) was also synthesized from bis(pyridalethynyl)benzene(BPEB) under same condition as a blank contrast for dielectric constant measurements.

After doing solvent exchange with fresh DMF and low boiling point solvent (acetone, DCM or methanol), the MOFs are evacuated overnight. However, the structure collapses upon removal of guest solvent at either heated or room temperature condition. Superconducting CO_2 drying is also employed but the crystals still cannot maintain its structure. Therefore, we attempt to investigate the DMF solvated struc-

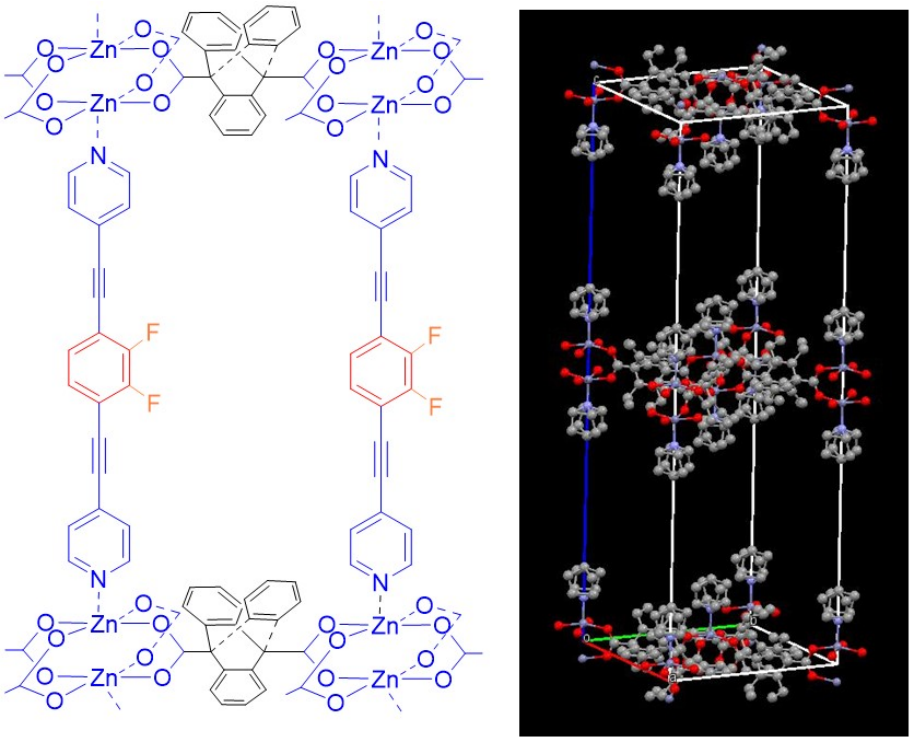

Figure 2.1: Chemical(left) and X-ray structrue(right) of $Zn_2(TDC)_2$(BPEB-2F) MOF

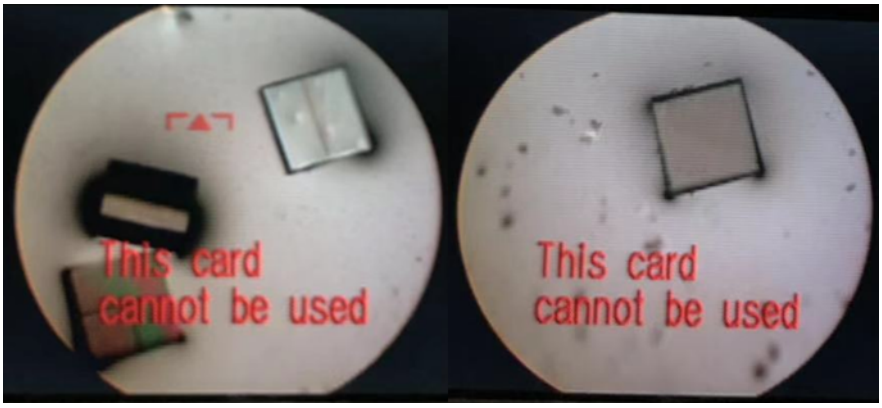

Figure 2.2: Microscopic image of tetragonal $Zn_2(TDC)_2$(BPEB-2F) crystals

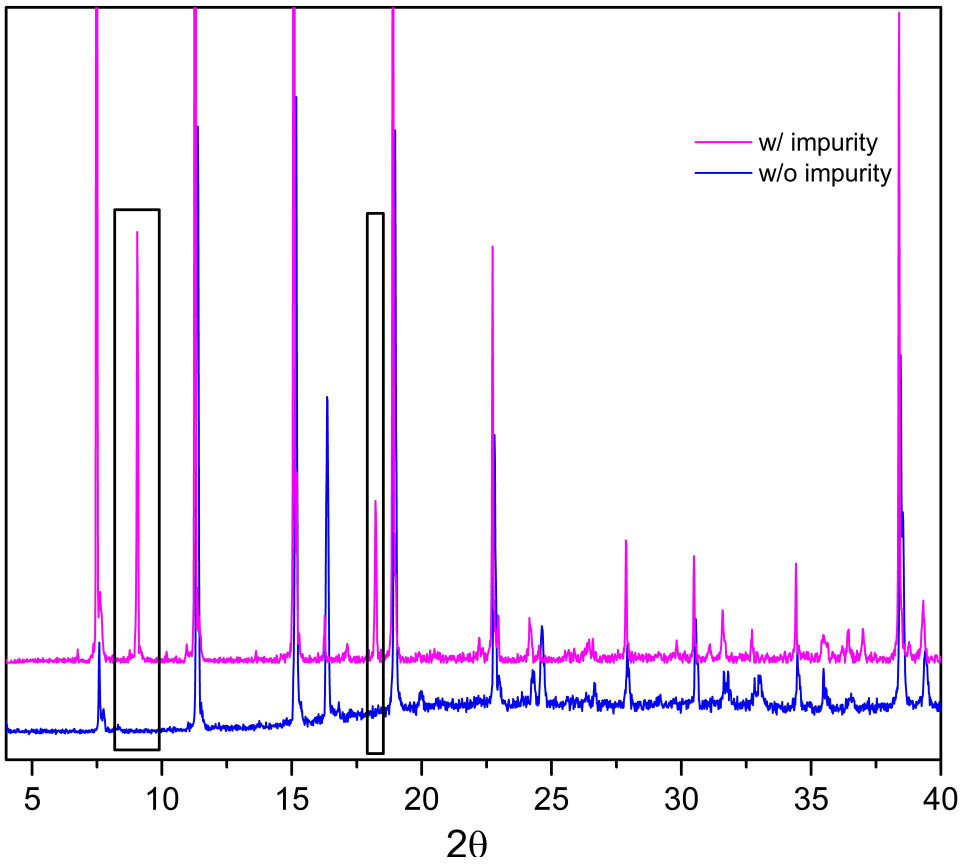

Figure 2.3: PXRD pattern of $Zn_2(TDC)_2$(BPEB-2F). Impurities appear when if heated over 48 hours under 120 degrees

ture.

Single crystal X-ray structure shows a tetragonal phase pillar-layered structure we desired. The rotor part was invisible in X-ray structure because its fast motion blurred the diffraction of electrons around it. It means the presence of solvent molecules did not hinder the rotation.

The fluorine ssNMR was used to investigate. Fluorine has similar gyromagnetic ratio to hydrogen and relaxation behaviour of fluorine atoms is expected when rotational frequency is matching magnetic field frequency. However, the resulting fluorine ssNMR spectra have very low fluroine signal due to low fluorine content in the sample and fluorine background from perfluorinated probe parts.

We turn to dielectric spectroscopy to characterize electric response of the MOFs under electric field. In the structure, the only components that have significant contributions to polarization are difluorophenylene rotor and solvent. In dielectric characterization, to avoid influence of dipoles from solvent, we conducted solvent exchange with toluene which has low polarity. Then solvent on surface of the crystals were wiped with filter paper before placed in dielectric spectrometer for measurement. Unfortunately, in comparison with dielectric response of unfunctionalized $Zn_2(TDC)_2(BPEB)$ MOF, response from solvent molecules still prevails under such circumstance(Figure 2.4 and 2.5).

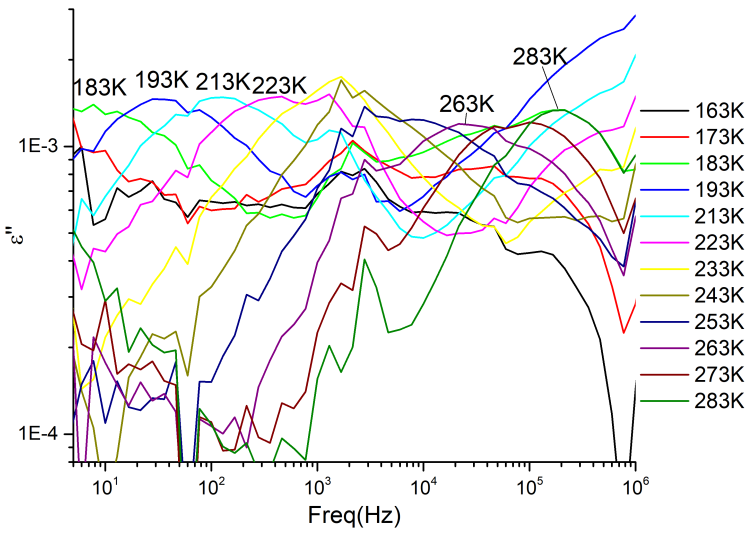

Figure 2.4: Imaginary dielectric constant of BPEB-2F MOF with toluene at various frequency and temperature

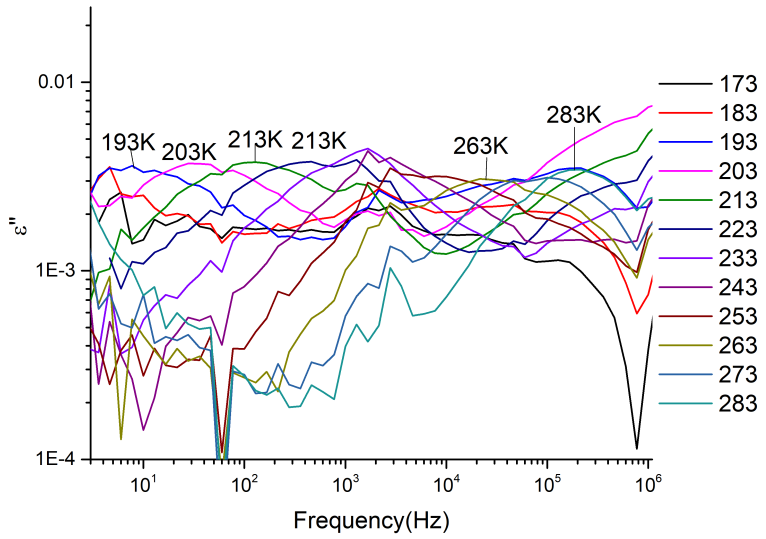

Figure 2.5: Imaginary dielectric constant of BPEB MOF with toluene at various frequency and temperature

2.3.2 $Zn_2(TDC)_2(BPB)$ MOF with Reduced Pillar Length

We seek to understand the stability of such tetragonal pillar-layered MOF system to facilitate future design. Therefore an isoreticular MOF with bispyridalbenzene(BPB) is synthesized. BPB ligand does not have ethynyl group thus rotational barrier remains high. However, the linear linker is shortened by length of two triple bond, thus the pore aperture and pore size are both reduced, and the structure could potentially remain stable when solvent is removed.

The $Zn_2(TDC)_2(BPB)$ MOF is synthesized under similar condition in DMF (details in experimental section). While single crystal X-ray diffraction yield no structural information due to poor crystal quality, the PXRD shows iso-distance peak which indicates a layered structure is obtained (Figure 2.6).

It was noted that addition of acetic acid can change the crystal from near-cubic shape to tetragonal phase. The possible explanation is that acetic acid is slowing down the rate of growth of TDC layer thus elongates the crystals.

Evacuation of solvent at elevated temperature still collapses the structure, which is indicated by PXRD(Figure 2.11). Under microscope, programmed heated crystals from room temperature to 250 °C under ambient condition showed disappearance of birefringence at around 60 °C, which indicates lost of crystallinity. At similar temperature, TGA shows significant weight loss(25%) (Figure 2.10). However, shape of crystals remained intact during the entire process. Supercritical CO_2 drying at different rate is tried however the structure still collapse after drying.

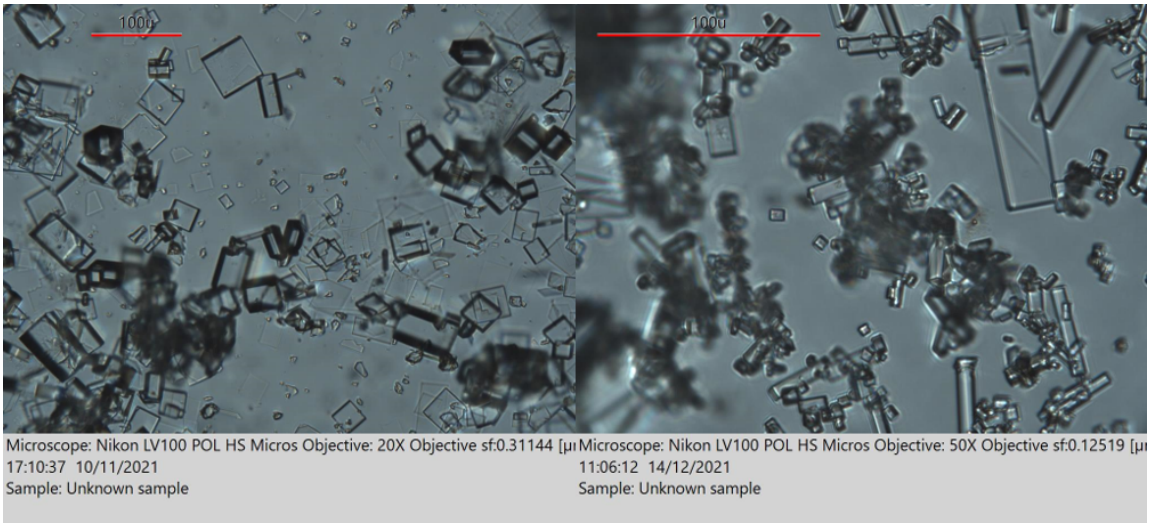

Figure 2.6: Microscopic photos of $Zn_2(TDC)_2(BPB)$ synthesized with no modulator(left) and 20 vol% acetic acid(right)

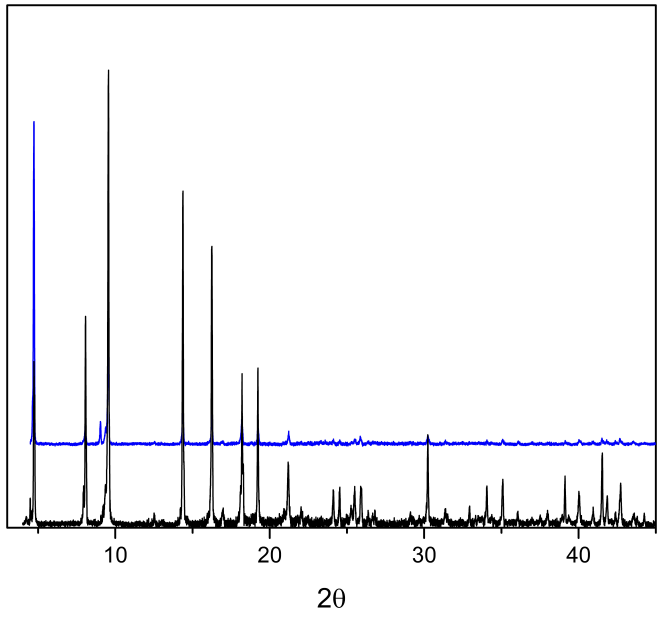

Figure 2.7: PXRD pattern of $Zn_2(TDC)_2(BPB)$ synthesized with no modulator(black) and 20 vol% acetic acid(blue)

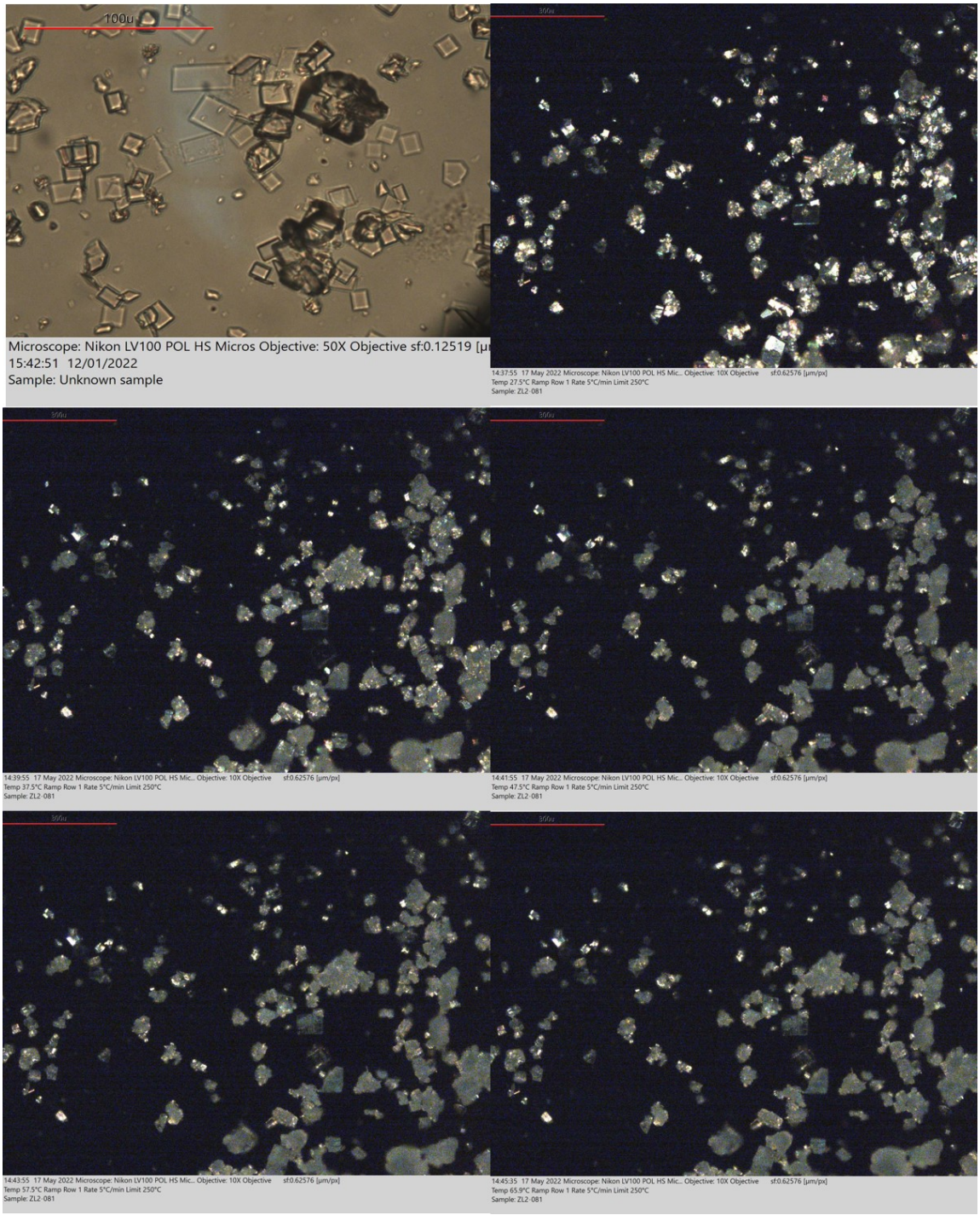

Figure 2.8: Polarized variable-temperature microscopic images of $Zn_2(TDC)_2(BPB)$

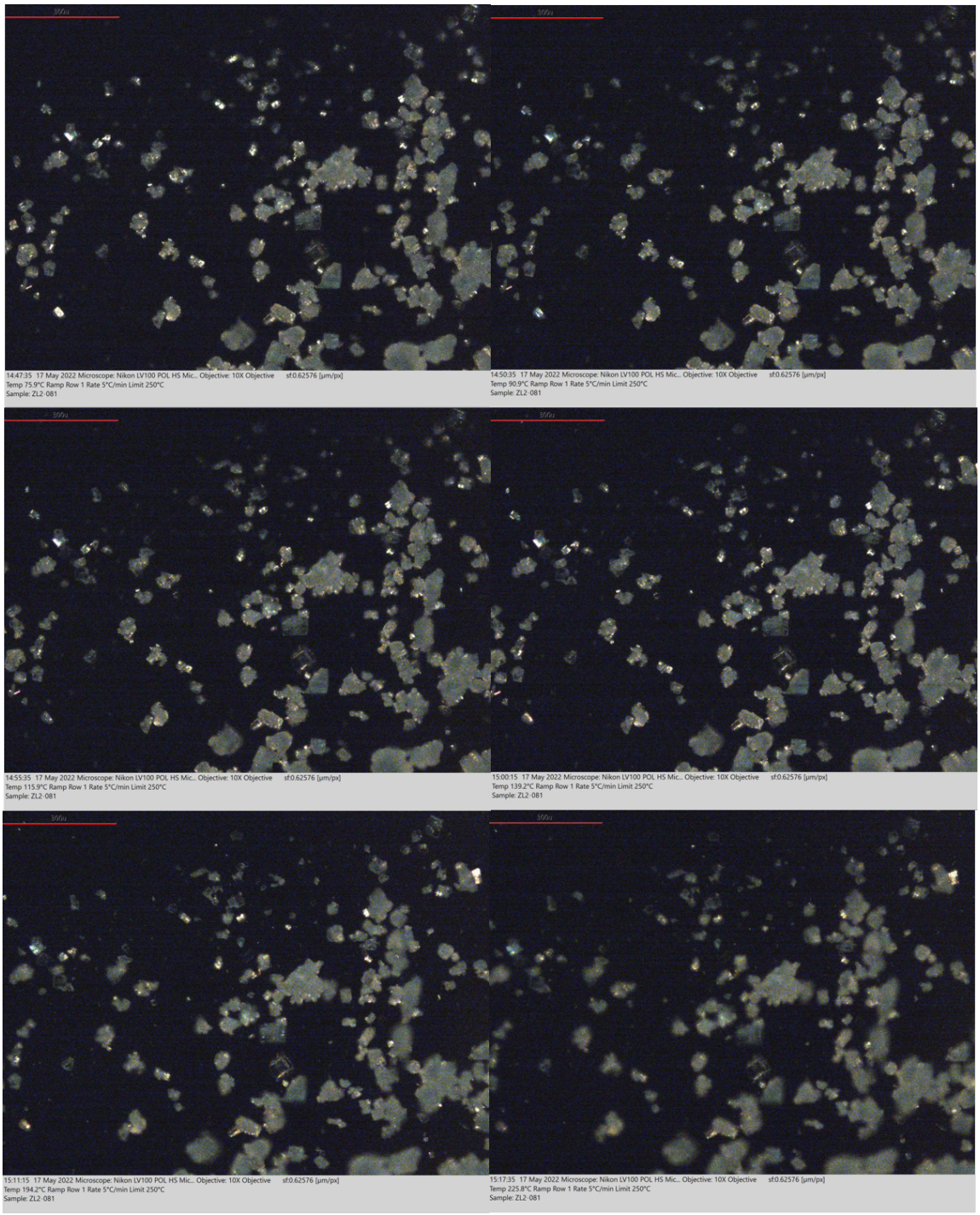

Figure 2.9: Polarized variable-temperature microscopic images of $Zn_2(TDC)_2(BPB)$

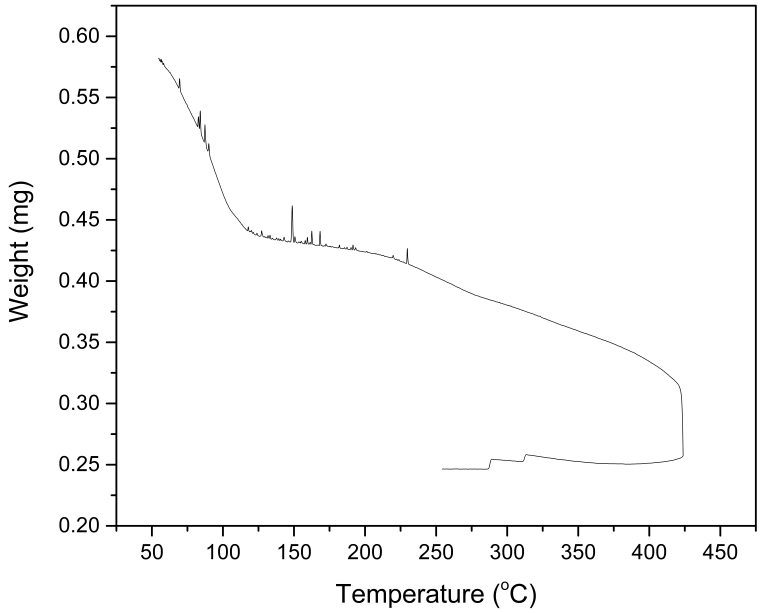

Figure 2.10: Thermogravimetric analysis of $Zn_2(TDC)_2(BPB)$

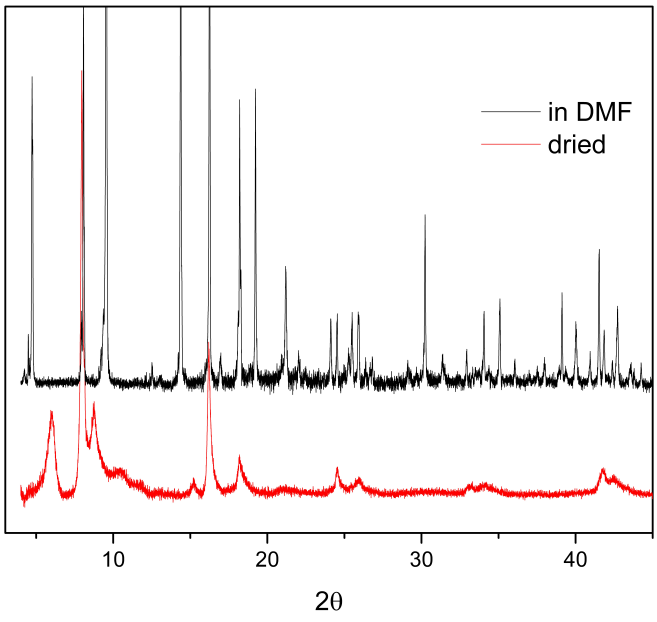

Figure 2.11: PXRD pattern of as synthesized(black) and supercritical CO_2 dried(red) $Zn_2(TDC)_2(BPB)$

2.4 Experimental Sections

2.4.1 Syntheses of Ligands

9,10-bis(chloromethyl)anthracene: Anthracene(5.0 g, 28.1 mmol), paraformaldehyde (4.2 g, 140.0 mmol), and conc. HCl (12.0 mL, 395.0 mmol) were added to 60 mL acetic acid and heated to 60°C for 5 h. 100 mL water was added, and the reaction was allowed to stir for 30 min. The reaction was taken off oil bath and stirred until cooled down. The yellow precipitate was filtered, washed with water and 5 mL ethanol and then dried. Yield: 7.1 g, 92%. ^{1}H NMR ($CDCl_3$, 500 MHz) δ(ppm): 8.40 (q, 4H), 7.61 (q, 4H), 6.18 (s, 4H), 2.09 (s, 6H).

Anthracene-9,10-diylbis(methylene) diacetate: 9,10-bis(chloromethyl)anthracene (7.1 g,25.9 mmol) and KOAc (17.5 g, 178.0 mmol) were combined with 150 mL acetic acid and refluxed at 120°C for 5 h. 150 mL water was added, and the reaction was allowed to stir for 30 min then cooled down. The reaction was filtered and precipitate washed with water and 2 mL minimal cold acetone. The yellow solid was recrystallized in DCM at -10°C for 2 days. The mixture was then filtered and washed with another 2 mL acetone to yield 3.0 g of solid. The filtrate was then purified by column chromatography with 1:1 Hexanes:DCM. The resulting solid was evaporated to dryness and recrystallized in 50 mL acetone. After 2 days, the precipitate was filtered and washed with acetone to afford an additional 0.6 g. anthracene-9,10-diylbis(methylene) diacetate. Yield: 3.6 g, 42.5%. ^{1}H NMR ($CDCl_3$, 300 MHz) δ(ppm): 8.50 (q, 4H), 7.60 (q, 4H), 6.20 (s, 4H), 2.03 (s, 6H).

9,10-Triptycene-bismethylene diacetate: anthracene-9,10-diylbis(methylene) diacetate (1g, 3.1 mol) and CsF (5.65 g, 37.2 mmol) were added to a flame dried 200 mL round bottomed flask and placed under an argon atmosphere. 30 mL dry DCM and 50 mL dry MeCN were then added and the mixture was stirred under 50 °C. And then (trimethylsilyl)phenyl trifluoromethanesulfonate (1.51 mL, 6.2 mmol) was added dropwise. The mixture was heated overnight. After completion of the reaction, the mixture was filtered and concentrated. The crude solid was then purified with column chromatography with 1:1 mixture of DCM:hexane. 1.1 g product was obtained as a white powder (90% yield). ^{1}H NMR ($CDCl_3$, 500 MHz) δ(ppm): 7.32 (q,6H), 7.05 (q, 6H), 5.67 (s, 4H), 2.45 (s, 6H).

9,10-Triptycenedimethanol: triptycene-9,10-diylbismethylene diacetate (1.2 g, 2.9mmol) was and combined with KOH (0.9 g, 15.2 mmol) and MeOH:H_2O (12 mL) in a small round bottomed flask. The reaction was heated at 80°C for 3 h and then 150 mL water was added. The reaction was continued for another 30 minutes. The mixture was cooled to room temperature while stirring. The precipitate was filtered, washed with H_2O, DCM, and then dried. Yield: 0.9 g, 99%. ^{1}H NMR (DMSO-d6, 300 MHz) δ(ppm): 7.52 (s, 6H), 7.00 (q, 6H), 5.50 (s, 2H), 5.02 (d, 4H).

9,10-Triptycenedicarboxylic acid (TDC): 9,10-Triptycenedimethanol (0.9 g, 2.9 mmol) was dissovled in 10 mL acetone. H_2SO_4 (1.0 mL, 18.8 mmol), CrO_3 (1.0 g, 10.3 mmol), and water (9 mL) mixture was added to the solution. Then the reaction mixture was stirred at room temperature for 5 hr. The reaction is stopped when it turned to dark green. Water was then added and the precipitate was filtered,

washed with water, and collected by dissolving in acetone. The product was dried and dissolved in a KOH (20% wt) aqueous solution and filtered. Conc. HCl was added to precipitate out the acid, precipitate was collected and dried. Yield: 0.784 g, 80%. ^{1}H NMR (DMSO-d6, 500 MHz) δ(ppm): 7.84 (q, 6H), 7.11 (q, 6H).

1,4-Bis(2-(4-pyridyl)- ethynyl)-2,3-difluorobenzene (BPEB-2F): 1,4-dibromo-2,3-difluorobenzene, 14 (250 mg, 1.9 mmol), 4-ethynylpyridine (1.12g), $Pd(PPh_3)_2Cl_2$ (270 mg, 0.38 mmol), and CuI (36.5 mg, 0.192 mmol) were added to a flame dried sealed tube and placed under argon atmosphere. 20 mL of 1:1 argon sparged THF:TEA was then added to the flask and the tube was sealed with teflon-lined cap. The reaction mixture was heated to 60 °C for 24 hrs under stirring. After cooling down, the reaction mixture was extracted with ethyl acetate 3 times then purified by chromatography. ^{1}H NMR (300 MHz, $CDCl_3$, ^{19}F decoupled at -130 ppm) δ(ppm): 8.65(q,4H), 7.42(q, 4H), 7.30(s, 2H). 13C NMR (500 MHz, $CDCl_3$) δ(ppm): 152.18, 150.01, 130.21, 127.80, 125.53 113.93, 94.47, 85.36. 19F NMR (282 MHz, $CDCl_3$) δ(ppm): -132.93(s, 2F). HRMS: $C_{20}H_{11}N_2F_2(MH^+)$ calc: 317.08848, found: 317.08871.

2.4.2 NMR Spectra

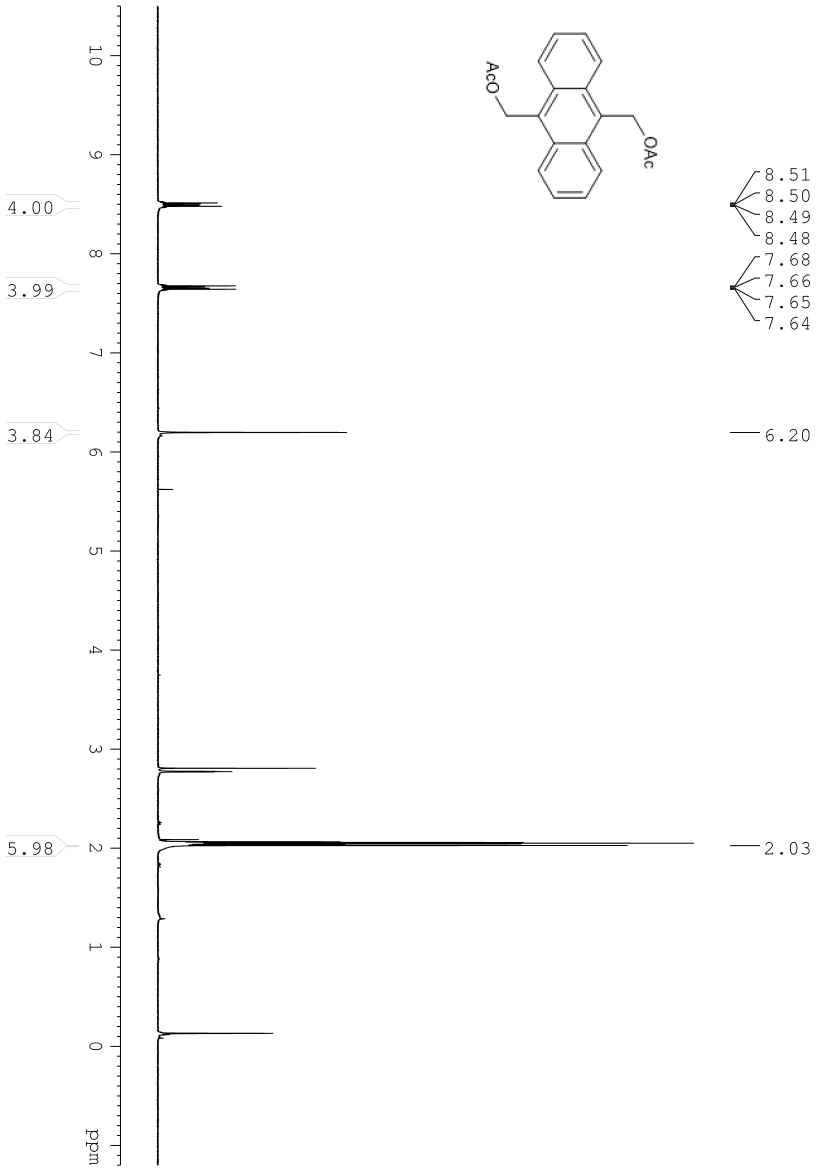

Figure 2.12: ^{1}H NMR(300 MHz, acetone-d6) of anthracene-9,10-diylbis(methylene) diacetate

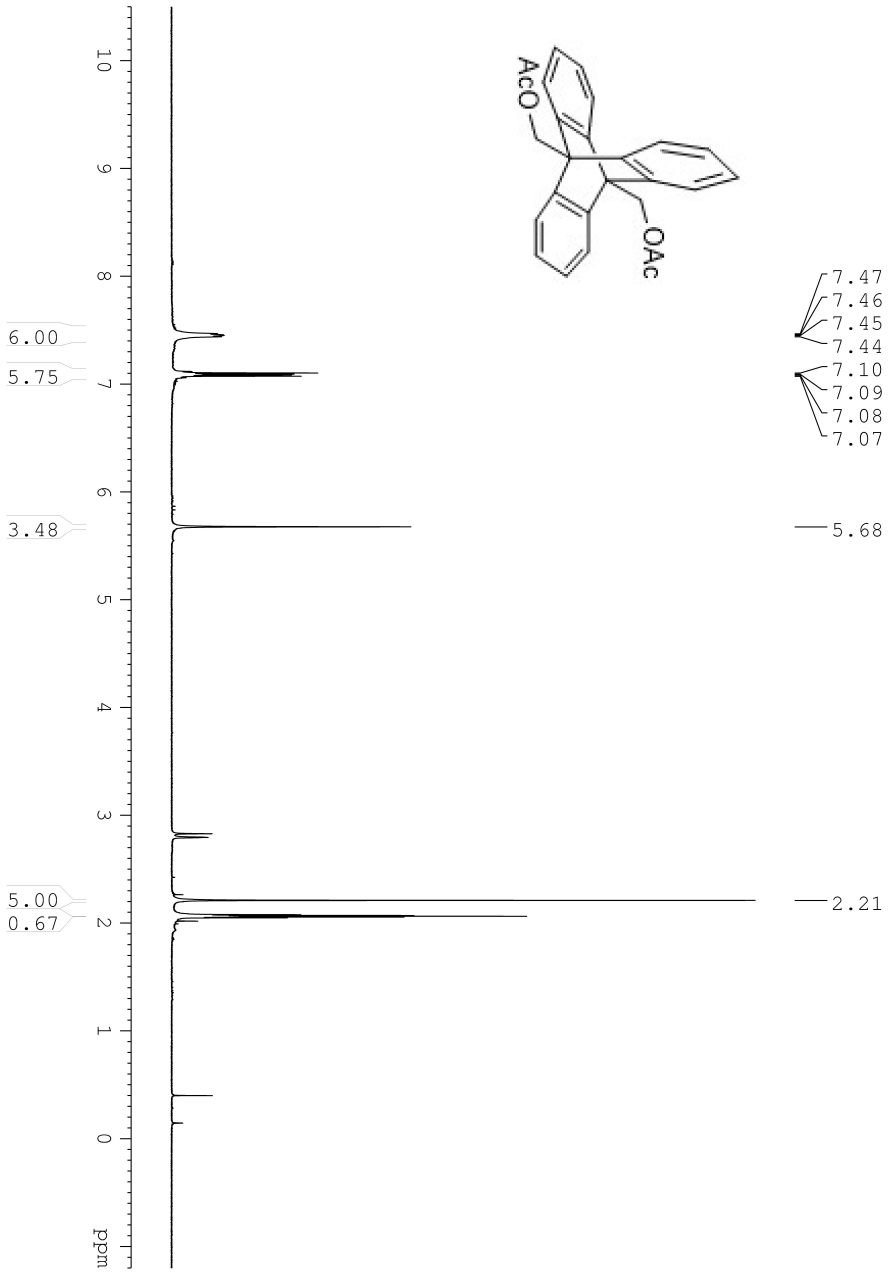

Figure 2.13: ^{1}H NMR(300 MHz, acetone-d6) of 9,10-triptycene-bismethylene diacetate

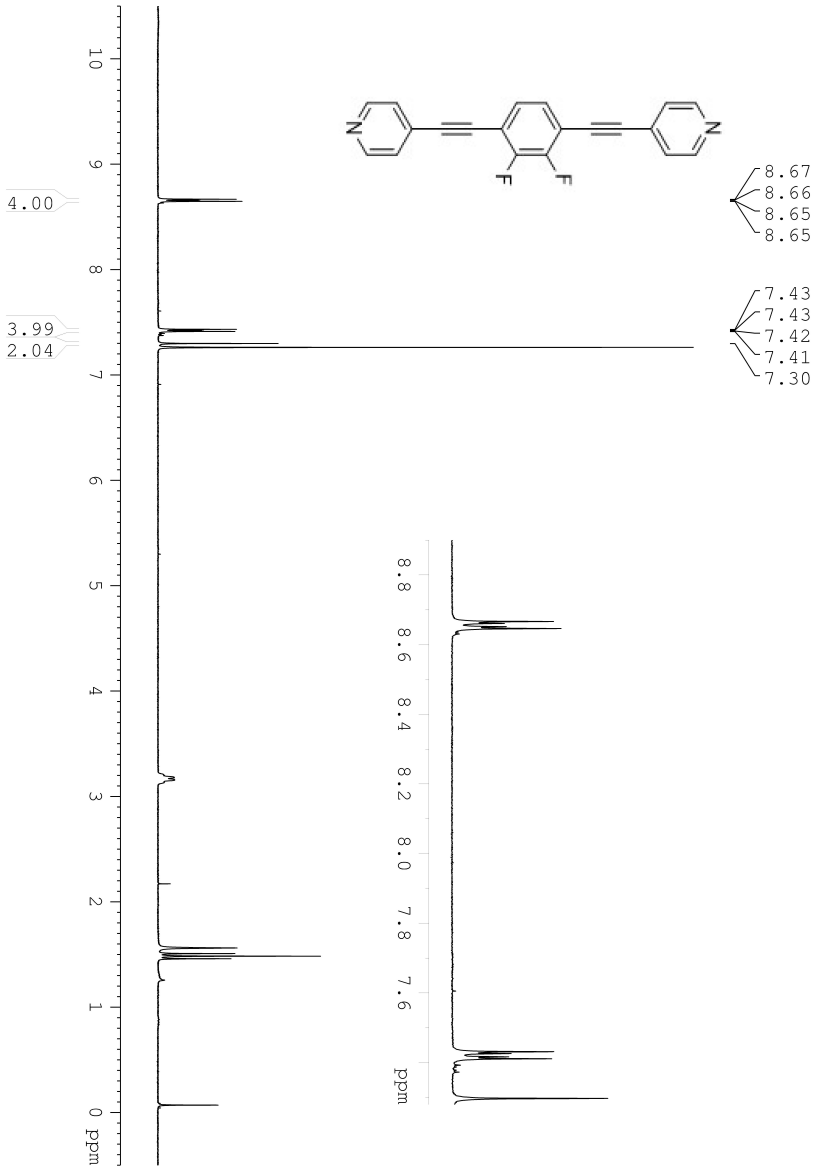

Figure 2.14: ^{1}H NMR(300 MHz, $CDCl_3$, ^{19}F decoupled at -130MHz) of 1,4-bis(2-(4-pyridyl)- ethynyl)-2,3-difluorobenzene

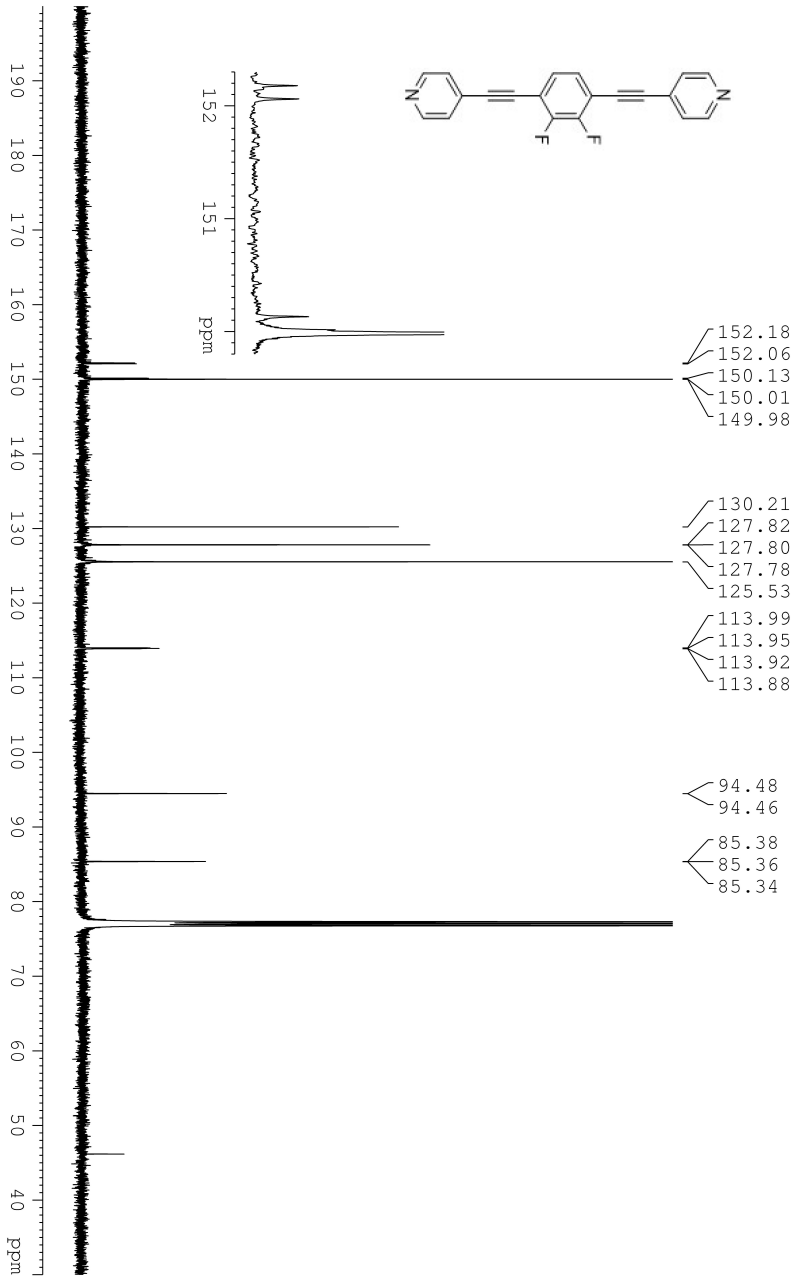

Figure 2.15: ^{13}C NMR(125 MHz, $CDCl_3$) of 1,4-bis(2-(4-pyridyl)- ethynyl)-2,3-difluorobenzene

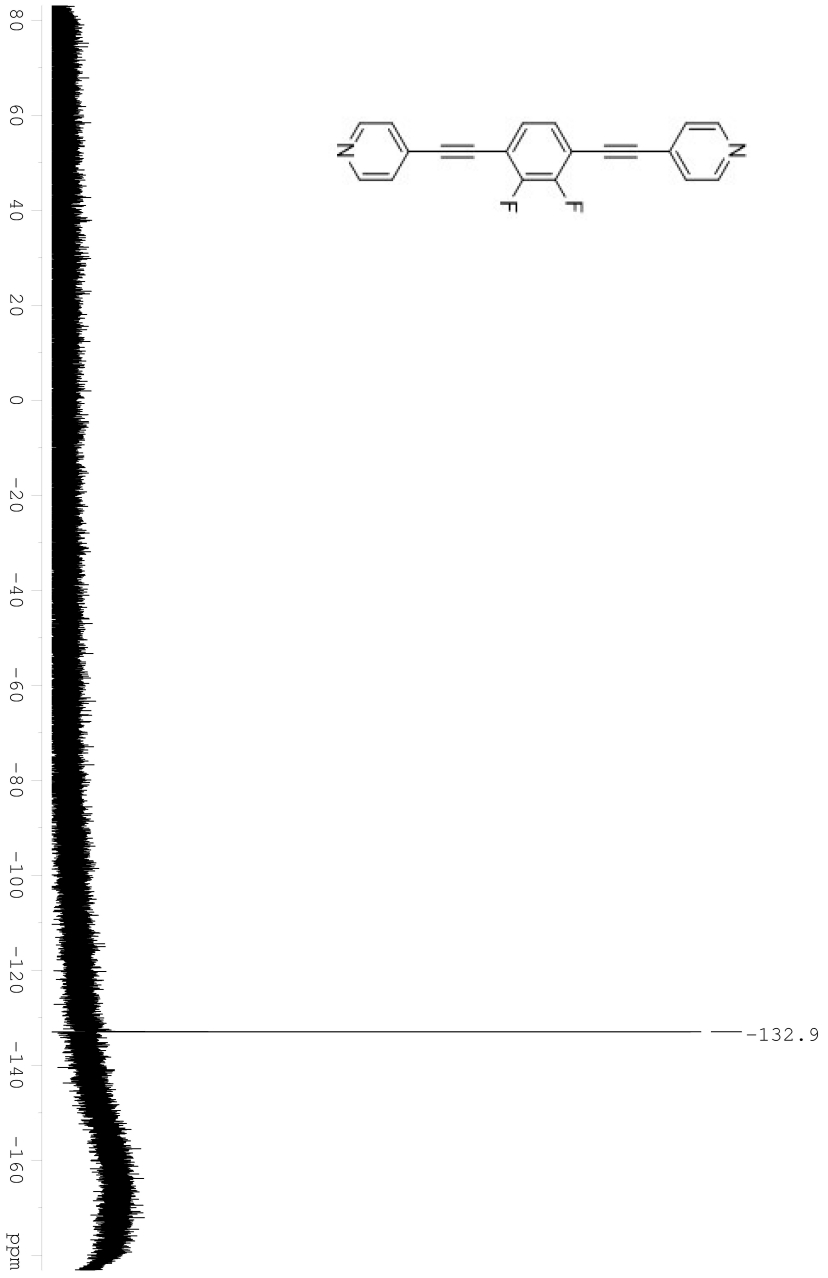

Figure 2.16: ^{19}F NMR(282 MHz, $CDCl_3$) of 1,4-bis(2-(4-pyridyl)- ethynyl)-2,3-difluorobenzene

2.4.3 Syntheses of MOFs

Synthesis of Zn2(TDC)$_2$(BPEB-2F) MOF: zinc nitrate(18.8 mg, 0.1 mmol), BPEB-2F(10 mg, 0.03 mmol) and TDC(22.0 mg, 0.06 mmol) were added to 3 mL DMF in a 2 dram vial. The mixture was sonicated until dissolution and heated to 100 °C for 24 hours. Light yellow cubic crystals are obtained.

Synthesis of Zn2(TDC)$_2$(BPB) MOF: 6 mg of BPB was dissovled in 1 mL DMF. In another vial, 17.7 mg TDC and 15.3 mg zinc nitrate were dissovled in 1.5 mL DMF.Both vials are sonicated. The solutions are mixed together and then heated to 120 °C for 24 hours. Cubic crystals are obtained. If acetic acid is added to the solution before heating, tetragonal crystals are observed.

References

[1] H. Cui, Z. Wang, K. Takahashi, Y. Okano, H. Kobayashi, and A. Kobayashi, "Ferroelectric porous molecular crystal,[mn3 (hcoo) 6](c2h5oh), exhibiting ferrimagnetic transition," *Journal of the American Chemical Society*, vol. 128, no. 47, pp. 15 074–15 075, 2006.

[2] Y. Zhang, W. Zhang, S.-H. Li, *et al.*, "Ferroelectricity induced by ordering of twisting motion in a molecular rotor," *Journal of the American Chemical Society*, vol. 134, no. 26, pp. 11 044–11 049, 2012.

[3] D.-W. Fu, W. Zhang, H.-L. Cai, *et al.*, "A multiferroic perdeutero metal–organic framework," *Angewandte Chemie International Edition*, vol. 50, no. 50, pp. 11 947–11 951, 2011.

[4] S. Horiuchi and Y. Tokura, "Organic ferroelectrics," *Nature materials*, vol. 7, no. 5, pp. 357–366, 2008.

[5] M. J. Jellen, M. J. Ayodele, A. Cantu, M. D. Forbes, and M. A. Garcia-Garibay, "2d arrays of organic qubit candidates embedded into a pillared-paddlewheel metal–organic framework," *Journal of the American Chemical Society*, vol. 142, no. 43, pp. 18 513–18 521, 2020.

CHAPTER 3

Rotational Dynamics of Interpenetrated Amphidynamic Zirconium Metal-Organic Frameworks

PIZOF-2F synthesis and investigations of dynamics are adapted from Zhiyu Liu, Yangyang Wang, Miguel Garcia-Garibay. Rotational Dynamics of an Amphidynamic Zirconium Metal-Organic Frameworks Determined by Dielectric Spectroscopy. *Journal of Physical Chemsitry Letters*, 12(24): 5644-5648,2021. DOI: 10.1021/acs.jpclett.1c01333. PIZOF-d4/d8 is synthesized by Prof. Braulio Rodríguez-Molina group and deuterium ssNMR analysis is in collaboration with Rodríguez-Molina. PIZOF-2NO_2 is unpublished work.

3.1 Abstract

A zirconium metal-organic framework with a difluorophenylene rotator bearing a permanent electric dipole of 3.2 D was synthesized, and its rotational motion was analyzed by temperature- and frequency-dependent broadband dielectric spectroscopy.

While solid-state NMR confirms fast rotation qualitatively, the dissipation factors measured between 113 and 153 K suggested an activation energy $E_a = 2.6$ kcal/mol, but deviations from a single Debye relaxation suggested a dynamic process that cannot be accounted for by a well-defined potential with a single activation barrier. The dynamic heterogeneity of the dipolar rotor was confirmed by analysis in terms of a Cole-Cole relaxation, which suggested a mean barrier of 1.9 kcal/mol, with a heterogeneity that decreases as temperature increases. Based on the single-crystal structure, we propose that the kinetic heterogeneity results from a temperature-dependent potential where rotation is mediated by the escape of the rotator from an energy well created by a double Ph−H···F−Ph hydrogen bond.

Given the nature of fast dynamics in the congested environment of this MOF, a dinitrophenylene rotator was also synthesized and incorporated into MOF with expectations that bulky nitro groups would 1)introduce stronger dipole and 2)avoid interpenetration. However the X-ray structures confirmed isoreticular interpenetration thus the dynamics was not studied.

3.2 Introduction

In recent years, our group and others have developed and characterized several types of amphidynamic crystals, engineered with rigid components linked to moving parts, as promising platforms for the development of smart materials and crystalline molecular machines.[1]–[5] Among them, MOFs have emerged as a promising platform to

explore and engineer emergent properties, such as those arising within crystalline rotary dipole arrays.[6]–[11] It is expected that strongly interacting dipoles that are free to reorient about a particular axis will have a high-temperature paraelectric phase, which, upon cooling, may adopt dipole-dipole-induced collective alignments to ferroelectric or antiferroelectric phases depending on the symmetry of the lattice.[8], [12] This is in contrast to current materials where the formation of these phases depends on phase transitions that rely on atomic and molecular displacements,[13] order-disorder transitions,[14] and host-guest interactions.[15], [16] Furthermore, rotary dipole arrays are expected to have switchable anisotropies as a result of changes in dipole orientation in response to strong external fields.[17]–[20]

One of the key challenges for the realization of self-ordering and external-field addressable dipole arrays is the design of structures with large dipole-dipole interactions (E_{DD}) that experience axial rotations with barriers (E_a) that are lower than thermal energies (RT), i.e., $E_{DD} > RT > E_a$($RT \approx 0.593$ kcal/ mol at 298 K).[9], [21] Giving access to porous structures with short dipole-dipole distances, low rotational barriers, and a range of crystal symmetries, MOFs are among the most promising platforms for the construction of dipole arrays. With that in mind, we explore here the synthesis, characterization and rotational dynamics of a previously reported air-stable zirconium MOF equipped with various substitutions on phenylene ring linked by triple bonds to para-benzenecarboxylate ligand PIZOF(Figure 3.1). It is known that rotation of aromatic groups about triple bonds occurs over vanishing (gas phase) intrinsic barriers and that these series of PIZOF have an excellent structural stability

that allows for the removal of solvent,[22] such that the rotational potential of the polar phenylene should be determined by interactions with the crystal lattice.

The PIZOF-2F structure can be described in terms of Zr_6O_8 clusters connected by 12 axial dicarboxylate ligands forming an interpenetrated structure with tetragonal and octahedral cavities. With expected dipole-dipole distances of 10 Å in a cubic lattice, PIZOF is expected to be isotropic and equally polarizable in all directions, which makes it an interesting dielectric crystalline material.

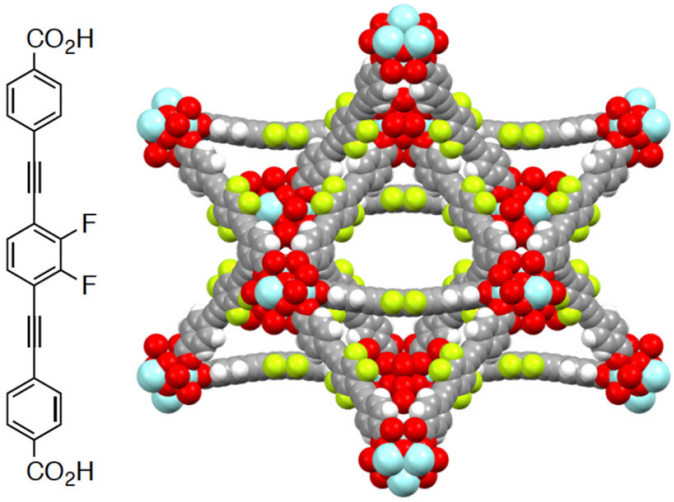

Figure 3.1: Line formula of the 4,4′-(1,4-phenylenebisethynyl)dibenzoic acid linker and X-ray structure of PIZOF-2F. H: white; C: gray; O: red; F: yellow; Zr: cyan.

3.3 Results and Discussion

3.3.1 Structure of PIZOF-2F

PIZOF-2F was prepared as previously reported, using the solvothermal method at 120 °C with acetic acid as a growth modulator (see experimental section). Relatively large crystals (Figure 3.2) suitable for single-crystal X-ray diffraction analysis and broadband dielectric spectroscopy were obtained after heating for 24 h. The X-ray structure solution was in full agreement with the one previously reported, with the organic linkers displaying a slight bending between metal linkers (ca. 8°). The fluorine atoms are rotationally disordered over two positions related by twofold rotational symmetry, such that only one metal and half of a ligand are needed to account for the asymmetric unit. Notably, as discussed below, fluorine atoms experience short contacts with hydrogen atoms from the carboxyphenyl group of adjacent linkers, indicating that rotations of the polar rotator are unlikely to be barrierless, despite the large pore volume.

Differential scanning calorimetry was acquired to observe any possible first-order phase change. Sample was heated from 30 °C to 80 °C first, then cooled down to -75 °C and heated to 30 °C again. No obvious phase change was observed.(Figure 3.3)

Figure 3.2: SEM of dried PIZOF-2F crystals at 12 kV.

3.3.2 Variable Temperature Solid State NMR

The first confirmation of fast rotational dynamics came from solid state cross- polarization and magic angle spinning (CPMAS) ^{13}C NMR measurement using the dipolar dephasing pulse sequence, which showed the aromatic signals even after a 50μs delay, suggesting a motionally averaged heteronuclear ^{1}H-^{13}C dipolar interaction. [23], [24] Additionally, variable temperature CPMAS ^{13}C NMR measurements showed broadening of the signal of the unsubstituted (Figure 3.5), flanking phenylene rings over a relatively narrow temperature range that can be assigned to spin–lattice relaxation in the rotating frame, suggesting hindered rotation with dynamics in the tens of KHz regime, in agreement with recently published results using ^{2}H NMR quadrupolar line shape analysis.[25] Attempts to measure the temperature-dependence of the rotational dynamics of the difluorophenylene rotator using variable temperature spin–lattice relaxation ^{19}F NMR or line shape analyses of quadrupolar ^{2}H NMR spectra were not successful due to their low content in the sample. For-

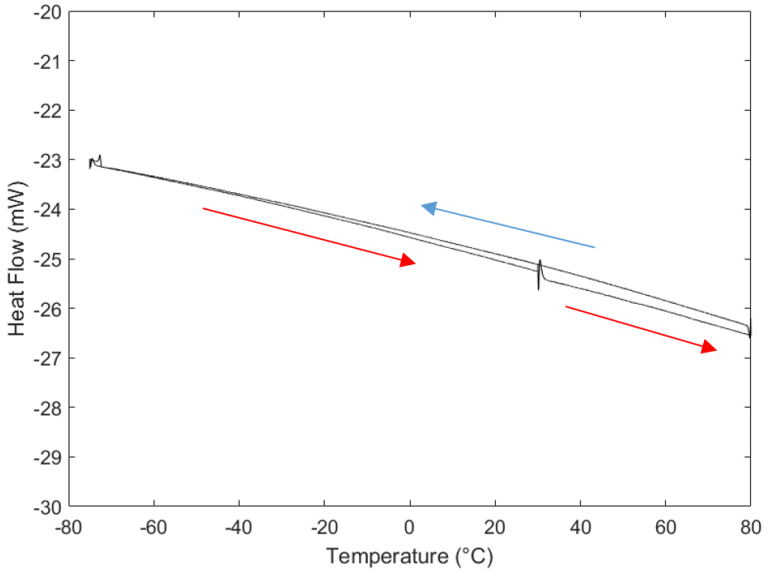

Figure 3.3: Differential scanning calorimetry (DSC) data of PIZOF-2F.

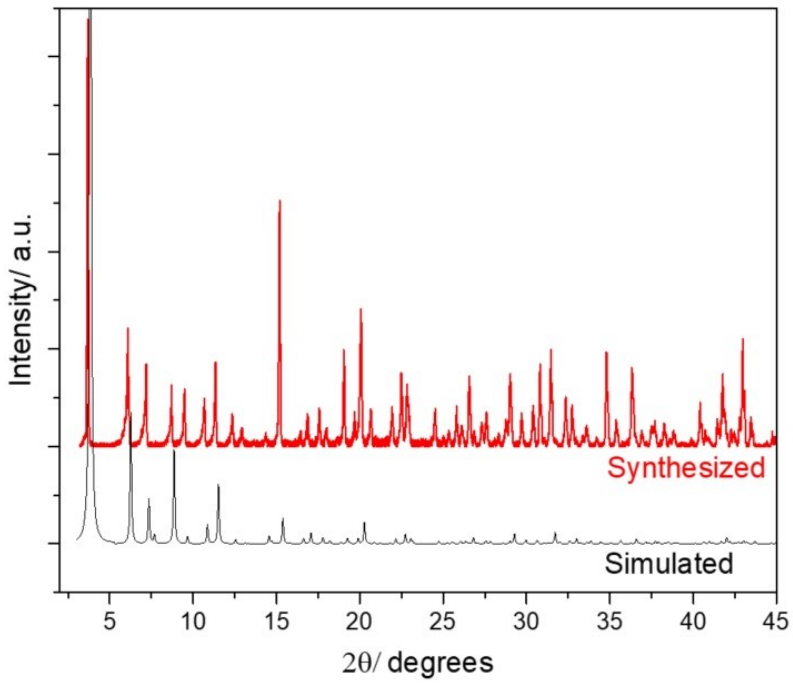

Figure 3.4: Simulated and measured Powder X-ray Diffraction pattern of PIZOF-2F

tunately, frequency- and temperature-dependent broadband dielectric spectroscopy provided us with the information required to analyze the rotational dynamics and activation parameters of PIZOF-2F.

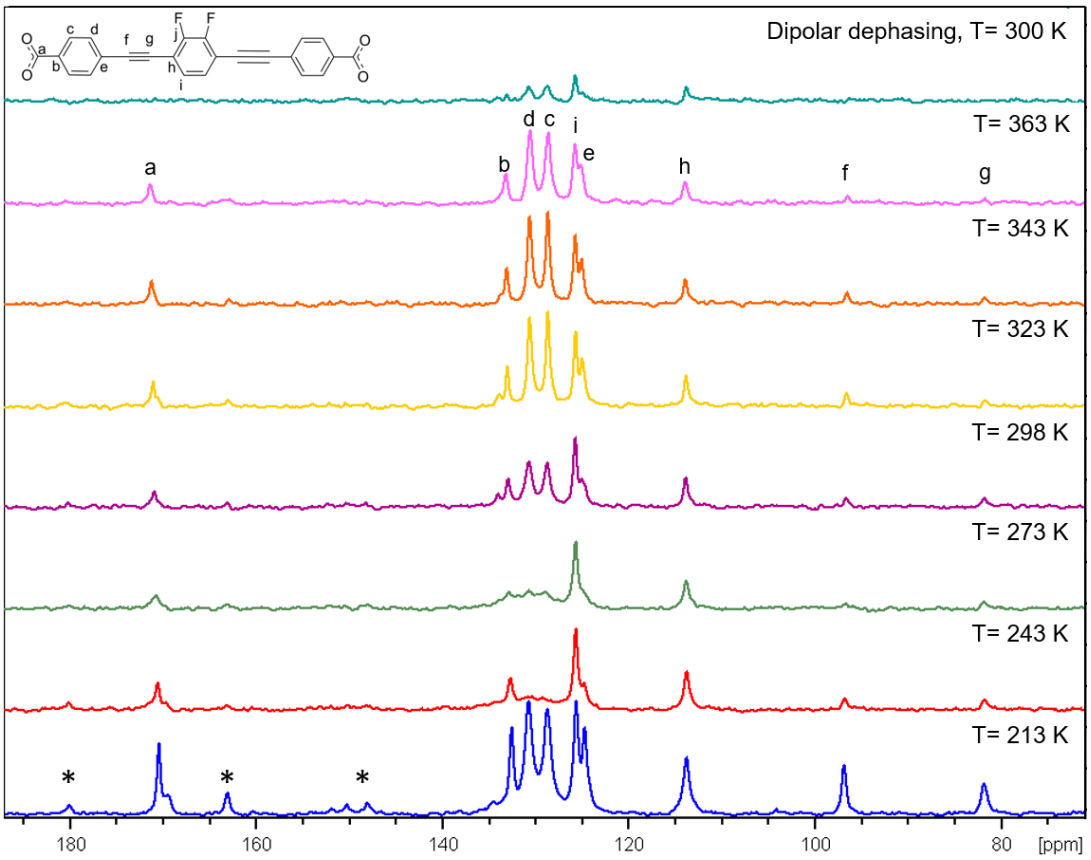

Figure 3.5: Variable temperature ^{1}H-^{13}C CPMAS spectra acquired by Bruker AV600SS magnet and 3.2 mm 600WB DVT HXY MAS probe. Contact time, 2ms. MAS rate, 10 kHz. Top spectrum was acquired with a dipolar dephasing sequence at room temperature with a dephasing delay of 50 μs. Disappearance and reappearance of phenylene carbons c and d near 243 K is due to resonance between slow dynamics of c and d and their frequencies in Hartmann-Hahn condition (c.a. 20 kHz).*: Spinning side bands.

3.3.3 Variable Temperature Broadband Dielectric Spectroscopy

Broadband dielectric measurements were carried out between 113 and 153 K at AC-field frequencies that varied from 10^3 to 10^6 Hz . Measurements of the real and imaginary parts of the complex dielectric, $\epsilon^{'}$ and $\epsilon^{''}$ showed that the system remained in a paraelectric phase with no ordering phase transition occurring within the temperature limits observed in our analysis. The dielectric relaxation is attributed to the rotation of the difluorophenylene dipoles, because all other dipoles from linker molecules are too weak, and the Zr atoms have an effectively spherical electron distribution. The dissipation factor (D) was calculated from $D = tan\delta = \epsilon^{''}/\epsilon^{'}$. The dissipation factor represents the energy loss as a result of the resistance presented to the field-induced polarization by a dielectric material. At any given temperature, the dissipation curve reaches a maximum when the frequency of the rotating dipole matches the frequency of the AC field applied to the sample. One can see from Figure 3.6(a) that Brownian rotation of the polar difluorophenylene at 313 K occurs, on average, at a frequency of $3 \times 10^5 s^{-1}$, where the curve reaches a maximum, although the width of curve indicates a significant dispersion.

Conventionally, this analysis is repeated at several temperatures, and one plugs the temperature-dependence of the peak frequencies to an Arrhenius equation to analyze rotational dynamics that assume a single activation energy, as expected for an ideal Debye model. However, given that the temperature and frequency limits of our instrument do not cover the range of dissipation maxima needed, we can estimate the maximum for five temperature values by assuming the same line shape

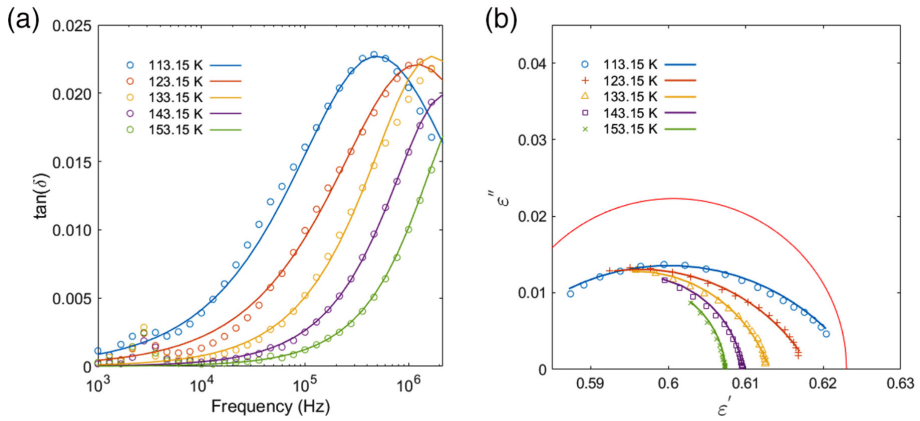

Figure 3.6: (a) Experimental (markers) and fitted (lines) tangent loss vs frequency at various temperatures. (b) Experimental (markers) and fitted (lines) Cole–Cole plot showing parts of the expected semicircles (the real part of permittivity is smaller than 1, because crystalline MOF powder cannot fill the space between the parallel plate capacitor).

with a shift that can be estimated from the position of slope. The temperature

Table 3.1: Temperature dependency of shifting factor a

Temperature/ K	113.15	123.15	133.15	143.15	153.15
a	1	0.34	0.17	0.10	0.04

dependency of dissipation peak frequencies is extracted from the plot and plugged in to Arrhenius equation: $\ln(f) = -E/RT + \ln(A)$, where f is peak frequency, R is gas constant, E is activation energy, A is pre-exponential factor. This method can still be applied to the dissipation data of PIZOF-2F by calculating temperature dependency of shifting factors though peak frequencies are not visible in the plot. After multiplying frequency data by a shifting factor a, slopes at higher temperatures

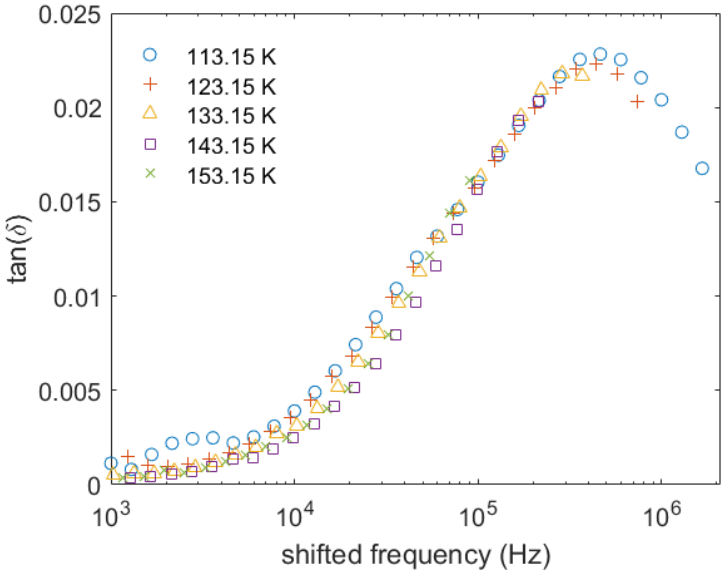

Figure 3.7: Dissipation factor plotted with frequency shifted by a factor of a at various temperatures.

can be brought to overlap with the slope of 113.15K (Table 3.1 and Figure S6). Under the assumption that lineshape remains identical, Arrhenius relations for higher temperatures become $\ln(f/a) = -E/RT + \ln(A)$). Therefore, energy barrier E can still be derived from slope of $\ln(1/a) = -E/RT + \ln(A/f)$.

This analysis suggests an activation energy of approximately $E_a = 2.6$ kcal/mol ($R^2 = 0.989$, Figure , blue line). Considering the very low electronic barriers for rotation about triple bonds,[26], [27] it is likely that the activation energy in the case PIZOF-2F is related to interactions with the environment. However, recognizing that the width of the dissipation data is broader than the one expected for a single relaxation process in a simple Debye model, we turned to the Cole–Cole relaxation model in order to account for the heterogeneity of the relaxation data.[28]

The Cole–Cole relaxation is an empirical model modified from the Debye model, which is described by the following equation:

$$\epsilon^* = \epsilon^{'} - i\epsilon^{''} = \epsilon_\infty + \frac{\epsilon_s - \epsilon_\infty}{1 + (i\omega\tau)^(1-\alpha)}\,, \tag{3.1}$$

where ϵ^* is the complex dielectric constant, ϵ_s is static dielectric constant, ϵ_∞ is the infinite frequency dielectric constant, $i = \sqrt{-1}$, ω is the frequency of the external AC field, τ is a microscopic relaxation, and $\alpha(0 \leq \alpha \leq 1)$ is an exponential factor that changes the standard Debye model (when $\alpha = 0$) to a broadened shape. In the Cole–Cole plot, $\epsilon^{''}$ is plotted against $\epsilon^{'}$ to obtain the deviation from a symmetric semicircle that depends on the magnitude of the parameter α. (Figure 3.6(b)) While full Cole–Cole semicircles could not be obtained as some the data falls outside of the material response range due to high rotational rates, the available data was fitted to the Cole–Cole equation to qualitatively explore its deviation from a Debye model on the right halves of semicircles. Solid lines in Figure 3.6(b) fit the experimental data reasonably well. From these fitting parameters, one can obtain a series of τ as a function of temperature. Under a linear response approximation, we equate macroscopic relaxation time τ to a microscopic time τ_μ related to the dipole jump time constant, [29] which we then use to build an Arrhenius plot, $\tau = \tau_0 \exp(E_a/k_B T)$ in order to determine the mean activation parameters (Figure 3.8). The pre-exponential factor τ_0 is associated with the jump attempt frequency, giving a time constant with a value of $7.33 \times 10^{-11} s^{-1}$, and the activation energy E_a needed to overcome the rotational barrier has a mean value of 1.9 kcal/mol (see other parameters derived from the fitting in Table 3.2). Notably, while the data is rather limited, and the uncertainty

is high, the values of α in the Cole–Cole fit decrease from 0.30 to 0.04 as temperature rises from 113.15 to 153.15 K (Table 3.2), suggesting a significant reduction in the heterogeneity of the rotational dynamics at the higher temperatures.

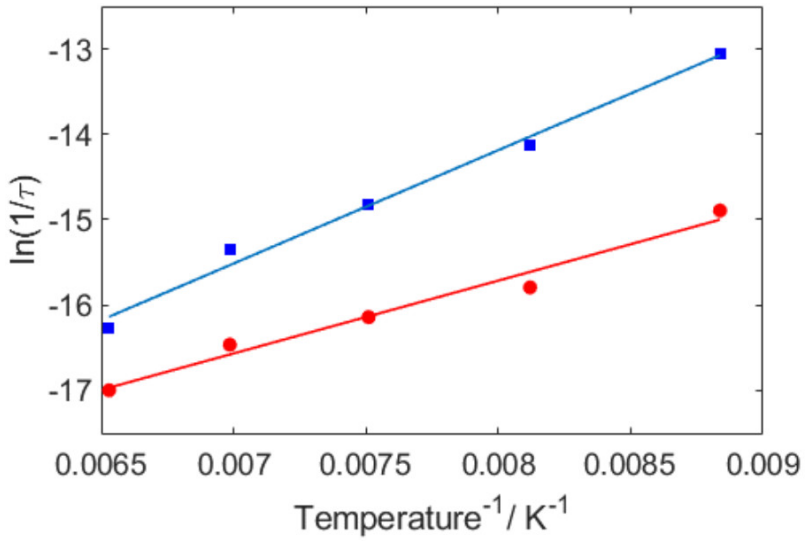

Figure 3.8: Arrhenius plots obtained from relaxation times as a function of temperature derived from $tan(\delta)$ values (blue, $E_a = 2.6$ kcal/mol) and from Cole–Cole fitting (red, 1.9 kcal/mol).

While a detailed analysis is hampered by the limited data, the results in Figure 3.6 and Figure 3.8 strongly suggest that the dielectric response of PIZOF-2F arises from a dipolar difluorophenylene rotator that overcomes relatively small activation barriers and is subject to significant heterogeneities. Our observations are consistent with results obtained with a nonpolar phenylene analogue measured with quadrupolar echo ^{2}H NMR by Rodríguez-Molina and co-workers, [25] which was shown to have rotational motion in fast exchange regime ($\tau^{-1} > 10^8\,s^{-1}$) at 298 K. Potential reasons for the rotational heterogeneity PIZOF-2F may result from struc-

tural factors related to a distribution of sites that have a range of potential energy profiles or from factors related to temperature-dependent framework motions that mediate the site exchange process.

Table 3.2: Parameters derived from Cole-Cole fitting at various temperatures.

Temperature/K	ϵ_s	ϵ_∞	τ / Hz	α
113.15	0.6192	0.5744	3.40E-07	0.6955
123.15	0.6156	0.5728	1.38E-07	0.7008
133.15	0.6135	0.5784	9.74E-08	0.8360
143.15	0.6088	0.5812	7.05E-08	0.9042
153.15	0.6074	0.5825	4.13E-08	0.9597

3.3.4 Structural Relation of Dynamic Behaviors

X-ray diffraction analysis of PIZOF-2F of a structure previously acquired at 100 K (21) reveals two well-defined positions for the polar difluorophenylene, suggesting that rotation occurs in the form of discrete 180° jumps between two degenerate minima (Figures 3.9 and 3.10). Analysis of diffraction data acquired at 180 and 298 K in this work revealed the same results, with no changes in the disorder of the fluorine atoms observed. A close inspection of the structure reveals a molecular rotor that bends substantially from the plane of the two carboxylates in order to form a C–H···F–C hydrogen bonding interaction with H···F distances between the central

rotator and four adjacent linkers that change from 2.702 Å at 100 K to 2.804 Å at 180 K and to 2.829 Å at 298 K (Figure 3.9). Furthermore, the boundaries of the difluorophenylene rotator are the empty pore on one side and a relatively crowded structure on the other, as illustrated by the three views of the space-filling models in Figure 3.10. A four-arm cavity is created by four neighboring ligands that act as the C–H···F–C hydrogen bond donors, suggesting that the relatively small activation energy required for PIZOF-2F rotation is likely to reflect the dissociation of the C–H···F–C hydrogen bonds to allow for an outward bending and subsequent rotation of the 1,4-bis(p-carboxyphenyl-ethynyl)-2,3-difluorobenzene linker. Based

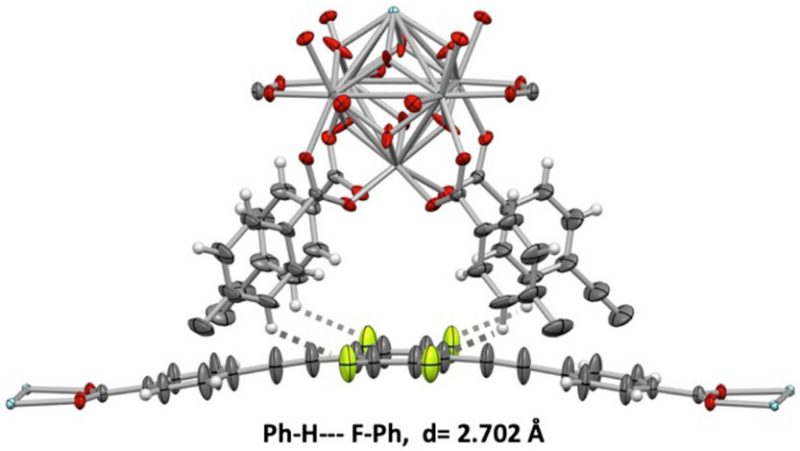

Figure 3.9: Close-up of the crystal structure of PIZOF-2F showing the C-H···F–C hydrogen bonds, the rotationally disordered position of the fluorine atoms, and the significant bending to the linker. We propose that rotation of the difluorophenylene relies on escaping the energy coupled with bending outward and rotation of the flanking phenylenes.

on the crystal structure, we suggest that the non-Debye relaxation and rotational

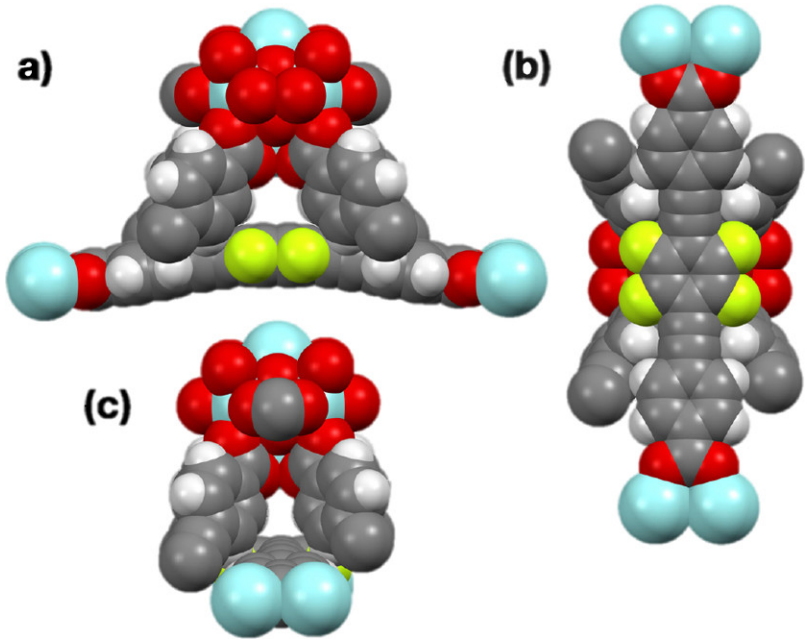

Figure 3.10: Space-filling models illustrating three orthogonal views of the local environment of the 1,4-bis(p-carboxyphenyl-ethynyl)-2,3-difluorobenzene rotor in the crystal structure of PIZOF-2F. (a) Same view as the one in Figure 4, with the pore empty volume at the bottom, (b) view from below the plane of the linker, and (c) view along the linker long axis, which is also the 2,3-difluorobenzene rotational axis.

heterogeneity as revealed by a temperature-dependent Cole–Cole α parameter in the case of PIZOF-2F may arise from temperature-dependent framework–rotator interactions. While heterogeneous dipolar rotation at low temperatures would be the result of a nonconstant potential energy surface determined by the dynamics of the framework, a dielectric response toward a single Debye relaxation at high temperatures would be consistent with a model where the dynamics of the environment are averaged within the time scale of dipolar rotation. In conclusion, we have shown that cubic crystals of PIZOF-2F allow for fast rotational motion of a difluorophenylene rotator, presenting opportunities for the development of crystalline high-frequency dielectric materials that could be amenable for isotropic field-induced polarization.

3.3.5 Deuterium Lineshape Analysis of Partially Deuterated PIZOF

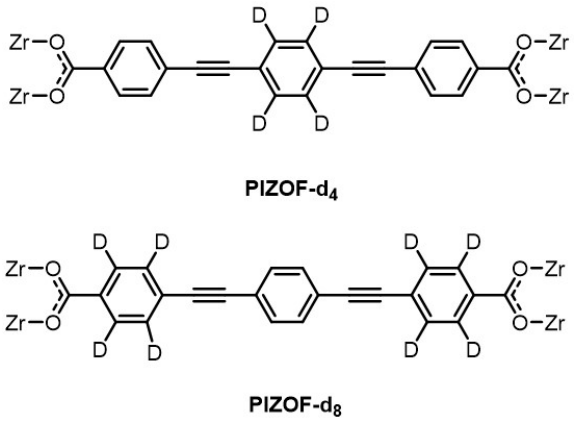

Figure 3.11: Partial deuteration of PIZOF ligand

In the collaboration with Prof. Braulio Rodriguez-Molina research group, we also characterized the dynamics of unfunctionalized phenylene rings in PIZOF. Ligand

with deuterated central phenylene ring or ligand with deuterated benzoate phenylene ring is incorporated into MOFs to give PIZOF-d_4 and PIZOF-d_8.(Figure 3.11) Deuterium lineshape analysis can detect dynamics between 10^3 and 10^7 Hz. Based on previously described study, the dynamics of central phenylene ring clearly falls out the capability of such measurement. The deuterium lineshape of PIZOF-d_4 still shows fast-limited motion at lowest temperature 160 (Figure 3.12) , which is in agreement of data from dielectric spectroscopy.

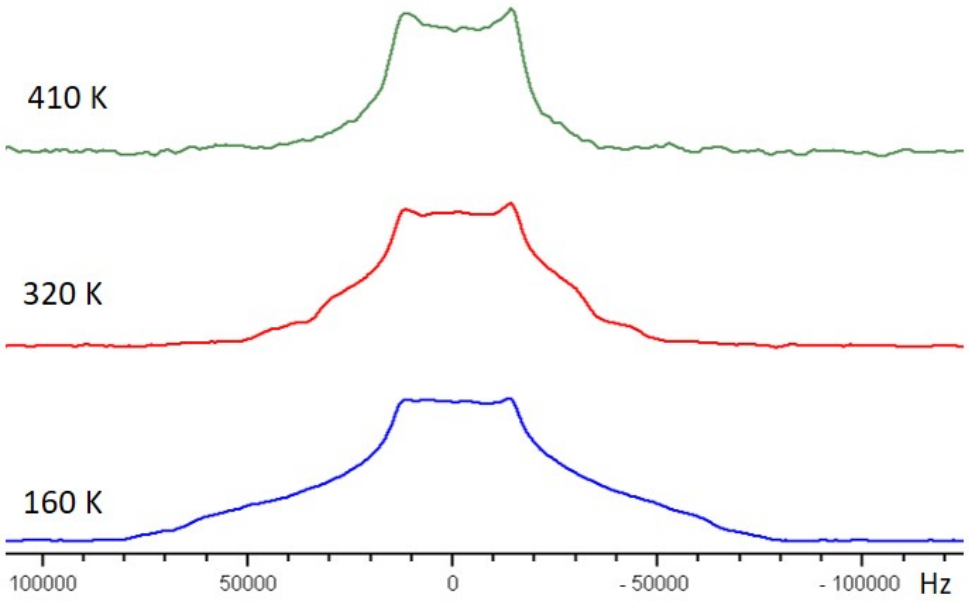

Figure 3.12: Deuterium lineshape analysis of PIZOF-d_4

Since the phenylene ring on the side is only bonded with one triple bond, it is expected to show slower dynamics and undergo a transition from slow exchange to fast exchange as temperature rises. Deuterium lineshapes of PIZOF-d_8 are acquired between 140 K and 350 K. Experimental results and simulations based on a 180 degree flip is shown in Figure 3.13. Arrhenius fitting from exchanging rate at

various temperatures indicates an energy barrier of 5.9 kcal/mol and pre-exponential factor of $2.14 \times 10^{11}\ s^{-1}$.

PIZOF-d4 was first measured

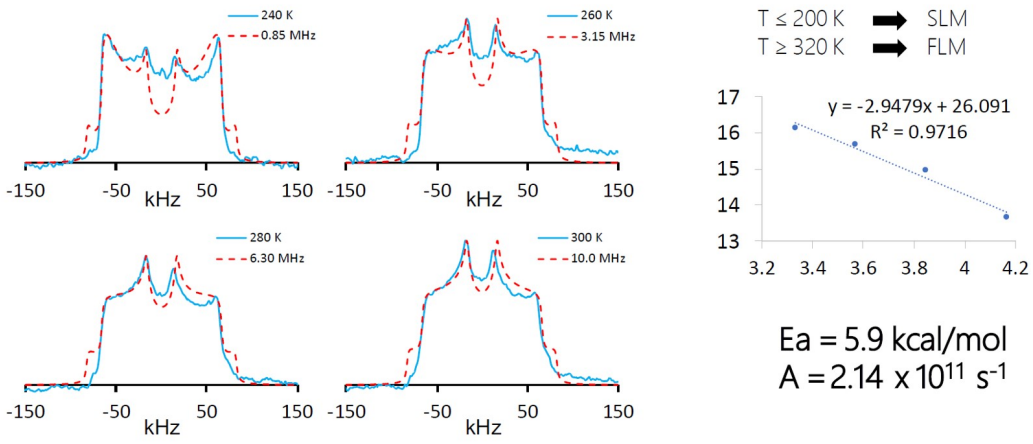

Figure 3.13: Deuterium lineshape analysis and arrhenius plot of PIZOF-d_8

3.3.6 PIZOF with Stronger Dipole

Given the result of PIZOF-2F, we seek to further increase the dipole-dipole strength and prevent interpenetration to allow a open space for dipolar rotors. A dinitro substituent on the central phenylene ring can potentially give the expected results. Therefore 4,4′-((2,3-dinitro-1,4-phenylene)bisethynyl)dibenzoic acid was synthesized and incorporated into PIZOF-2NO_2. The dinitrophenylene ligand has a more inert phenylene ring due to stronger electron withdrawing effect of dinitro group thus has lower activity and yield in synthesis. Also, synthetic conditions are different from that of PIZOF-2F possibly due to varied stacking behavior in solvothermal process. After modifications of synthetic pathways and solvothermal procedures

(see Experimental Sections), PIZOF-2NO_2 crystals was synthesized and activated. (Microscopic pictures in Figure 3.14). Single crystal data suggested that bulkier nitro group did not prevent interpenetration and crystal structure is very similar to PIZOF-2F. Therefore, the dynamics of PIZOF-2NO_2 was not investigated.

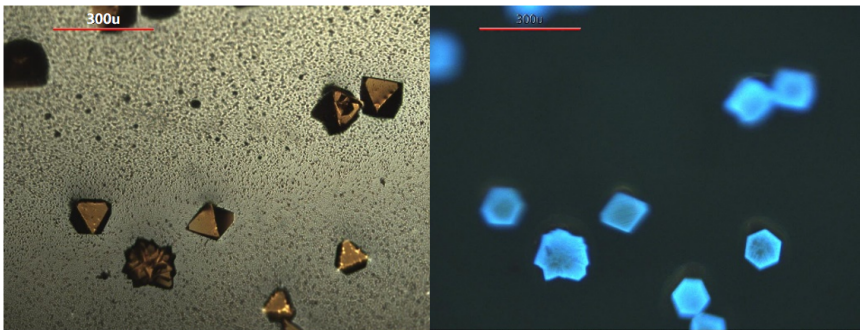

Figure 3.14: Microscopic pictures of PIZOF-2NO_2 crystals

We have also made attempts towards 2,3-diamino-5,6-dicyanophenylene dipole. However, possibly due to low electron density in the phenylene ring, the sonogashira coupling did not give desired product.

3.4 Experimental Sections

3.4.1 Syntheses of Ligands and MOFs

Synthesis of difluorophenylene linker:

4,4′-((2,3-difluoro-1,4-phenylene)bisethynyl)dibenzoic acid. 4 mL THF and 4 mL of triethylamine was mixed and then purged with argon for 20 min and added to a sealed tube in argon atmosphere. Then 1,4-diiodo-2,3-difluorobenzene (200 mg),

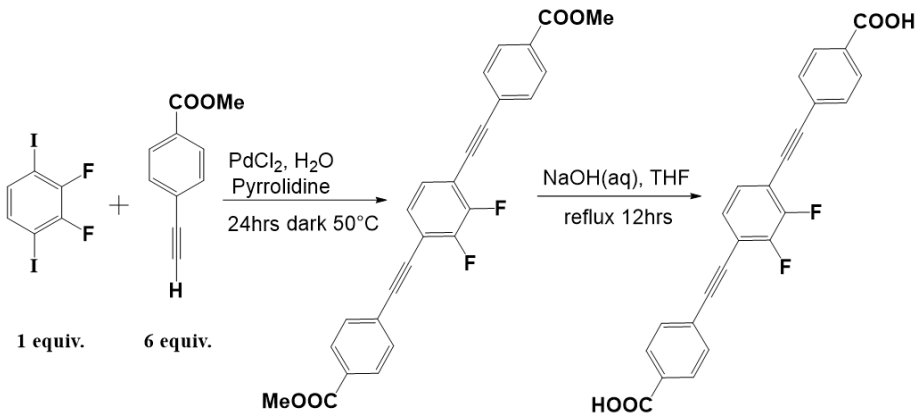

Scheme 3.1: Synthesis of difluorophenylene linker

methyl 4-ethynylbenzoate (262 mg), palladium(II) chloride triphenylphosphine (7 mg) and copper iodide (28 mg) was added to the sealed tube and the purging continued for another 10 minutes. The sealed tube was then heated to 50 °C for 24 hours. After it cooled down to room temperature, 10 mL of dichloromethane was added. The reaction mixture was filtered through celite and concentrated under vacuum. The crude product was purified by column chromatography with 8:2 DCM: acetone. Yield: 64% 152mg. 19F decoupled ^{1}H NMR (300 MHz, $CDCl_3$) δ(ppm): 8.66 (m, 4H),7.42 (m, 4H), 7.30 (s, 2H), 2.16 (s, 6H). 19F NMR(282 MHz) δ(ppm) -133 (s, 2F).

100 mg of dibenzoate was added to 100 mL of THF in a 500 mL flask. Then 100 mL aqueous solution of NaOH was added to the flask. The mixture was refluxed at 70°C overnight. Dilute HCl was slowly added to the mixture to precipitate the dicarboxylic acid. After filtration and drying, 85 mg product (91%) was collected. ^{1}H NMR(500 MHz, DMSO) δ 8.00 (dd, 4H), 7.72(dd, 4H), 7.55(m, 2H) .^{13}C NMR(125 MHz, DMSO) δ(ppm) 166.80, 151.4, 149.21, 131.97, 129.85, 128.74, 125.28, 96.70,

83.55.

Synthesis of dinitrophenylene linker:

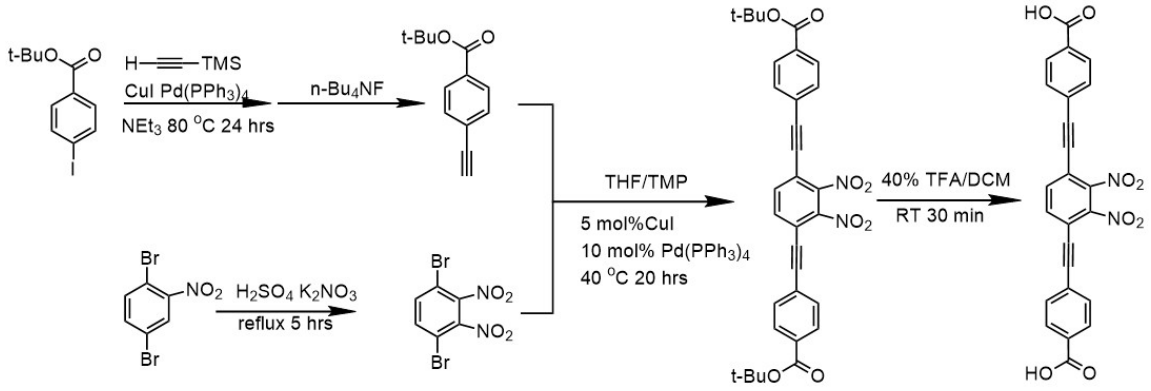

Scheme 3.2: Synthesis of dinitrophenylene linker

4-ethynylbenzoate tert-butylester. Followed procedures from [30]

1,4-dibromo-2,3-dinitrobenzene. 6 g of 1,4-dibromo-2-nitrobenzene and 16 g of potassium nitrate were added to a 250 mL round-bottom flask. Then 5mL of water and 100 mL concentrated sulfuric acid was slowly added to the flask. After a condenser was attached, the mixture was heated to 100 °C for 5 hours with constant stirring. After cooling down, 250 mL ice water was slowly added and the mixture was filted in a glass sintered funnel. The precipitate was collected and purified by column with 1:4 ethyl acetate:hexanes.400 mg light-yellow product was collected. ^{1}H NMR(500 MHz, DMSO) δ(ppm) 7.74 ppm(s, 2H).

4,4′-((2,3-dinitro-1,4-phenylene)bisethynyl)dibenzoate tert-butylester. 240 mg deprotected alkyne, 100 mg dibromodinitrobenzene, 12 mg CuI and 70 mg $Pd(PPh_3)_4$ were added to an argon-purged mixture of 6 mL 2,2,6,6-tetramethylpiperidine (TMP)

and 6 mL THF under argon atmosphere in a sealed tube. After 20 hours at 40°C, the reaction mixture was filtered through silica plug and then purified by chromatography with 2:3 ethyl acetate:hexanes. 45 mg yellow crystals obtained. ^{1}H NMR(300 MHz, $CDCl_3$) δ(ppm) 8.04(m, 4H), 7.84(s, 2H), 7.63(m, 4H), 1.65 (s, 18H). Melting point 220 °C.

4,4′-((2,3-dinitro-1,4-phenylene)bisethynyl)dibenzoic acid. 50 mg of dibenzoate was added to 10 mL DCM in a vial. 2.5 mL trifluoroacetic acid was slowly added and the reaction mixture was stirred at room temperature for 30 min. The filtrate was washed with water until washout pH reached neutral and dried before d in MOFs synthesis. 42 mg yellow powder obtained. ^{1}H NMR(500 MHz, DMSO) δ(ppm) 8.22(s, 2H), 8.03(d, 4H),7.71(d, 4H). ^{13}C NMR (125 MHz, DMSO) δ(ppm) 166.68, 144.00, 137.13, 132.34, 132.28 129.97, 124.47, 117.78, 98.84, 83.92.

Synthesis of PIZOF-2F: In a 3-dram Teflon capped vial 15 mg $ZrCl_4$ and 2 mL DMF were added. After dissolution, 12 mg of linker and 0.5 mL of acetic acid was added. The vial was sonicated for 10 min and placed in oven preheated to 120 °C for 24 hours. After cooling down, solvent exchange was conducted with fresh DMF and acetone. Crystals in acetone was then dried under vacuum at 120 °C for 12 hours.

Synthesis of PIZOF-2NO_2: In a 1-dram Teflon capped vial 8.5 mg $ZrCl_4$ and 2.5 mL DMF were added. After dissolution, 12 mg of linker was added and the vial was capped and sonicated until clear. Then 0.17 mL acetic acid was added. The vial was bubbled with argon for 5 min before heated to 110 °C for 40 hours. After cooling down, solvent exchange was conducted with fresh DMF and acetone. Crystals in

acetone was then dried under vacuum at 120 °C for 12 hours.

3.4.2 NMR Spectra

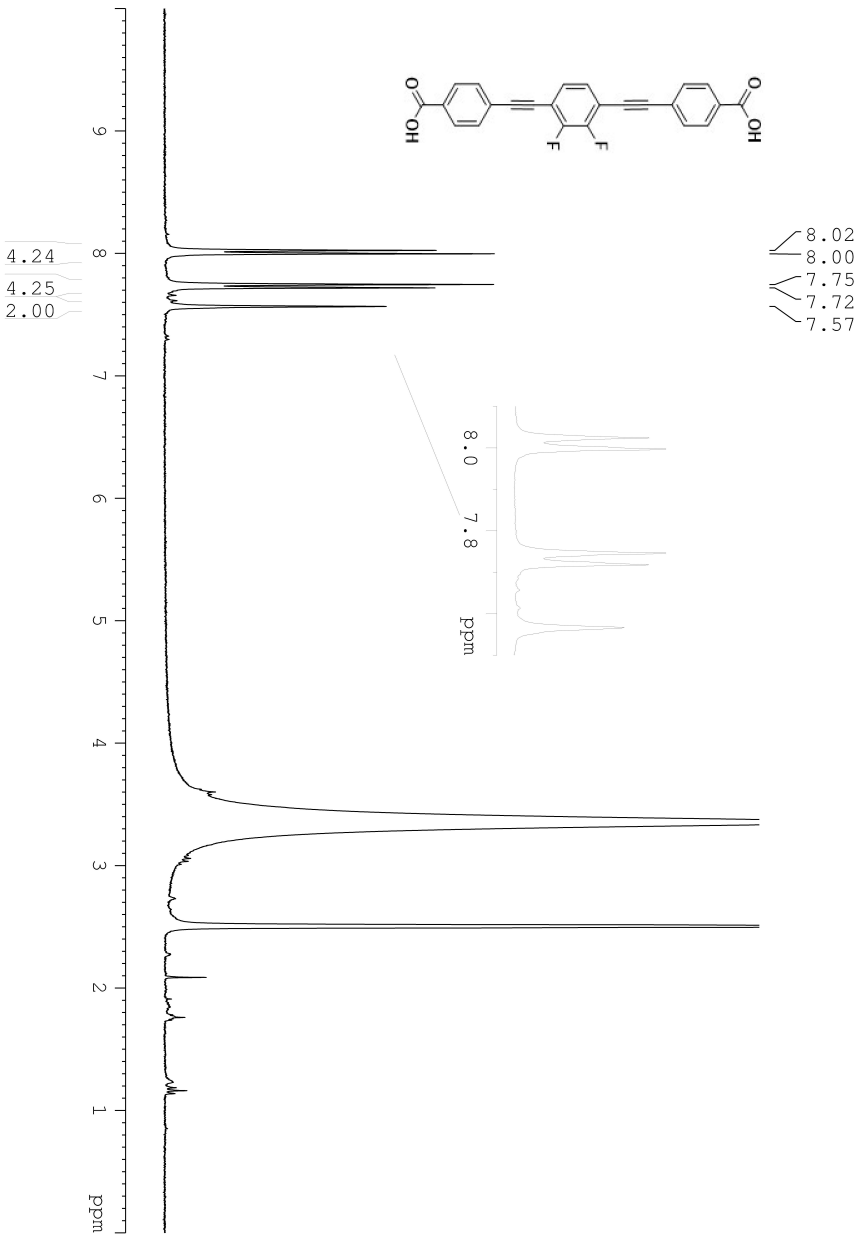

Figure 3.15: ^{1}H NMR (^{19}F decoupled at -130 ppm, 300 MHz, $CDCl_3$) of 4,4′-((2,3-difluoro-1,4-phenylene)bisethynyl)dibenzoic acid

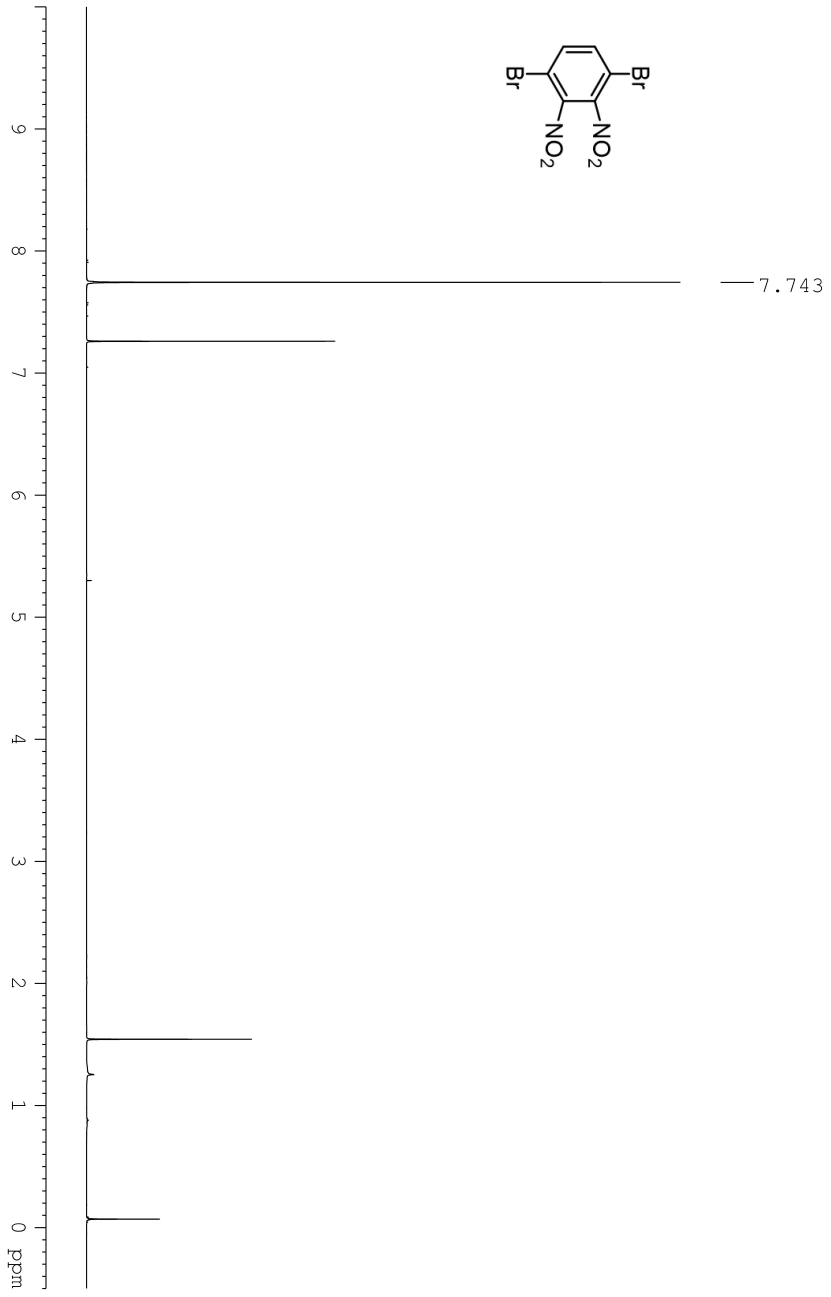

Figure 3.16: ^{1}H NMR (500 MHz, $CDCl_3$) of 1,4-dibromo-2,3-dinitrobenzene

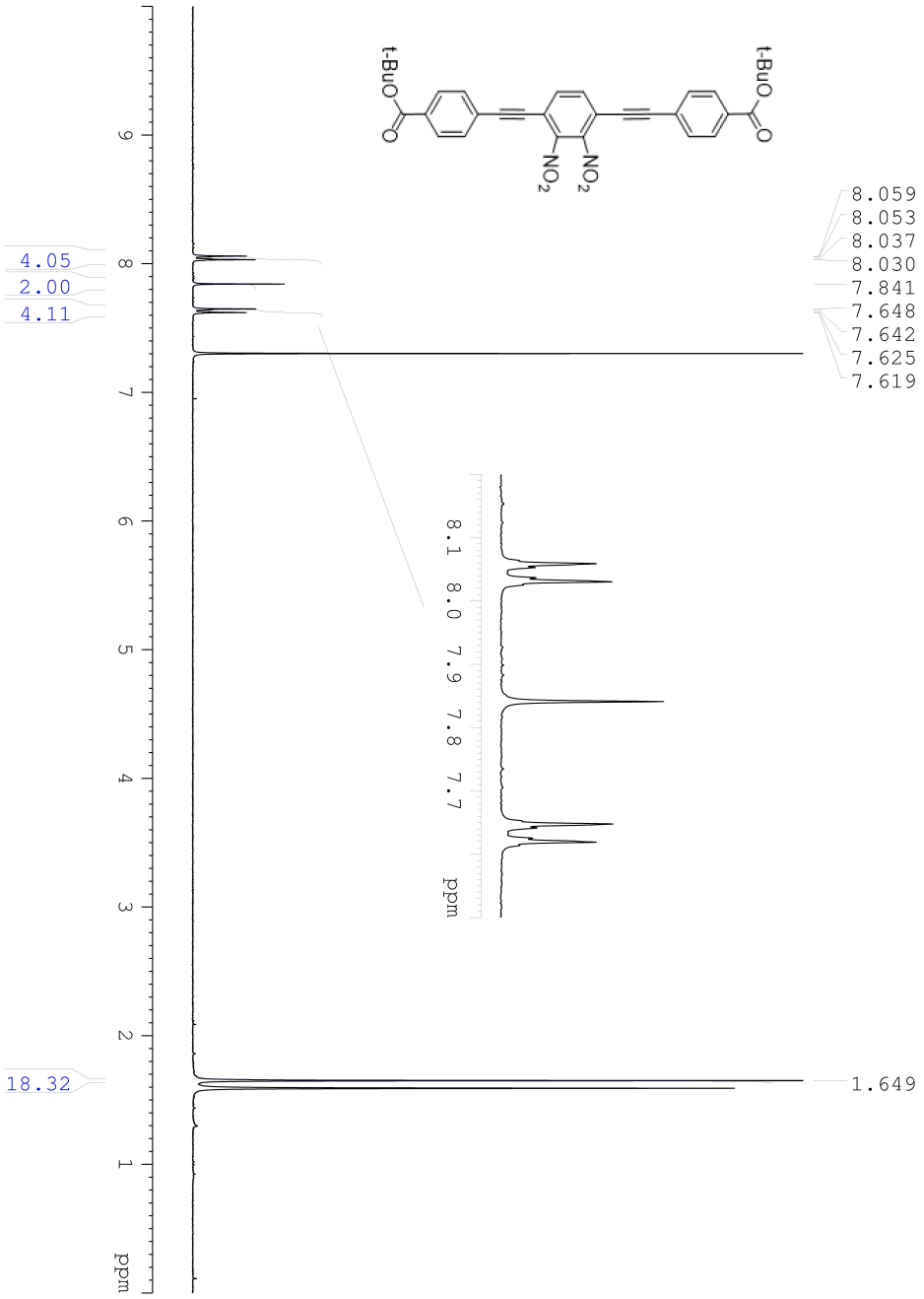

Figure 3.17: ^{1}H NMR (300 MHz, $CDCl_3$) of 4,4′-((2,3-dinitro-1,4-phenylene) bisethynyl) dibenzoate tert-butylester

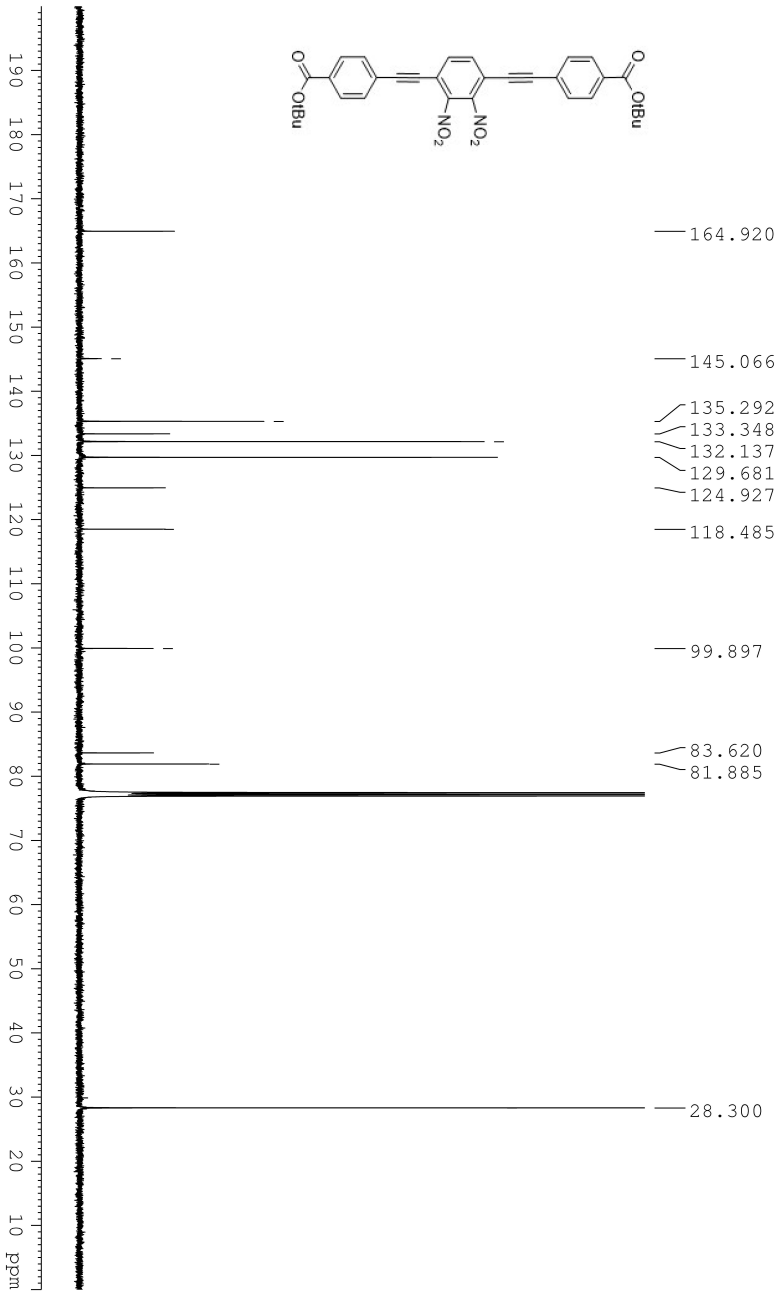

Figure 3.18: ^{13}C NMR (125 MHz, $CDCl_3$) of 4,4′-((2,3-dinitro-1,4-phenylene) bisethynyl) dibenzoate tert-butylester

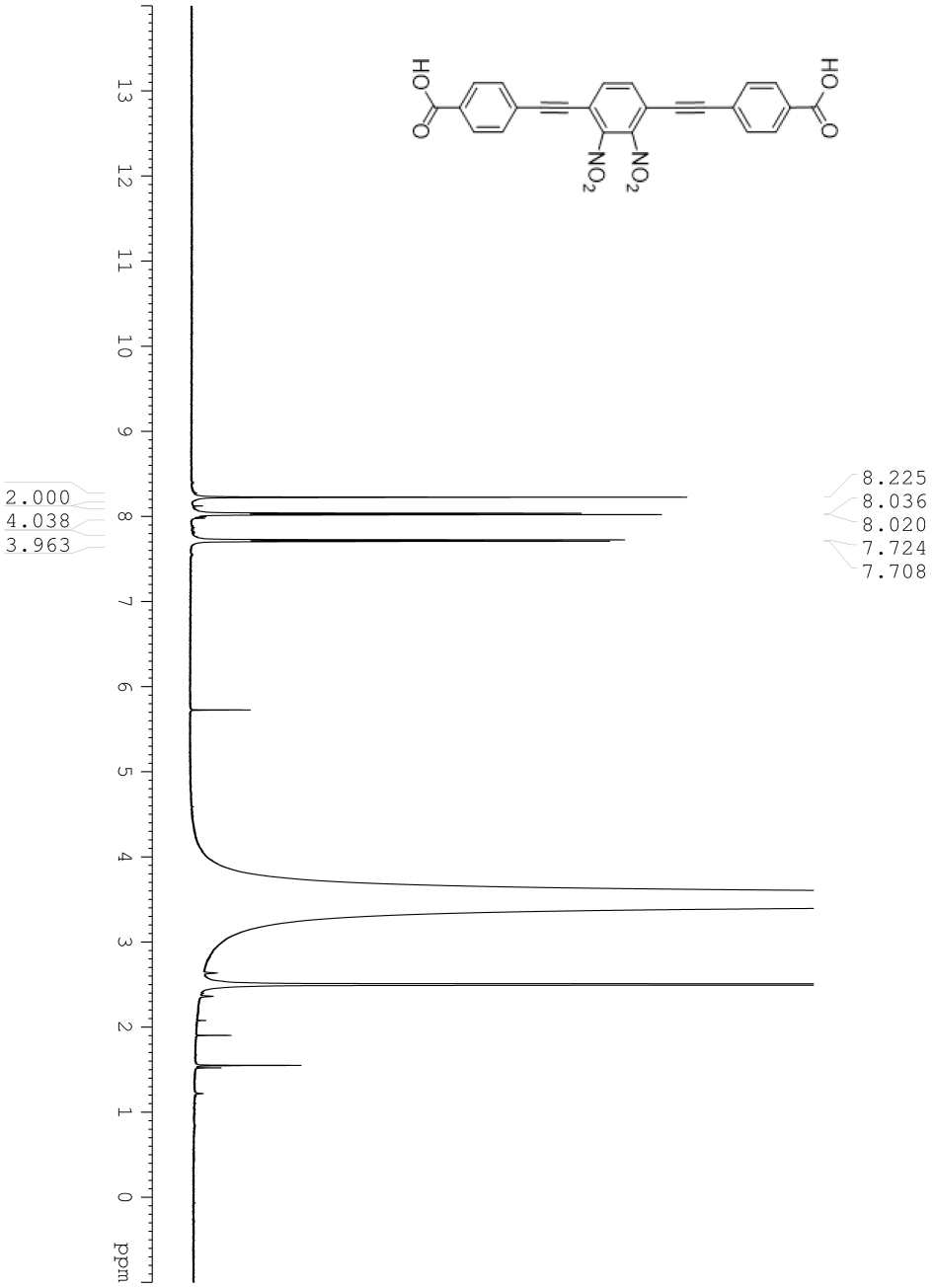

Figure 3.19: ^{1}H NMR (500 MHz, DMSO) of 4,4′-((2,3-dinitro-1,4-phenylene) bisethynyl) dibenzoic acid

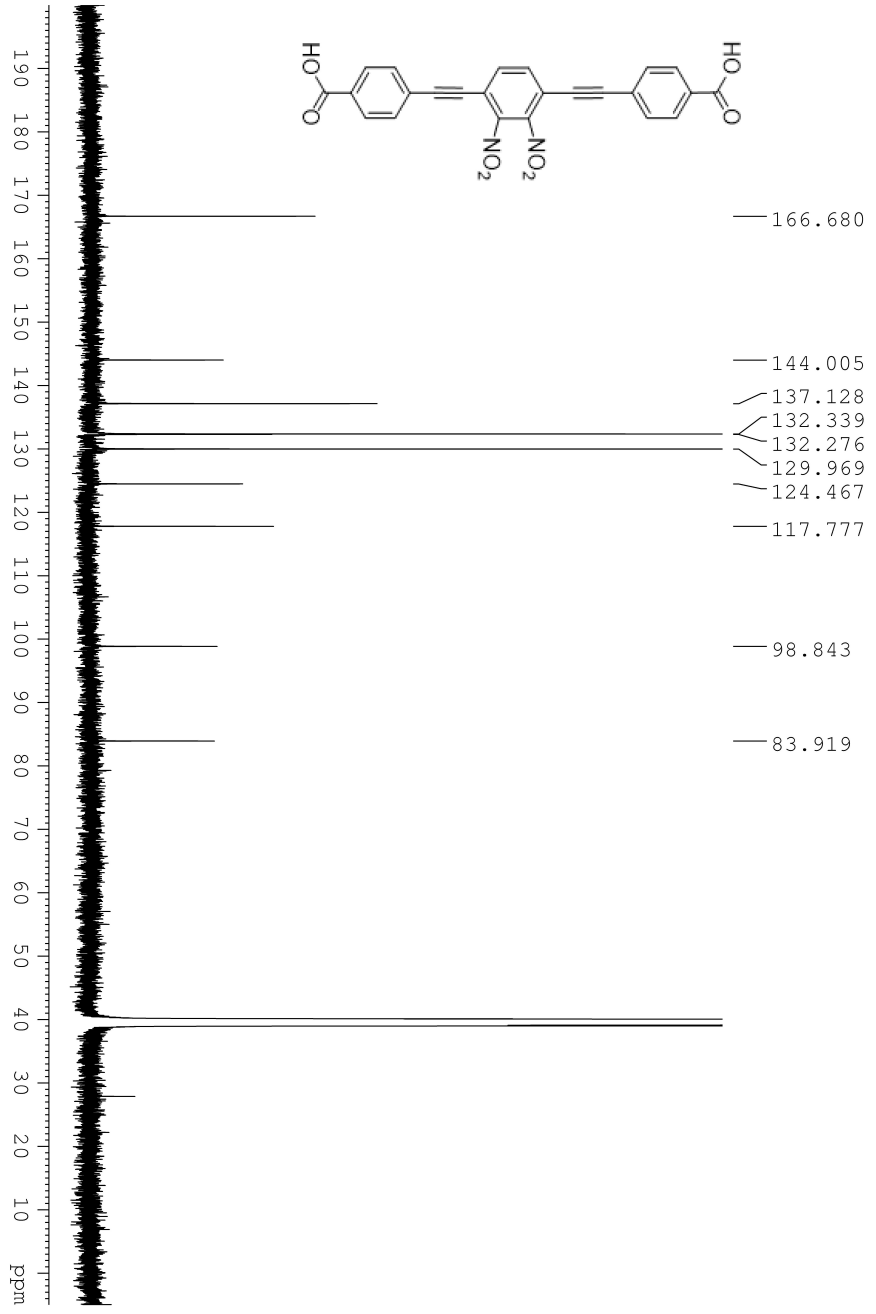

Figure 3.20: ^{13}C NMR (125 MHz, DMSO) of 4,4′-((2,3-dinitro-1,4-phenylene) bisethynyl) dibenzoic acid

3.4.3 X-ray Structures

Complete cif files are availabe free of charge via www.ccdc.cam.ac.uk/structures. Deposition number are 2088393, 2088394.

Table 3.3: Crystallographic data of PIZOF-2F acquired at 180 K and 298 K with Bruker APEX-II CCD Mo K_α beam. Refined with SHELXL 2014/6.

Temperature/K	180	298
Crystal System	cubic	cubic
Space Group	$Fd\bar{3}m$	$Fd\bar{3}m$
a/Å	39.846	39.823
b/Å	39.846	39.823
c/Å	39.846	39.823
α/Å	90	90
β/Å	90	90
γ/Å	90	90
V/Å^3	63262	63156
Z	48	48
Reflections used	9373	9693
R_f	6.36%	7.46%

References

[1] C. S. Vogelsberg and M. A. Garcia-Garibay, "Crystalline molecular machines: Function, phase order, dimensionality, and composition," *Royal Society of Chemistry*, vol. 41, no. 5, pp. 1892–1910, 2012.

[2] V. N. Vukotic, K. J. Harris, K. Zhu, R. W. Schurko, and S. J. Loeb, "Metal–organic frameworks with dynamic interlocked components," *Nature Chemistry*, vol. 4, no. 6, pp. 456–460, 2012.

[3] A. Comotti, S. Bracco, T. Ben, S. Qiu, and P. Sozzani, "Molecular rotors in porous organic frameworks," *Angewandte Chemie*, vol. 126, no. 4, pp. 1061–1065, 2014.

[4] L. Catalano and P. Naumov, "Exploiting rotational motion in molecular crystals," *CrystEngComm*, vol. 20, no. 39, pp. 5872–5883, 2018.

[5] M. E. Howe and M. A. Garcia-Garibay, "The roles of intrinsic barriers and crystal fluidity in determining the dynamics of crystalline molecular rotors and molecular machines," *The Journal of Organic Chemistry*, vol. 84, no. 16, pp. 9835–9849, 2019.

[6] S. L. Gould, D. Tranchemontagne, O. M. Yaghi, and M. A. Garcia-Garibay, "Amphidynamic character of crystalline mof-5: Rotational dynamics of terephthalate phenylenes in a free-volume, sterically unhindered environment," *Journal of the American Chemical Society*, vol. 130, no. 11, pp. 3246–3247, 2008.

[7] X. Jiang, H.-B. Duan, S. I. Khan, and M. A. Garcia-Garibay, "Diffusion-controlled rotation of triptycene in a metal–organic framework (mof) sheds light on the viscosity of mof-confined solvent," *ACS central science*, vol. 2, no. 9, pp. 608–613, 2016.

[8] E. B. Winston, P. J. Lowell, J. Vacek, J. Chocholoušová, J. Michl, and J. C. Price, "Dipolar molecular rotors in the metal–organic framework crystal irmof-2," *Physical Chemistry Chemical Physics*, vol. 10, no. 34, pp. 5188–5191, 2008.

[9] C. S. Vogelsberg, F. J. Uribe-Romo, A. S. Lipton, *et al.*, "Ultrafast rotation in an amphidynamic crystalline metal organic framework," *Proceedings of the National Academy of Sciences*, vol. 114, no. 52, pp. 13 613–13 618, 2017.

[10] J. Perego, C. Bezuidenhout, A. Pedrini, *et al.*, "Reorientable fluorinated aryl rings in triangular channel fe-mofs: An investigation on co 2–matrix interactions," *Journal of Materials Chemistry A*, vol. 8, no. 22, pp. 11 406–11 413, 2020.

[11] J. Perego, S. Bracco, M. Negroni, *et al.*, "Fast motion of molecular rotors in metal–organic framework struts at very low temperatures," *Nature Chemistry*, vol. 12, no. 9, pp. 845–851, 2020.

[12] V. Rozenbaum, "Long-range orientational order in a two-dimensional degenerate system of dipoles on a square lattice," *Journal of Experimental and Theoretical Physics Letters*, vol. 63, no. 8, pp. 662–667, 1996.

[13] H. Cui, Z. Wang, K. Takahashi, Y. Okano, H. Kobayashi, and A. Kobayashi, "Ferroelectric porous molecular crystal,[mn3 (hcoo) 6](c2h5oh), exhibiting fer-

rimagnetic transition," *Journal of the American Chemical Society*, vol. 128, no. 47, pp. 15 074–15 075, 2006.

[14] Y. Zhang, W. Zhang, S.-H. Li, *et al.*, "Ferroelectricity induced by ordering of twisting motion in a molecular rotor," *Journal of the American Chemical Society*, vol. 134, no. 26, pp. 11 044–11 049, 2012.

[15] D.-W. Fu, W. Zhang, H.-L. Cai, *et al.*, "A multiferroic perdeutero metal–organic framework," *Angewandte Chemie International Edition*, vol. 50, no. 50, pp. 11 947–11 951, 2011.

[16] S. Horiuchi and Y. Tokura, "Organic ferroelectrics," *Nature materials*, vol. 7, no. 5, pp. 357–366, 2008.

[17] S. DeLeeuw, D. Solvaeson, M. A. Ratner, and J. Michl, "Molecular dipole chains: Excitations and dissipation," *The Journal of Physical Chemistry B*, vol. 102, no. 20, pp. 3876–3885, 1998.

[18] E. Sim, M. A. Ratner, and S. W. De Leeuw, "Molecular dipole chains ii," *The Journal of Physical Chemistry B*, vol. 103, no. 41, pp. 8663–8670, 1999.

[19] J. De Jonge, M. Ratner, S. De Leeuw, and R. Simonis, "Molecular dipole chains iii: Energy transfer," *The Journal of Physical Chemistry B*, vol. 108, no. 8, pp. 2666–2675, 2004.

[20] J. Vacek and J. Michl, "Artificial surface-mounted molecular rotors: Molecular dynamics simulations," *Advanced Functional Materials*, vol. 17, no. 5, pp. 730–739, 2007.

[21] R. D. Horansky, L. I. Clarke, E. B. Winston, *et al.*, "Dipolar rotor-rotor interactions in a difluorobenzene molecular rotor crystal," *Physical Review B*, vol. 74, no. 5, p. 054 306, 2006.

[22] R. J. Marshall, Y. Kalinovskyy, S. L. Griffin, C. Wilson, B. A. Blight, and R. S. Forgan, "Functional versatility of a series of zr metal–organic frameworks probed by solid-state photoluminescence spectroscopy," *Journal of the American Chemical Society*, vol. 139, no. 17, pp. 6253–6260, 2017.

[23] S. D. Karlen and M. A. Garcia-Garibay, "Amphidynamic crystals: Structural blueprints for molecular machines," in *Molecular Machines*, Springer, 2005, pp. 179–227.

[24] L. B. Alemany, D. M. Grant, T. D. Alger, and R. J. Pugmire, "Cross polarization and magic angle sample spinning nmr spectra of model organic compounds. 3. effect of the carbon-13-proton dipolar interaction on cross polarization and carbon-proton dephasing," *Journal of the American Chemical Society*, vol. 105, no. 22, pp. 6697–6704, 1983.

[25] A. Torres-Huerta, D. Galicia-Badillo, A. Aguilar-Granda, J. T. Bryant, F. J. Uribe-Romo, and B. Rodrıguez-Molina, "Multiple rotational rates in a guest-loaded, amphidynamic zirconia metal–organic framework," *Chemical Science*, vol. 11, no. 42, pp. 11 579–11 583, 2020.

[26] S. Saebø, J. Almlöf, J. E. Boggs, and J. G. Stark, "Two approaches to the computational determination of molecular structure: The torsional angle in

tolane and the effect of fluorination on the structure of oxirane," *Journal of Molecular Structure: THEOCHEM*, vol. 200, pp. 361–373, 1989.

[27] V. Sipachev, L. Khaikin, O. Grikina, V. Nikitin, and M. Trætteberg, "Structure, spectra and internal rotation of bis (trimethylsilyl) acetylene: Spectral analysis by scaling quantum-chemical force fields and two methods for calculating vibrational effects," *Journal of Molecular Structure*, vol. 523, no. 1-3, pp. 1–22, 2000.

[28] K. S. Cole and R. H. Cole, "Dispersion and absorption in dielectrics i. alternating current characteristics," *The Journal of chemical physics*, vol. 9, no. 4, pp. 341–351, 1941.

[29] G. Williams, "Use of the dipole correlation function in dielectric relaxation," *Chemical Reviews*, vol. 72, no. 1, pp. 55–69, 1972.

[30] T. C. Wang, W. Bury, D. A. Gómez-Gualdrón, *et al.*, "Ultrahigh surface area zirconium mofs and insights into the applicability of the bet theory," *Journal of the American Chemical Society*, vol. 137, no. 10, pp. 3585–3591, 2015.

CHAPTER 4

Rotational Dynamics of Dumbbell Shape Rotor-Stator Molecular Crystals

Unpublished work in collaboration with Prof. Shih-Ching Chuang research group. All molecular rotors are synthesized by Chuang and group member. Characterization and anaylsis of dynamics are performed by Liu and Garcia-Garibay.

4.1 Abstract

We synthesized a series of dumbbell-shape molecular rotor-stator crystals where tribenzotriquinacene stator cap both ends of the rotors: biphenyl, diphenylacetylene and diphenylbutadiyne. The rotational dynamics was studied both experimentally and computationally using ssNMR and DFT simulation. They reveal that diphenylacetylene and diphenylbutadiyne rotors have fast dynamics. Surprisingly, the tribenzotriquinacene stator is also dynamic within our experimental temperature range. DFT simulation on single molecule reveals an intrinsic barrier c.a. 0.8 kcal. As tribenzotriquinacene can function as a fullerene receptor, investigation on such

type of amphidynamic crystals will facilitate the design towards molecular machines with more complications.

4.2 Introduction

In close-packed crystalline molecular crystals, even volume-conserving rotations can be slow or hindered at times due to congested crystal environments.[1] In our previous studies, a linear geometry of triple bond linked phenylene ring is usually more restricted by such factor. Incorporating such motif into MOFs is a good supramolecular approach. However, in some cases, carefully chosen molecules can reduce packing density thus enable fast rotations. In this chapter, dynamics of molecular rotors featuring biphenyl/ diphenylacetylene/ diphenylbutadiyne rotor and bis-tribenzotriquinacene stator are investigated (Figure 4.1). While we anticipate the ethynyl group would has low intrinsic energy barrier, bulky tribenzotriquinacene groups can both reduced packing density and bring new possibilities as a receptor molecule in host-guest systems.[2], [3]

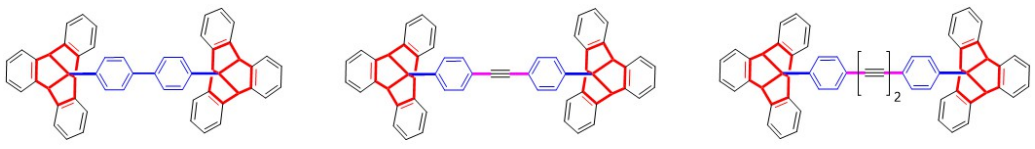

Figure 4.1: Structure of molecular rotor **0**, **1** and **2**

4.3 Results and Discussions

4.3.1 Variable-Temperature ^{1}H Broadline SSNMR

^{1}H wideline spectra of compound **0**, **1** and **2** are measured at various temperatures (Figure 4.2, 4.3 and 4.4). The first obvious feature is that lineshapes of all three compounds broadens as temperature rises. Peak width is broadened more than 20 kHz from lowest to highest temperature. Such broadening is attributed to local motion of protons which decreases chemical shift anisotropy. With bigaussian fitting of wideline spectra of compound **0** and **1**, one broad(green) and one sharp(red) component can be extracted for most temperatures (except failures on lowest temperature data where the broad component covers up the sharp component). The broad component is attributed to the tribenzotriquinacene stators while sharp component to the phenylene rotor. It can be observed that stator phenylene contributed to the majority of broadening. It indicates that stators are not 'static' as we anticipated. Their dynamics are activated by thermal energy hence the signal gradually shift towards a motion-averaged narrow peak. On the other hand, sharp signals of rotor protons are only slightly broadened, indicating that they possess fast dynamics even at lowest temperature. And by virtue of triple bond in compound **1**, phenylene rotors have lower energy barrier hence give sharper signal than **0**. Even though bigaussian fitting is not successful for spectra of **2**, in the stacked we can still observe that the a broad component narrows while a sharp component is not as sensitive to change in temperature.

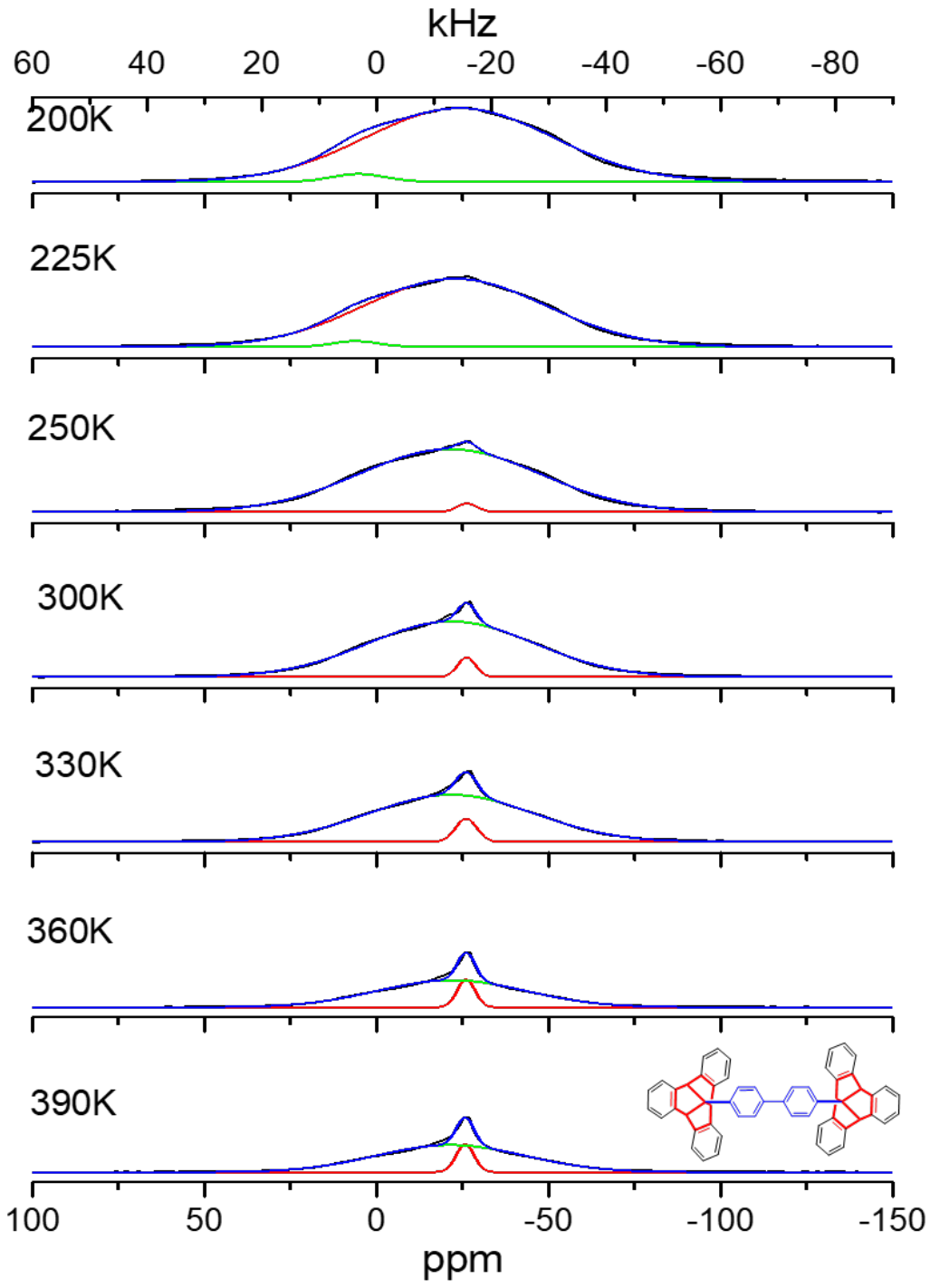

Figure 4.2: ^{1}H ssNMR broadline spectra of **0** with bigaussian fitting. (Fitting at 200 K and 225K failed)

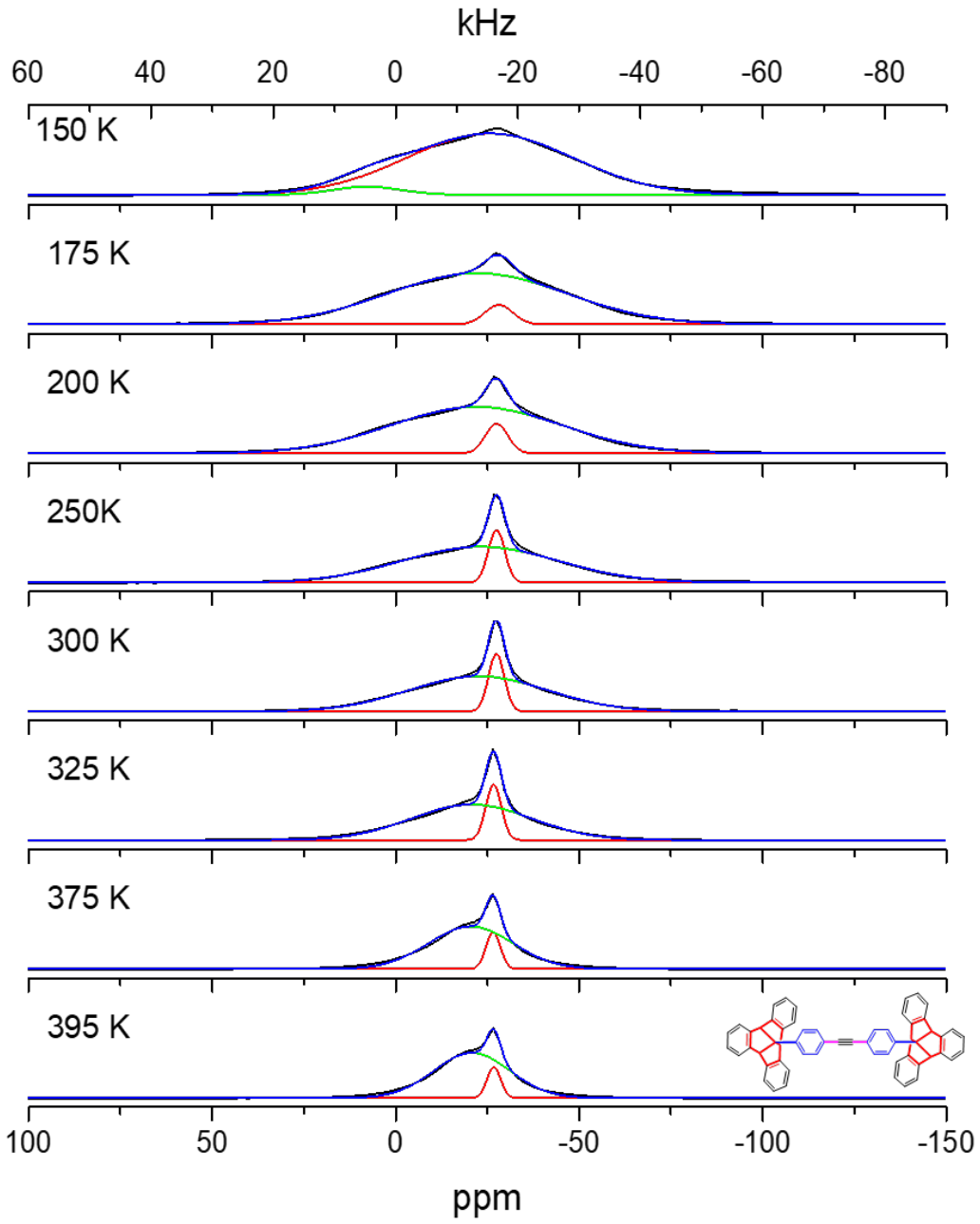

Figure 4.3: ^{1}H ssNMR broadline spectra of **1** with bigaussian fitting. (Fitting at 150 K failed.)

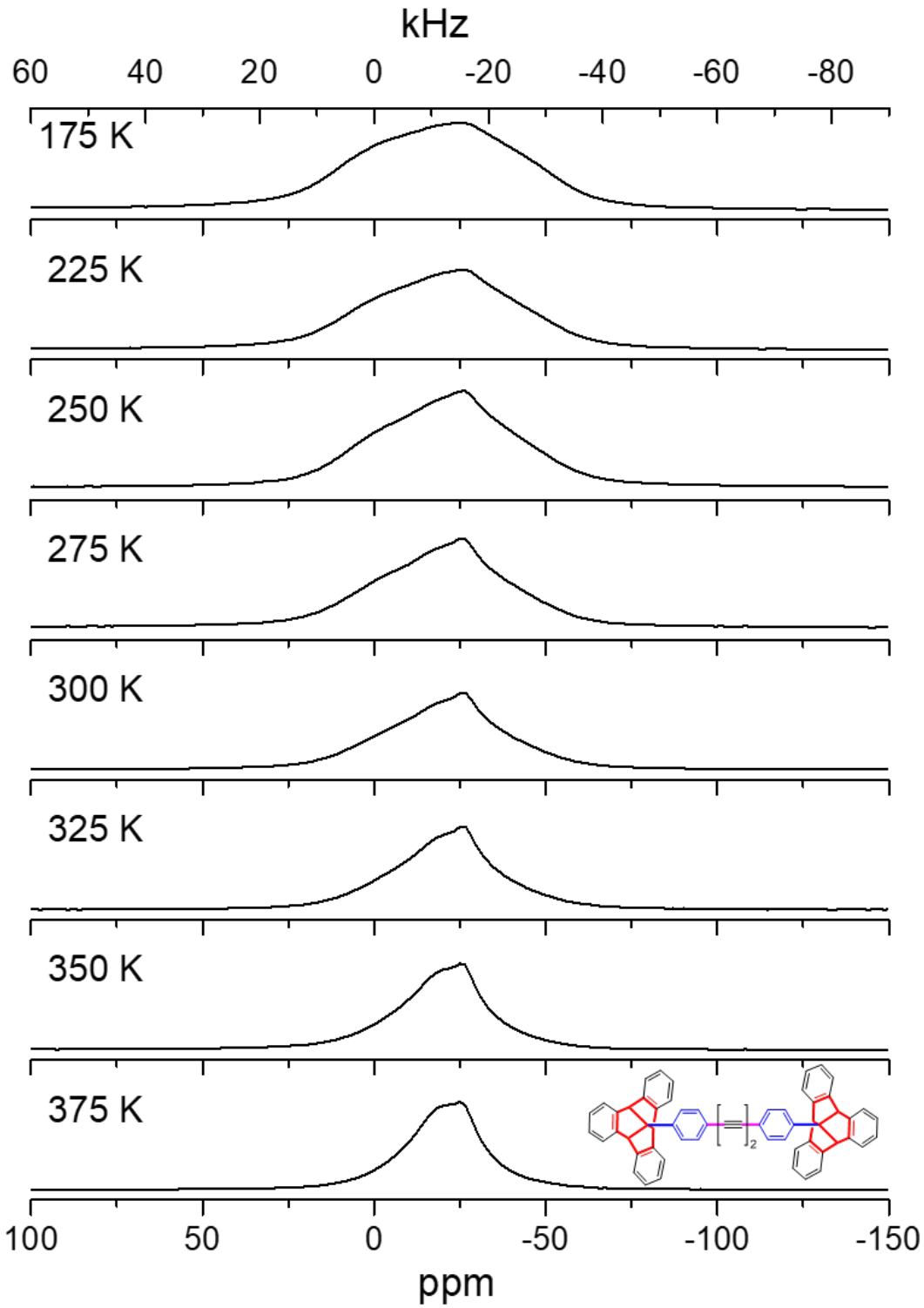

Figure 4.4: ^{1}H ssNMR broadline spectra of **2**.

4.3.2 Variable-Temperature ^{1}H-^{13}C CPMAS SSNMR

The variable temperature ^{1}H-^{13}C CPMAS spectra also confirm such findings. For **1** and **2**, peak of the tertiary carbon on stator coalesce to one single sharp peak(64 ppm), indicating a thermal-activated averaged motion (Figure 4.6 and 4.7). Interestingly, the tertiary carbon in compound **0** appears as two distinct peaks that are split by 350 Hz at 225 K, and as temperature rises, these two signals shift towards central position (Figure 4.7). Such phenomenon is most likely caused by different packing in crystal structure of **0**. The crystal structure of **0** probably adopts a lower symmetry which lead to split of the carbon signal.

4.3.3 Variable-Temperature ^{1}H Spin-Lattice Relaxation

Rotation gives additional mechanism to spin-lattice relaxation thus spin-lattice relaxation time (T1) has a temperature dependence which can be used to derive information on dynamics based on Kubo-Tomita relation.[4]

$$1/T_1 = C[\tau_c(1+\omega_0^2)\tau_c^2)^{-1} + 4\tau_c(1+4\omega_0^2\tau_c^2))^{-1}] \tag{4.1}$$

$$\tau_c = \tau_0 \exp E_a/RT \tag{4.2}$$

Compound **0**,**1**,**2** are measured between 175 K and 395 K. Only **1** shows a peak within the range. Kubo-Tomita fitting gives energy barrier of 1.0 kcal/mol and characteristic time τ_0 of 5.3×10^{-11}s (Figure 4.8). Fittings of T1 are shown in experimental section. Such relaxation can only be attributed to rotation of stator as the frequency would be too low for phenylene rotor.

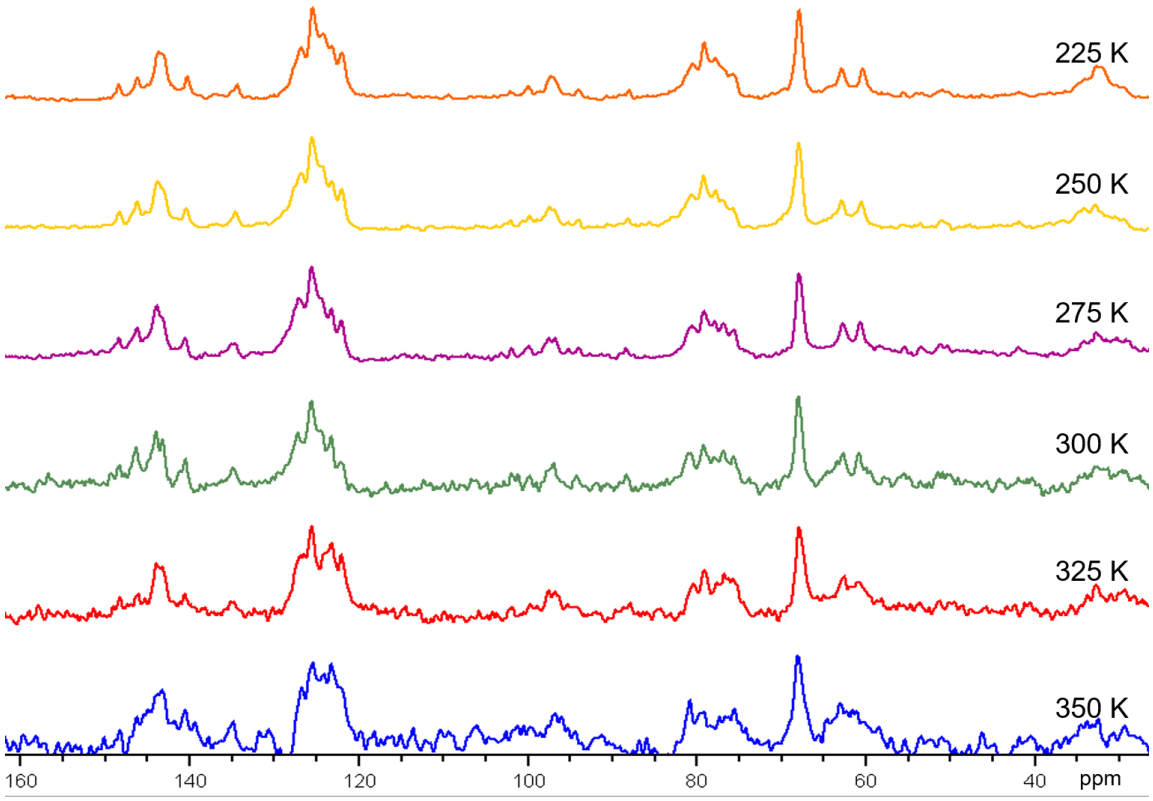

Figure 4.5: Variable-temperature ^{1}H-^{13}C CPMAS spectra of **0**, contact time= 4 ms, spin rate= 7000 Hz

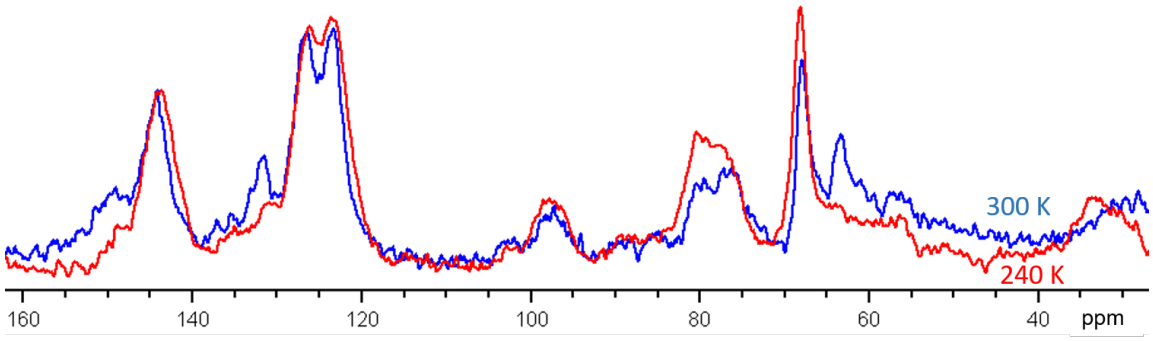

Figure 4.6: Variable-temperature ^{1}H-^{13}C CPMAS spectra of **1**, contact time= 4 ms, spin rate= 7000 Hz

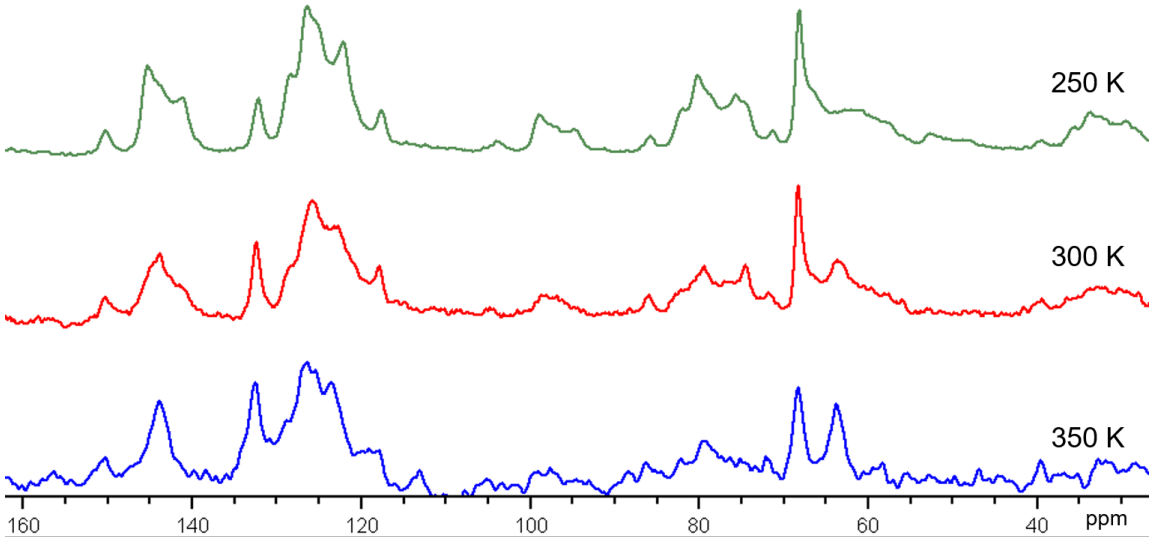

Figure 4.7: Variable-temperature ^{1}H-^{13}C CPMAS spectra of **2**, contact time= 4 ms, spin rate= 7000 Hz

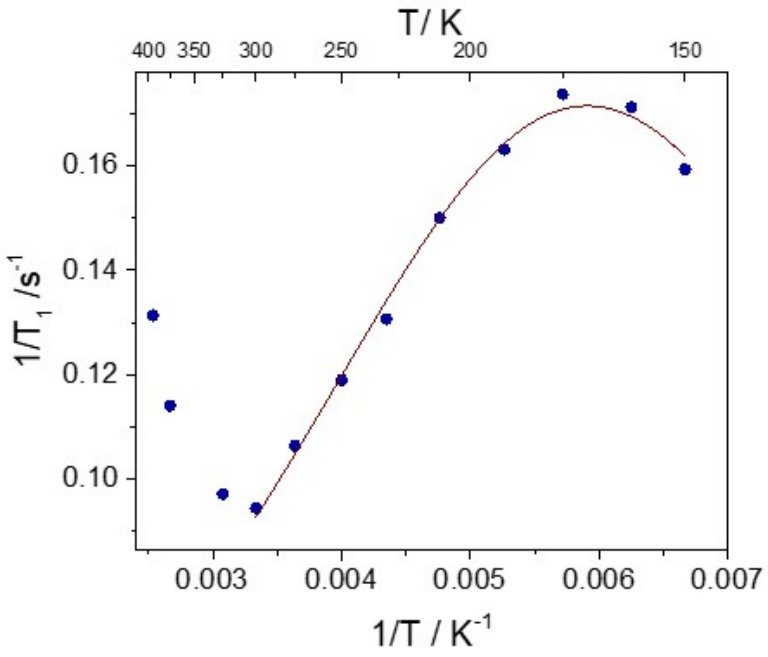

Figure 4.8: Kubo-Tomita fitting of **1**

4.3.4 Single Molecular DFT Simulation of Rotational Barrier of Rotors

Single-molecule gas-state energy barrier simulation is also conducted on compound **1** by DFT simulation. The initial structure is based on single crystal X-ray diffraction. And the energy profile is obtained by adjusting the dihedral angel between two central phenylene rings from 0 to 180 degrees. The resulting intrinsic energy barrier is 0.8 kcal/mol (Figure 4.9). The energy profile shows three local maximum when Ar-H and tertiary C-H has minimum distance(1.92 Å)(Figure 4.10). This indicates the interaction between rotor Ar-H and stator tertiary C-H contributes to the energy barrier. The result suggest that the intrinsic rotational barrier for such biphenylacetylene rotor remains low despite intramolecular stator-rotor interaction. The dipolar coupling between them may also contribute to the narrowing proton lineshape: as temperature rises, activated motion no longer experiences H-H dipolar coupling and the linewidth reduces.

Intermolecular interactions should also contribute significantly to the actual energy barrier, especially in close-packed molecular crystals.[5] Starting from the crystal structure, an ideal model includes 6 molecules and 2 fragments surrounding a target molecule. However, such calculation would be beyond our computing capabilities.

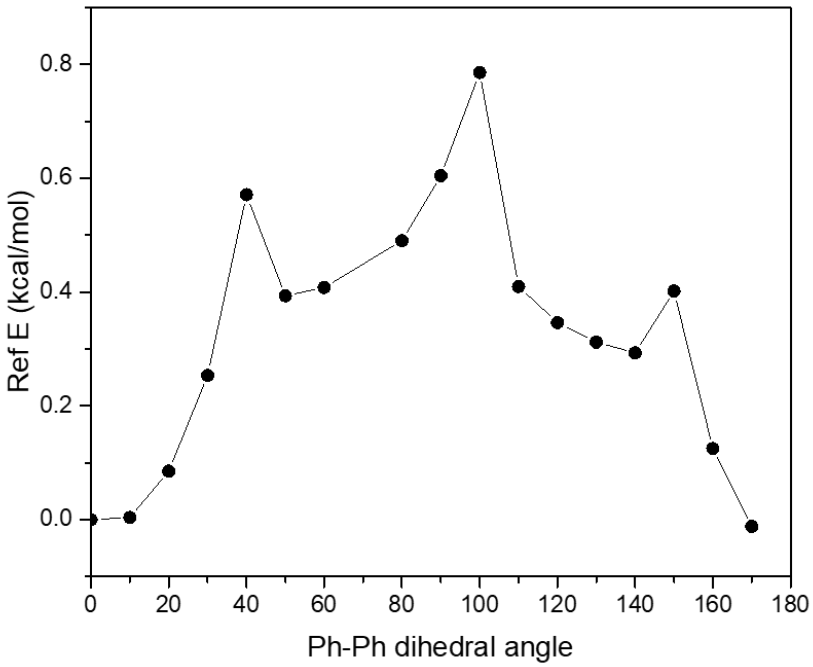

Figure 4.9: Single-molecule gas-state energy profile of **1**. method:ωB97X-D, optimization basis set: 6-31G, calculation basis set: 6-311+G**

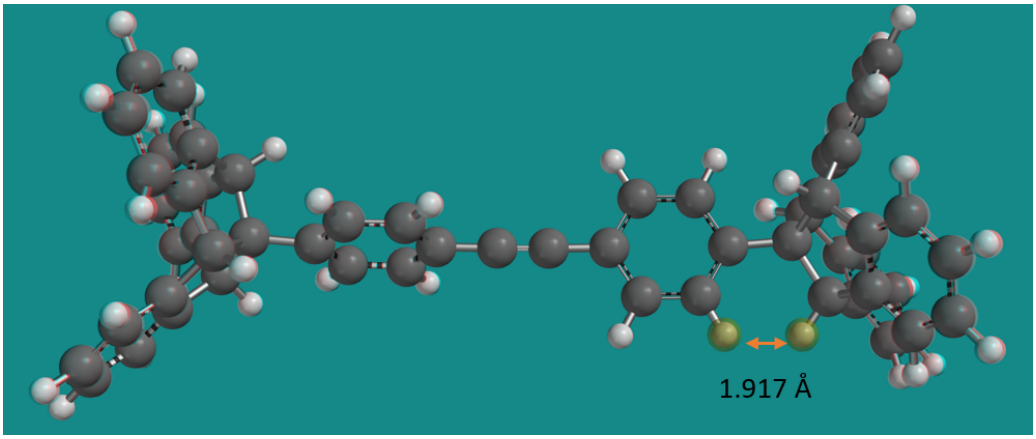

Figure 4.10: Configuration at energy maximum

4.4 Experimental Section

4.4.1 Solution NMR

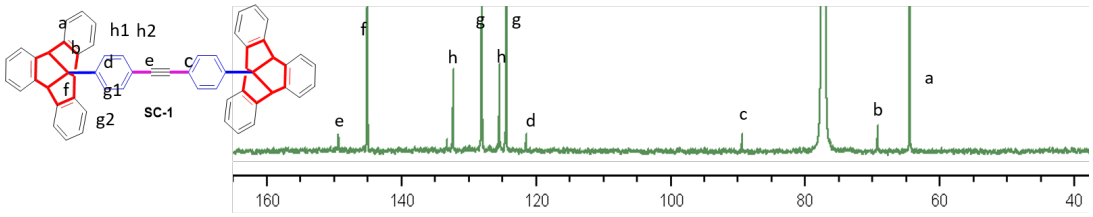

Figure 4.11: ^{1}H NMR(500 MHz, $CDCl_3$ of **1** with peak assignment)

4.4.2 Differential Scanning Calorimetry Data

Differential Scanning Calorimetry(DSC) data of **0** and **1** are shown below. The scans were completed in a RT-low-high-RT cycle. Within the temperature range, no phase change was observed. (The negative peak in Figure 4.12 left is due to unstable heat flow at the beginning of the experiment)

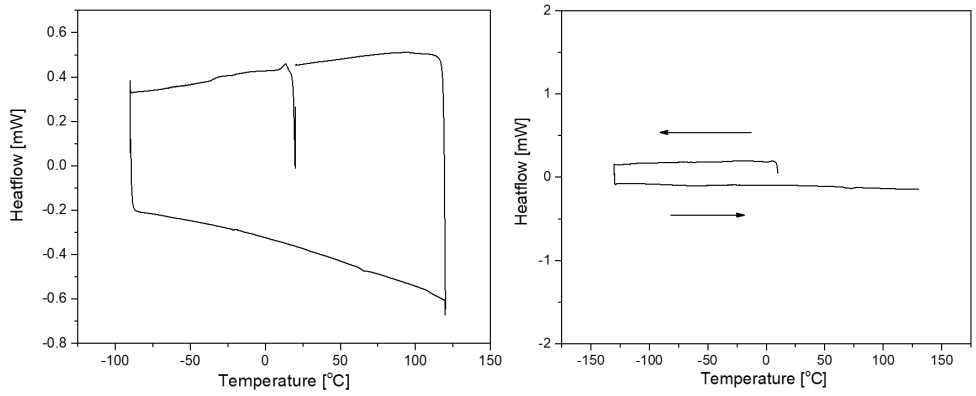

Figure 4.12: DSC curve of **0**(left) and **1**(right)

4.4.3 ^{1}H Spin-Lattice Relaxation Fitting

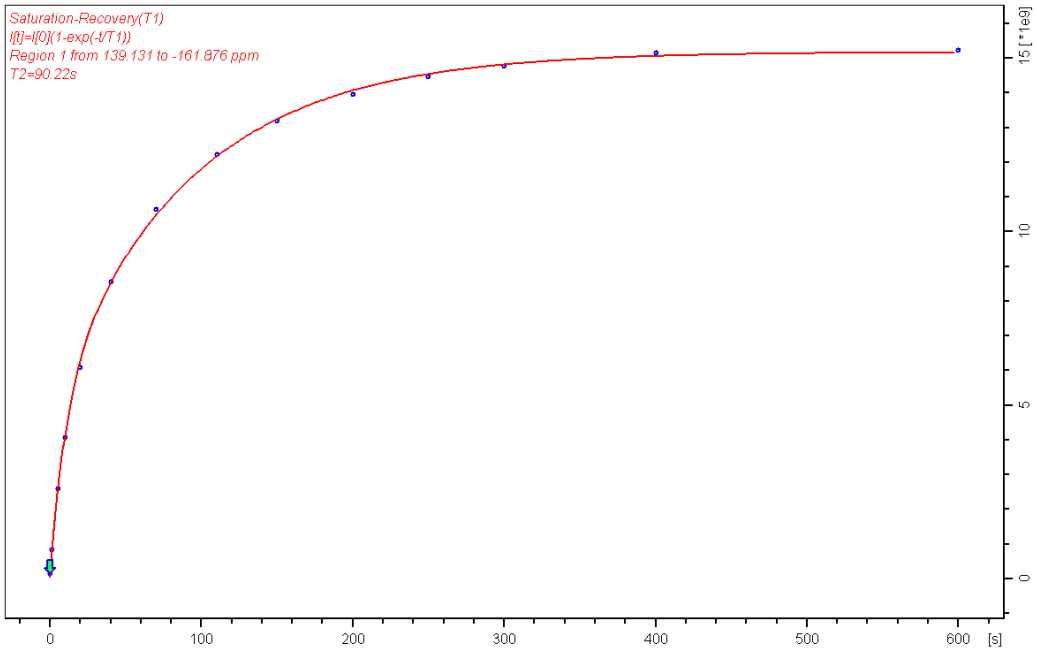

Figure 4.13: ^{1}H spin-lattice relaxation of rotor **0** at 200 K.

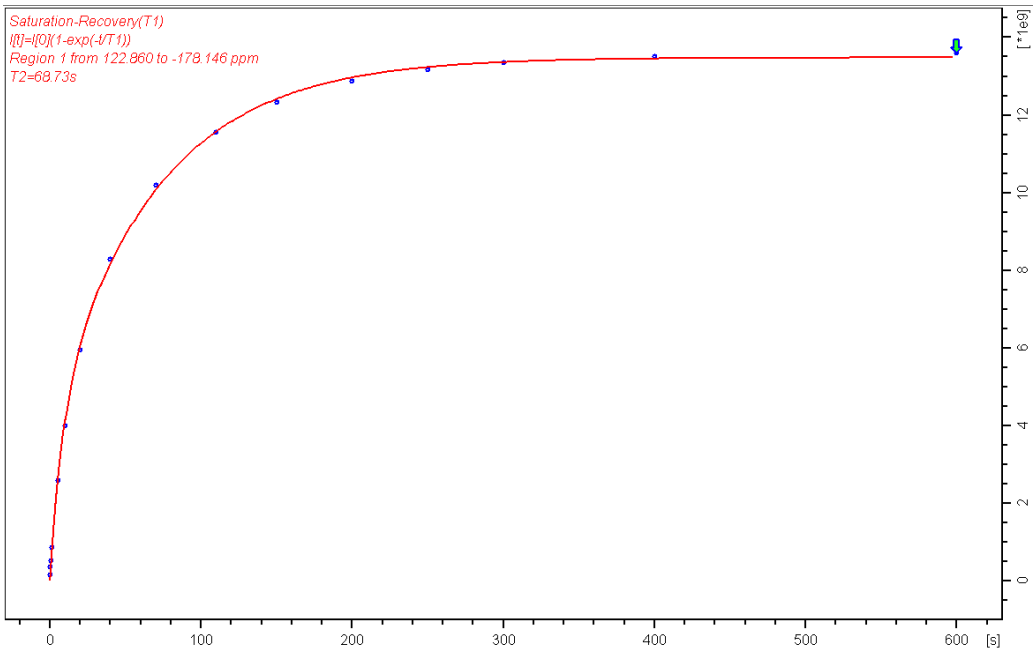

Figure 4.14: ^{1}H spin-lattice relaxation of rotor **0** at 225 K.

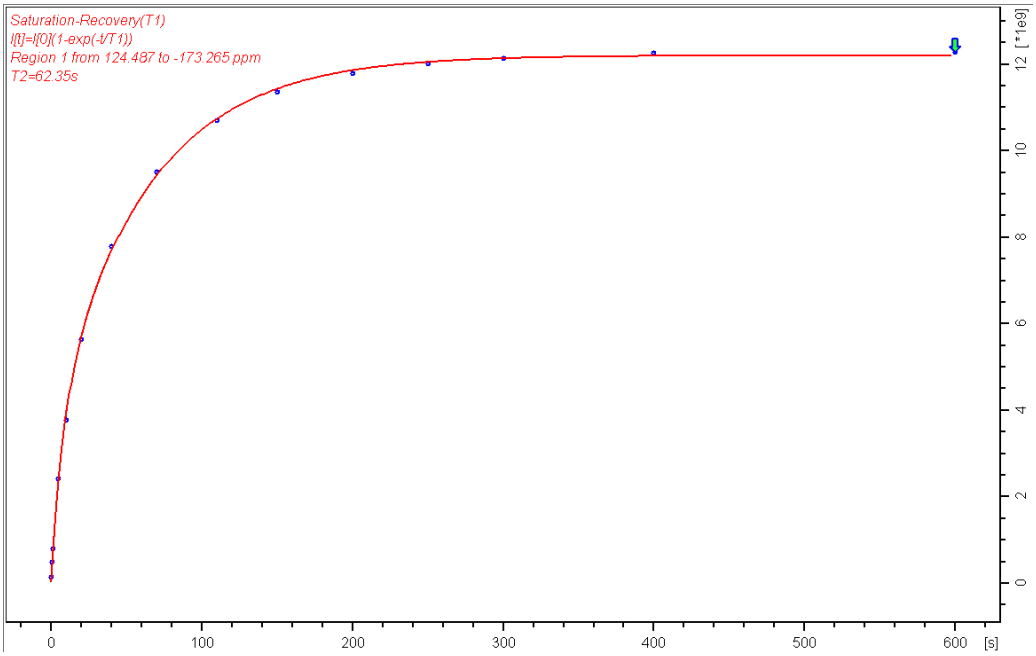

Figure 4.15: ^{1}H spin-lattice relaxation of rotor **0** at 250 K.

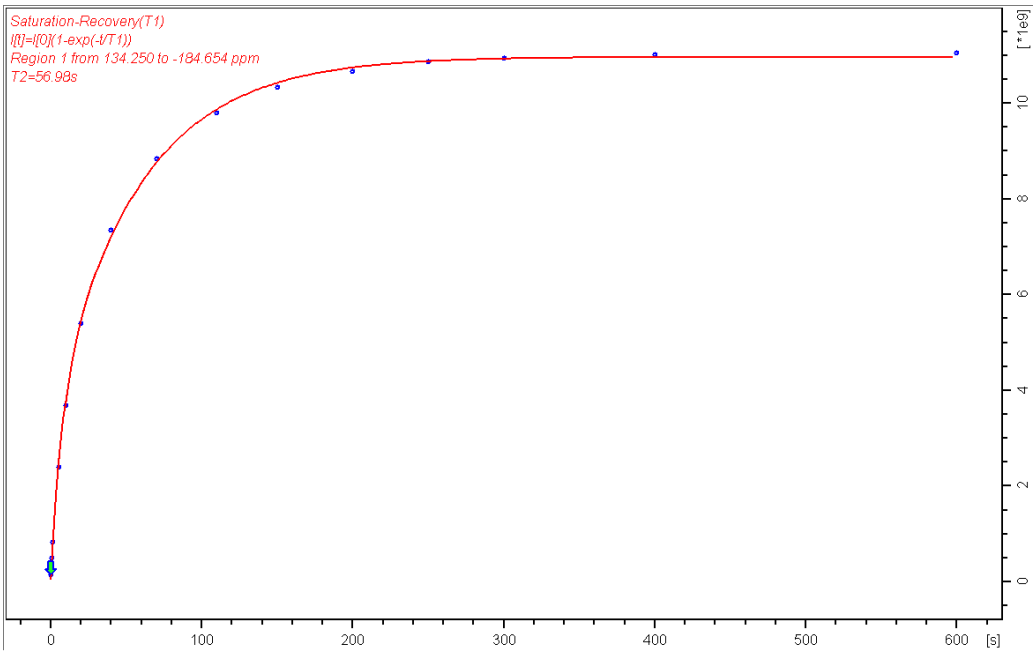

Figure 4.16: ^{1}H spin-lattice relaxation of rotor **0** at 280 K.

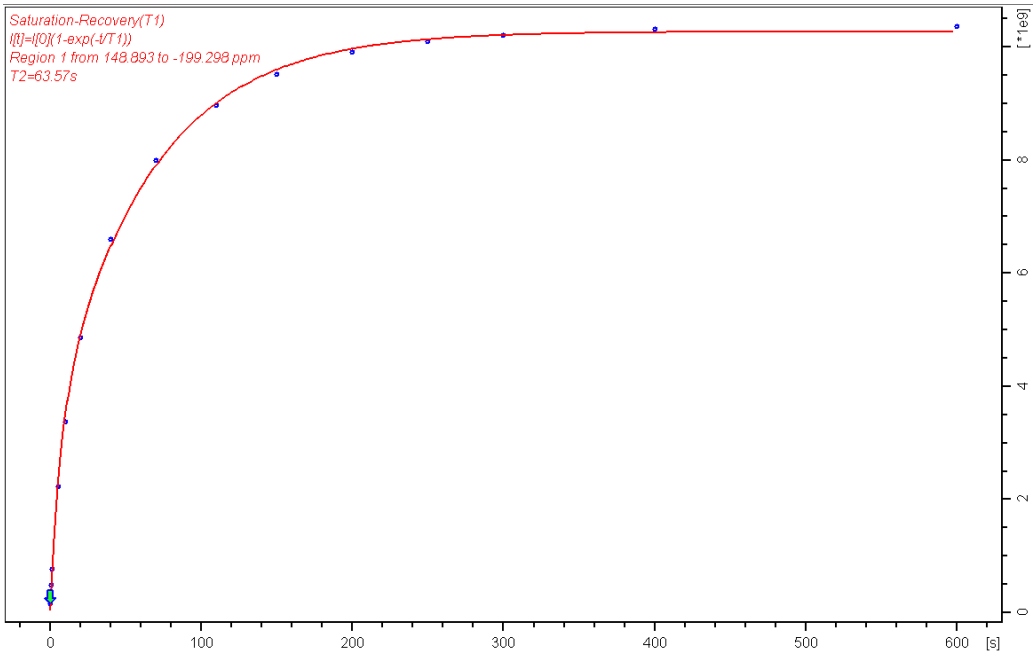

Figure 4.17: ^{1}H spin-lattice relaxation of rotor **0** at 300 K.

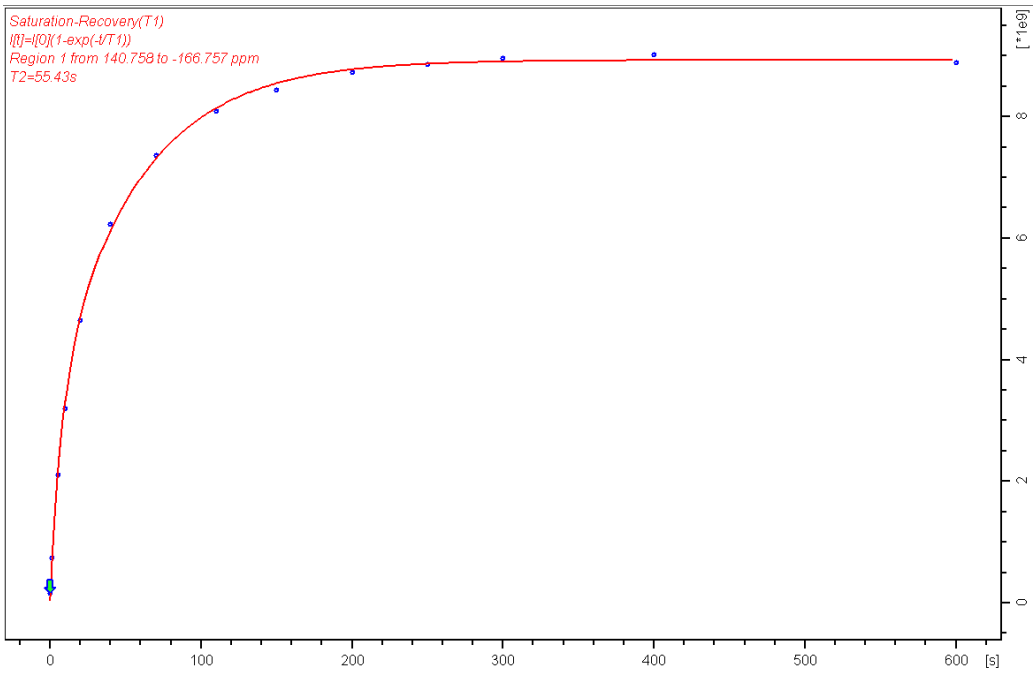

Figure 4.18: ^{1}H spin-lattice relaxation of rotor **0** at 330 K.

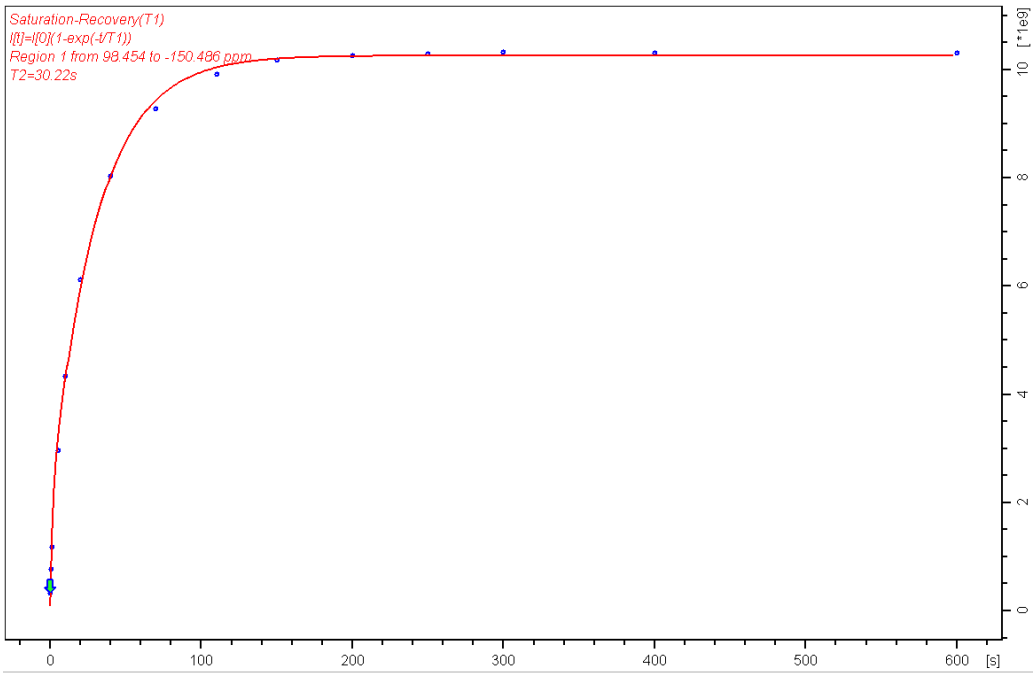

Figure 4.19: ^{1}H spin-lattice relaxation of rotor **0** at 360 K.

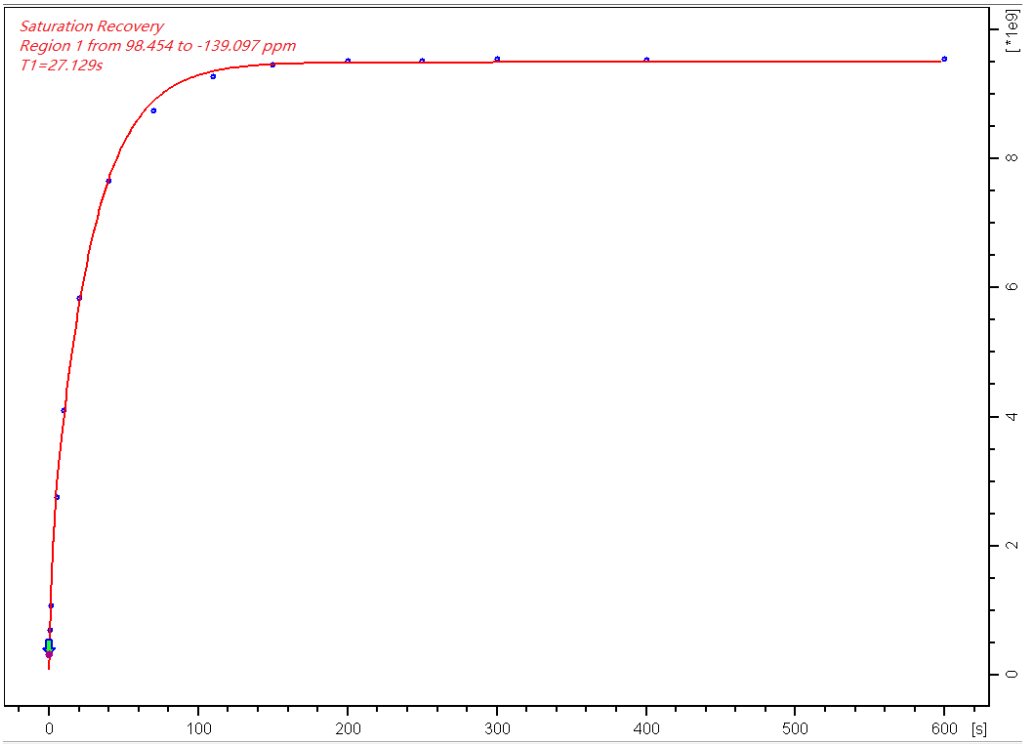

Figure 4.20: ^{1}H spin-lattice relaxation of rotor **0** at 390 K.

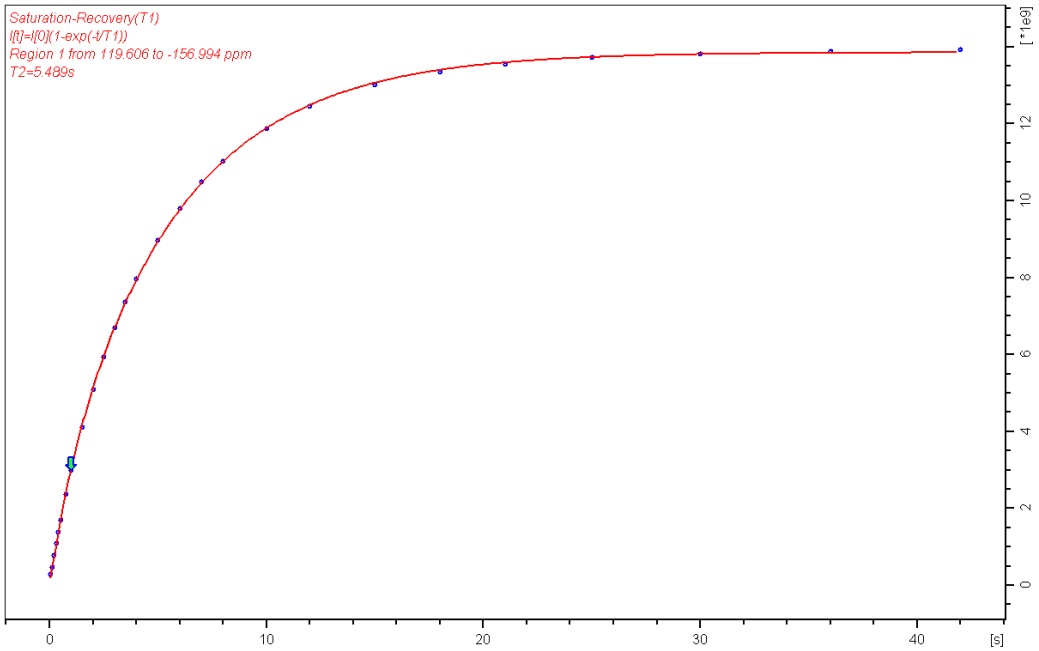

Figure 4.21: ^{1}H spin-lattice relaxation of rotor **1** at 175 K.

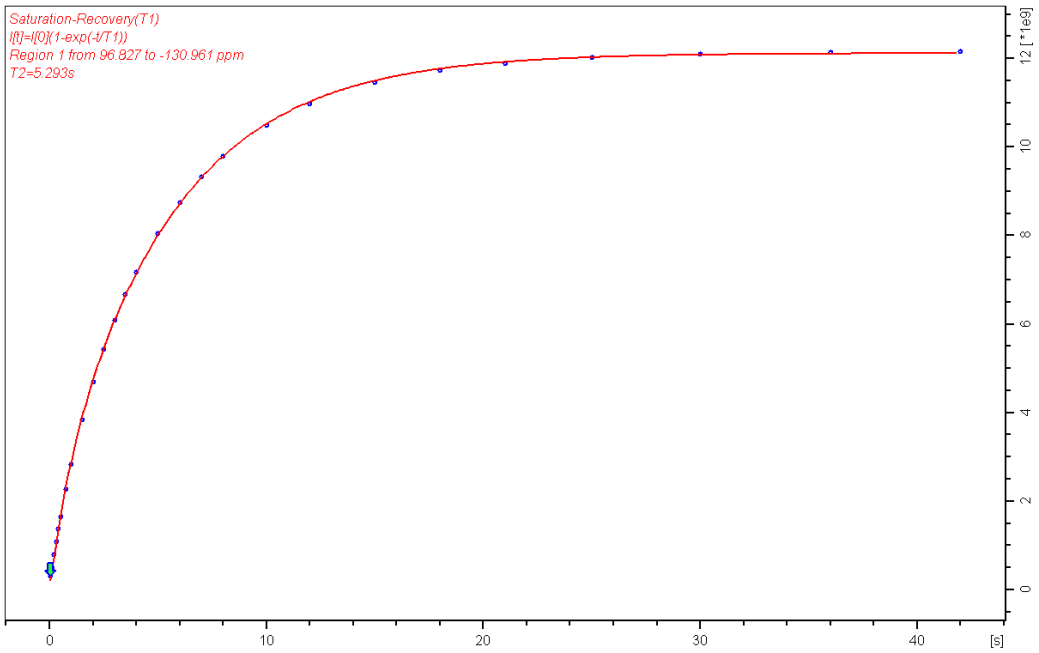

Figure 4.22: ^{1}H spin-lattice relaxation of rotor **1** at 200 K.

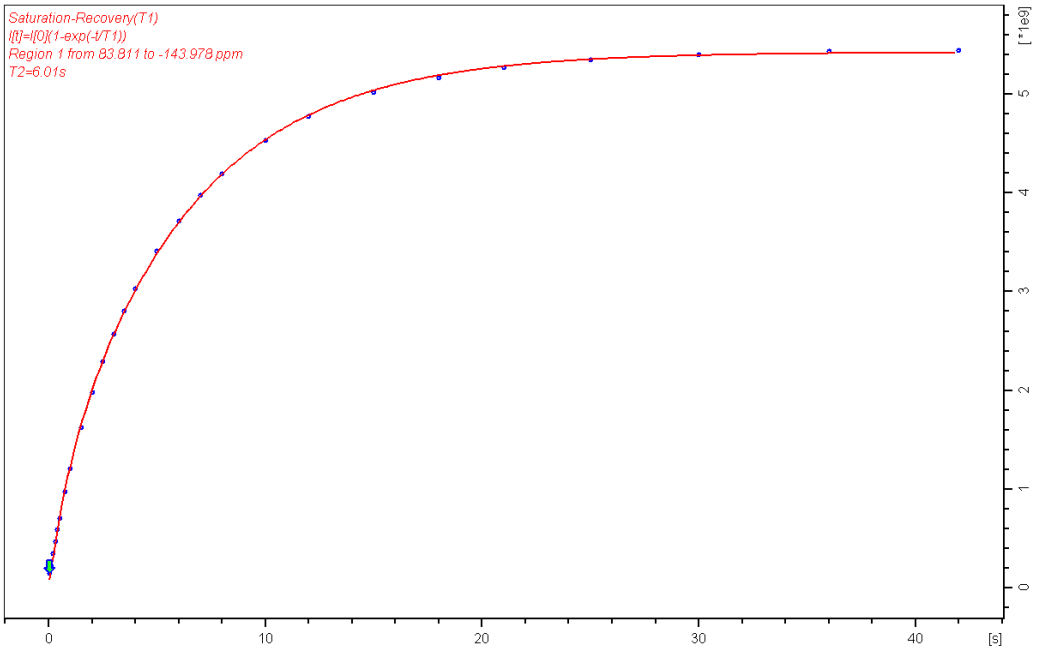

Figure 4.23: ^{1}H spin-lattice relaxation of rotor **1** at 225 K.

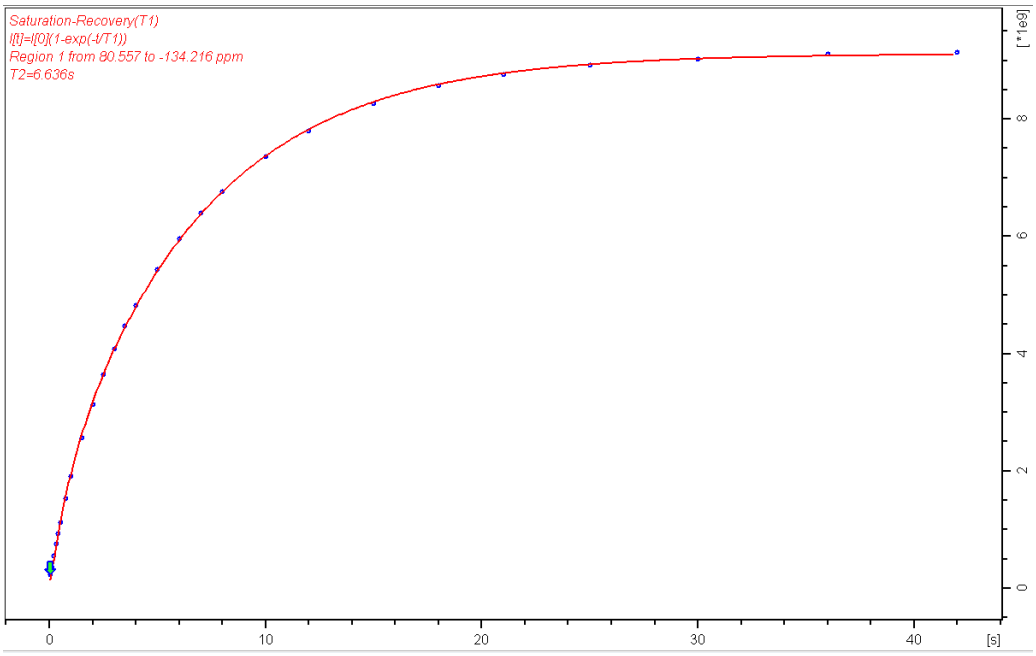

Figure 4.24: ^{1}H spin-lattice relaxation of rotor **1** at 250 K.

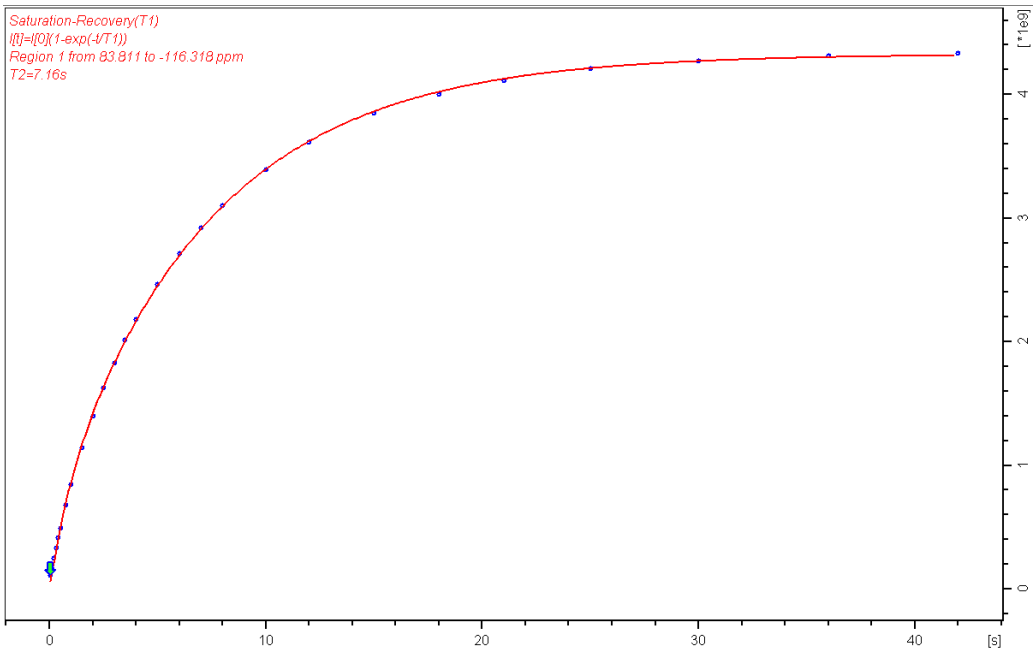

Figure 4.25: ^{1}H spin-lattice relaxation of rotor **1** at 275 K.

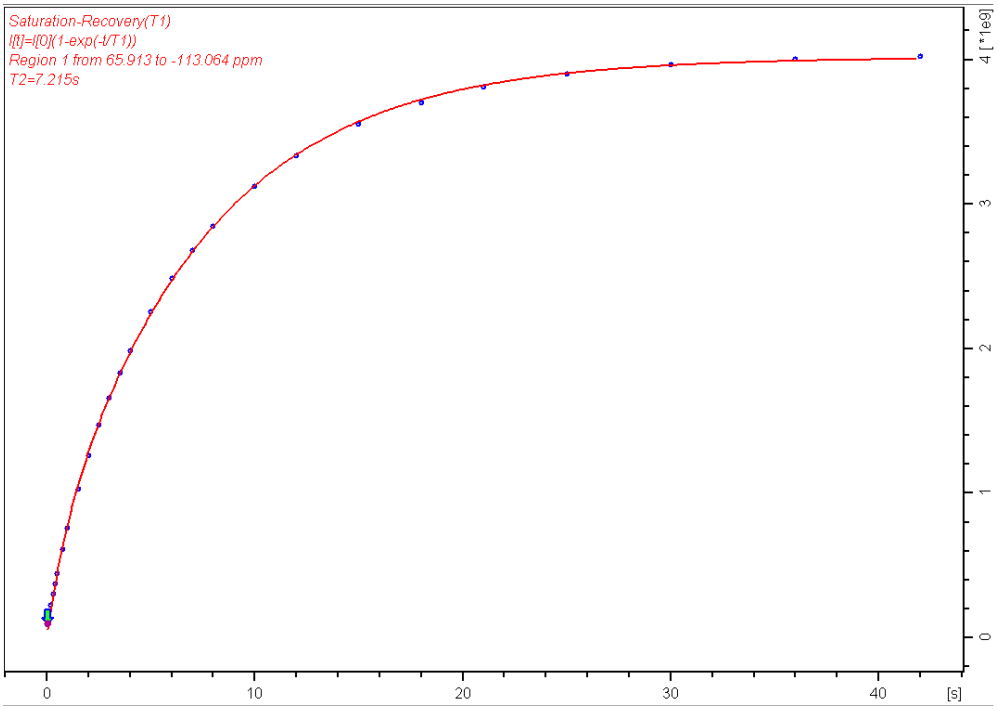

Figure 4.26: ^{1}H spin-lattice relaxation of rotor **1** at 300 K.

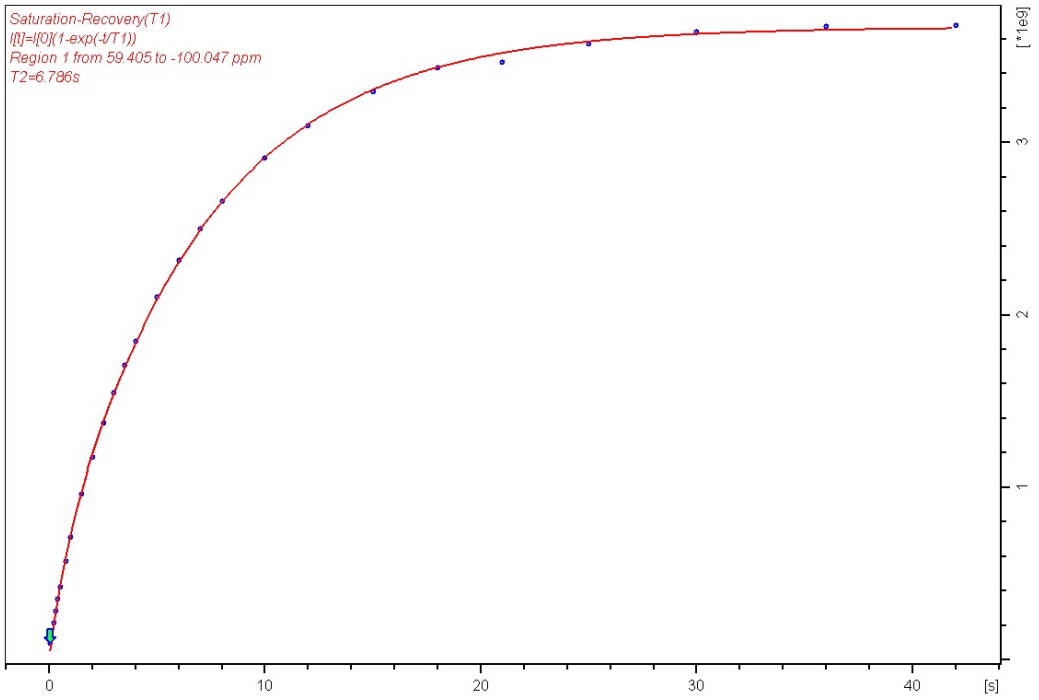

Figure 4.27: ^{1}H spin-lattice relaxation of rotor **1** at 325 K.

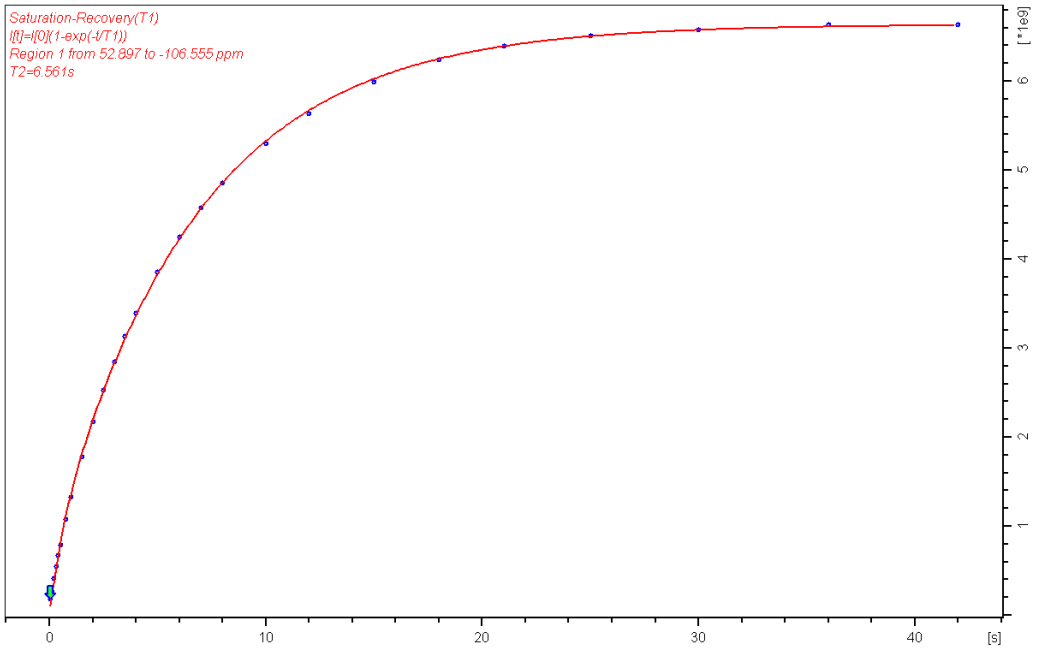

Figure 4.28: ^{1}H spin-lattice relaxation of rotor **1** at 350 K.

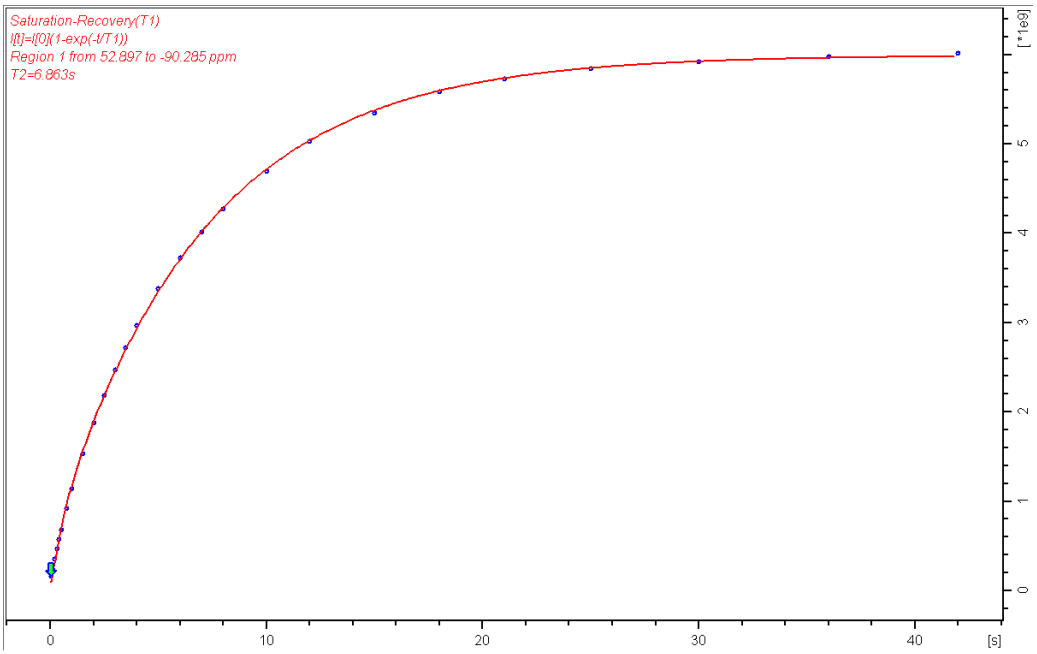

Figure 4.29: ^{1}H spin-lattice relaxation of rotor **1** at 375 K.

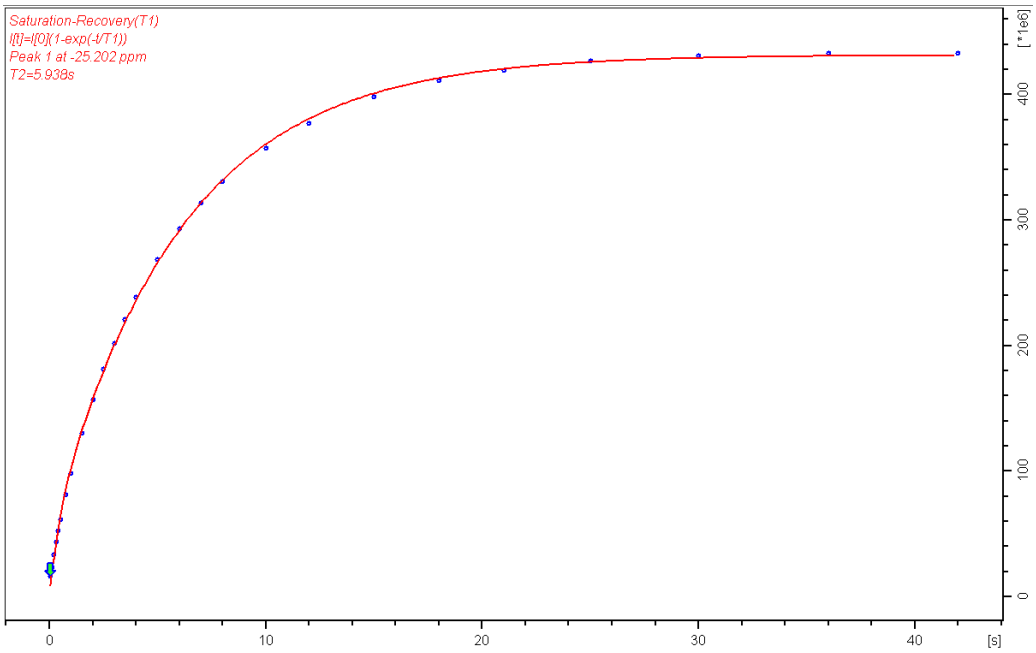

Figure 4.30: ^{1}H spin-lattice relaxation of rotor **1** at 395 K.

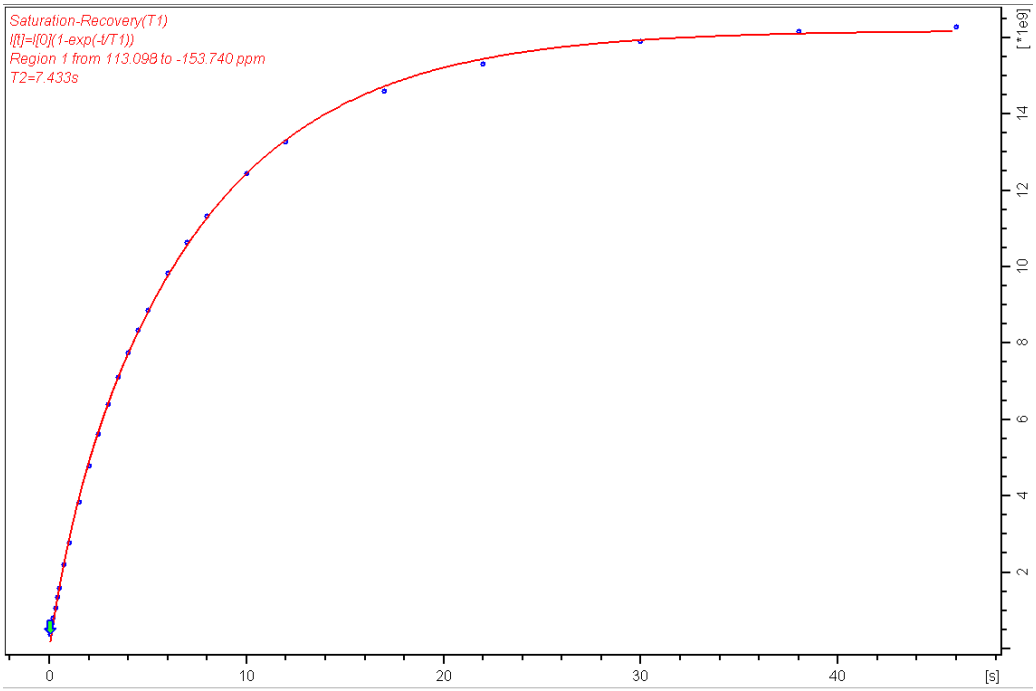

Figure 4.31: ^{1}H spin-lattice relaxation of rotor **2** at 175 K.

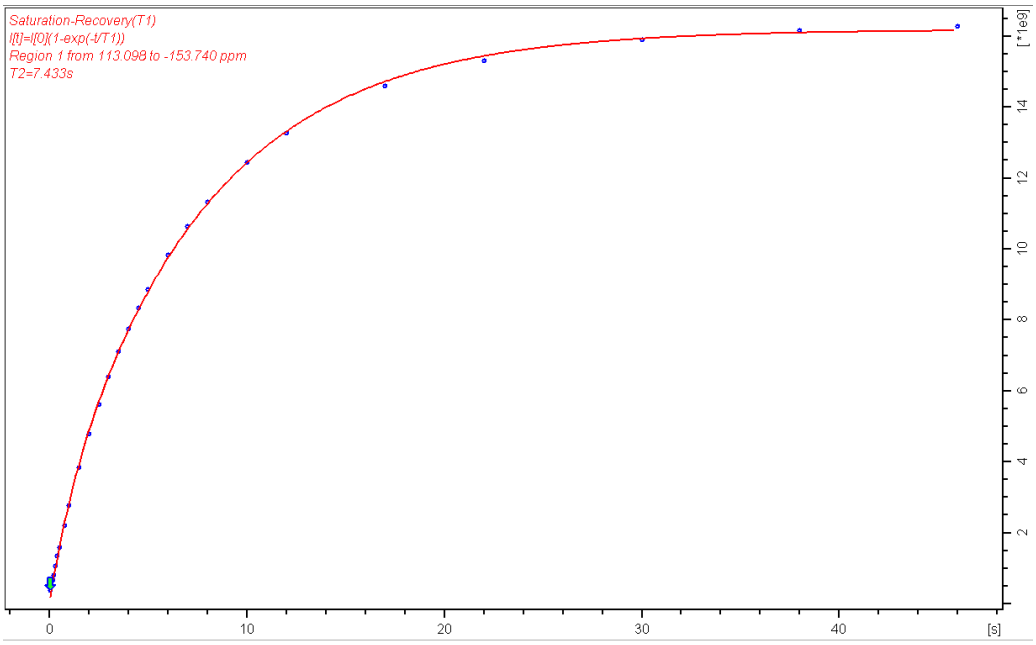

Figure 4.32: ^{1}H spin-lattice relaxation of rotor **2** at 200 K.

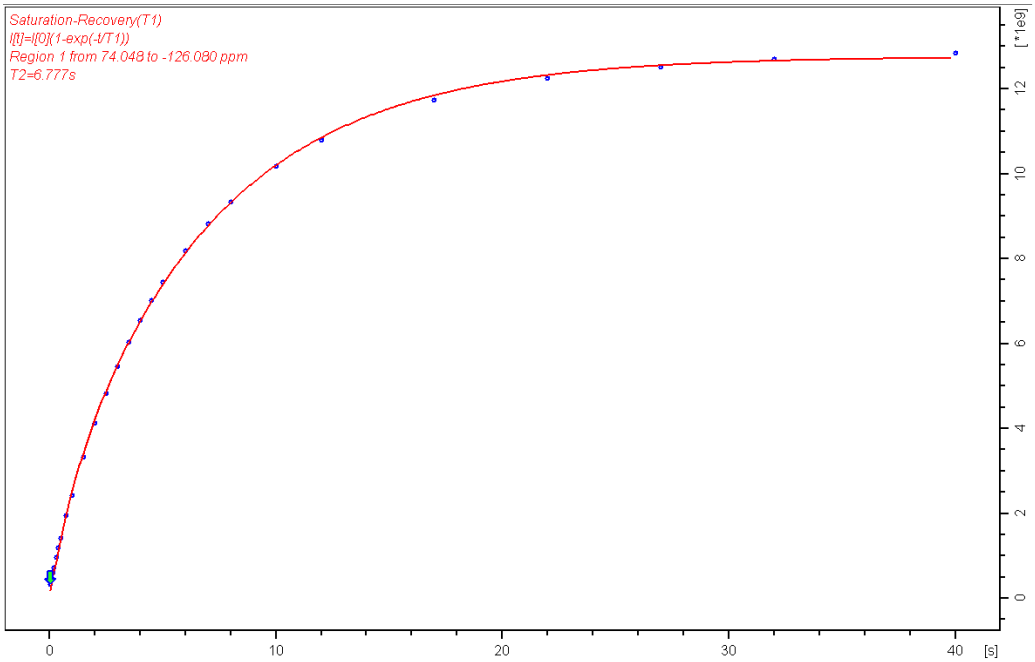

Figure 4.33: ^{1}H spin-lattice relaxation of rotor **2** at 225 K.

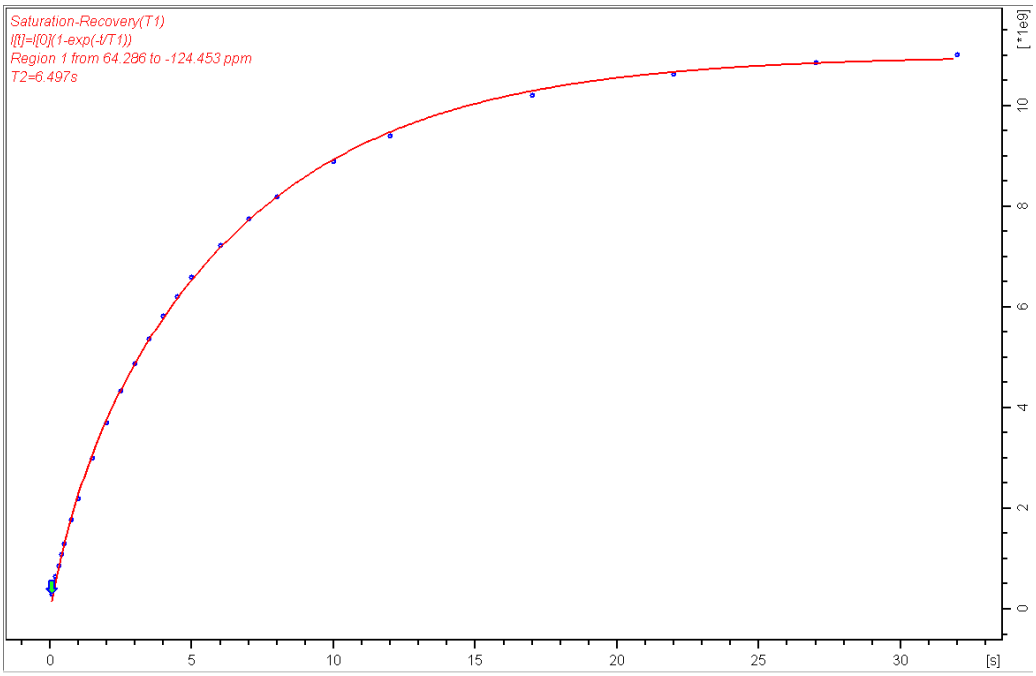

Figure 4.34: ^{1}H spin-lattice relaxation of rotor **2** at 250 K.

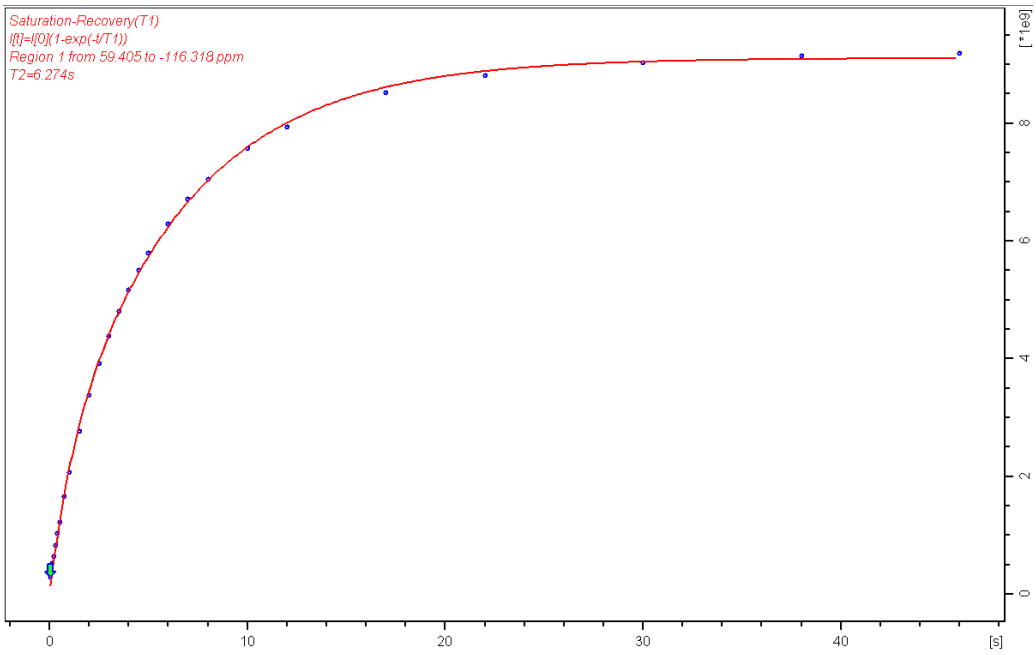

Figure 4.35: ^{1}H spin-lattice relaxation of rotor **2** at 300 K.

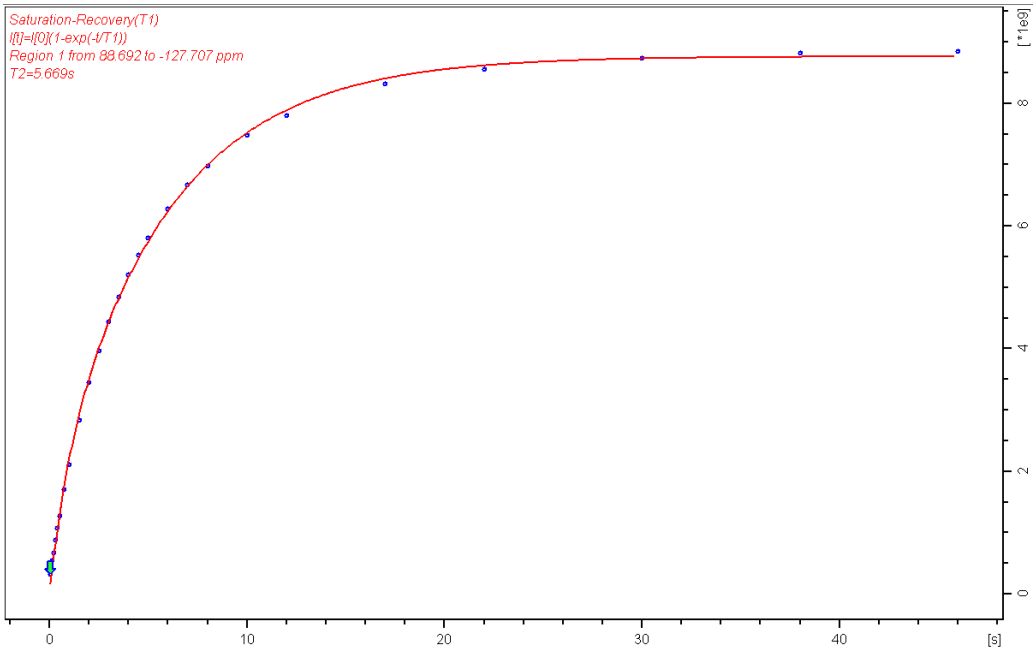

Figure 4.36: ^{1}H spin-lattice relaxation of rotor **2** at 325 K.

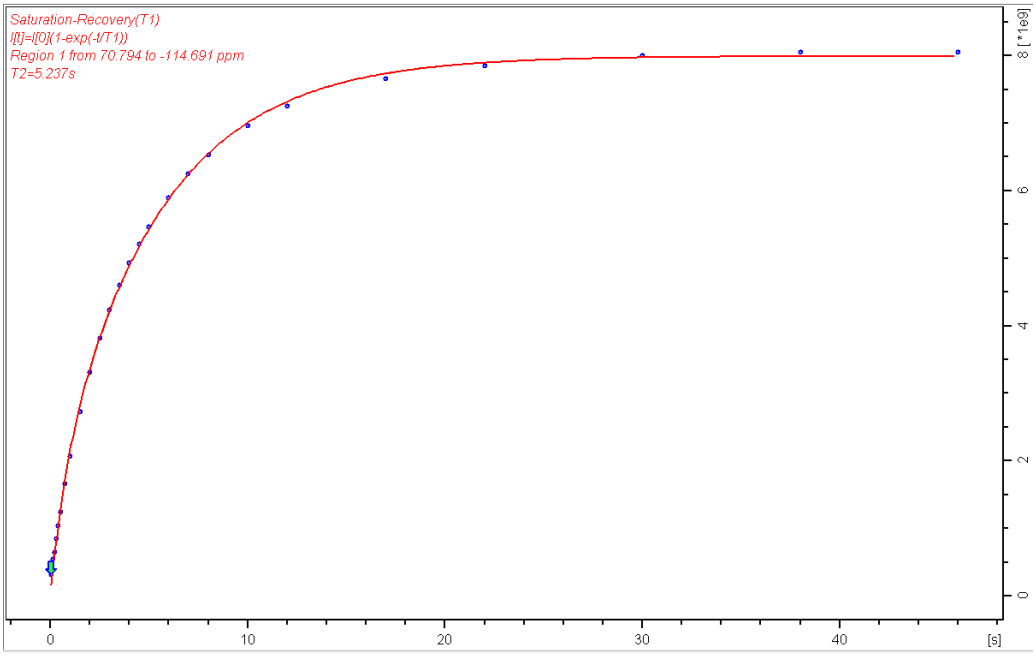

Figure 4.37: ^{1}H spin-lattice relaxation of rotor **2** at 350 K.

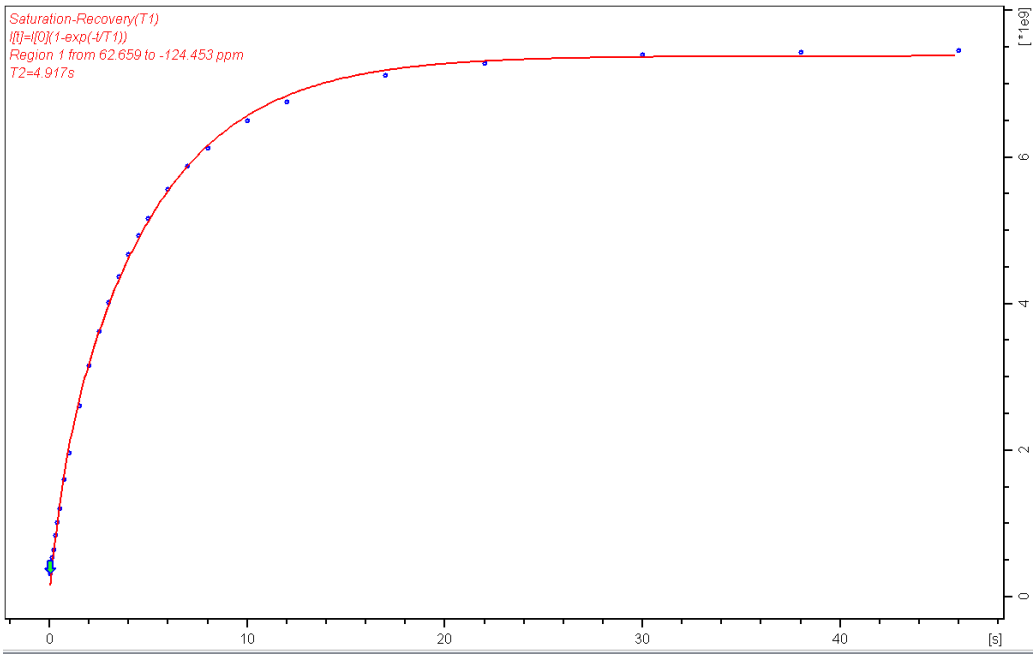

Figure 4.38: ^{1}H spin-lattice relaxation of rotor **2** at 375 K.

4.4.4 Crystal Structures

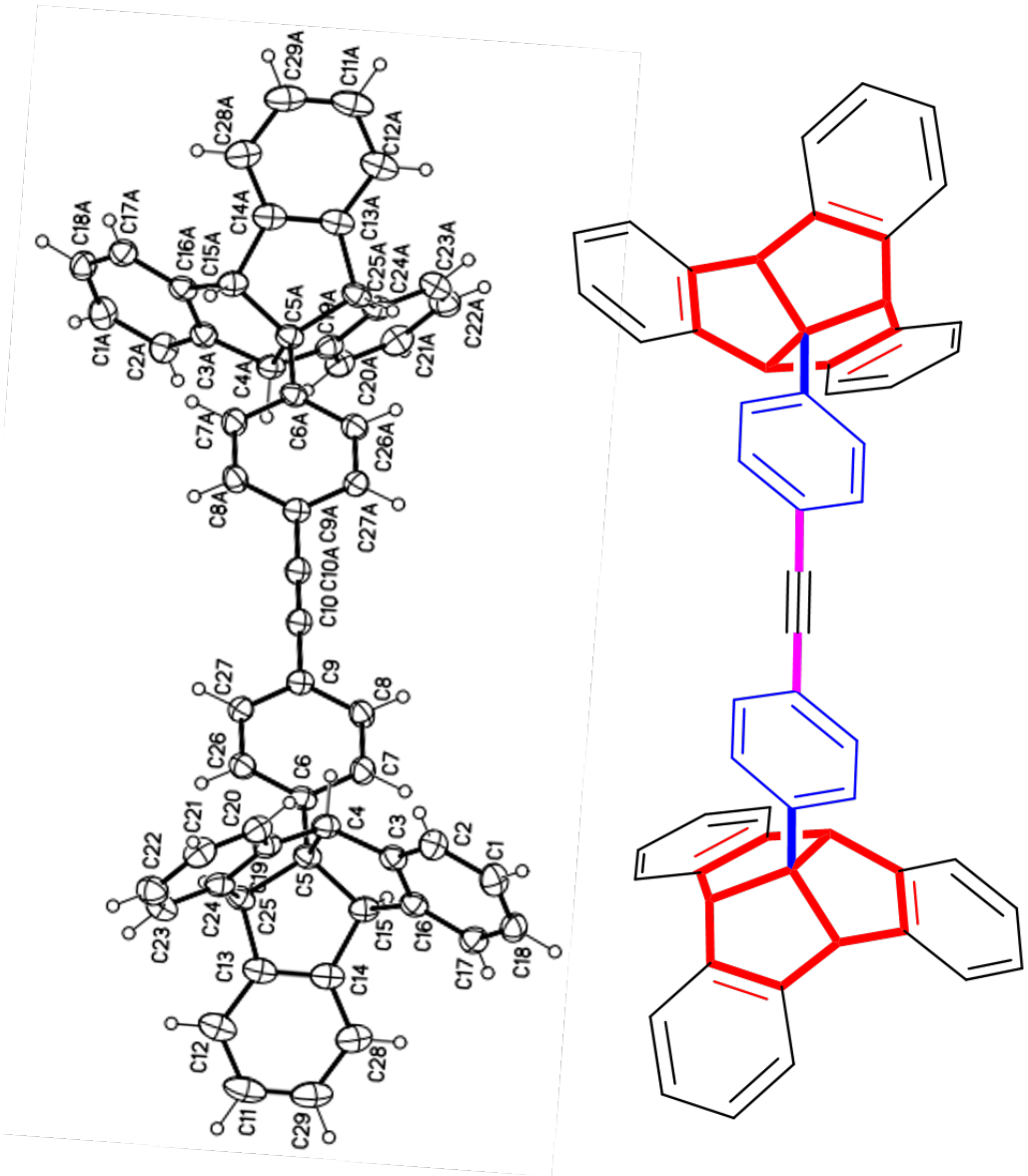

Figure 4.39: Crystal and structure of **1**

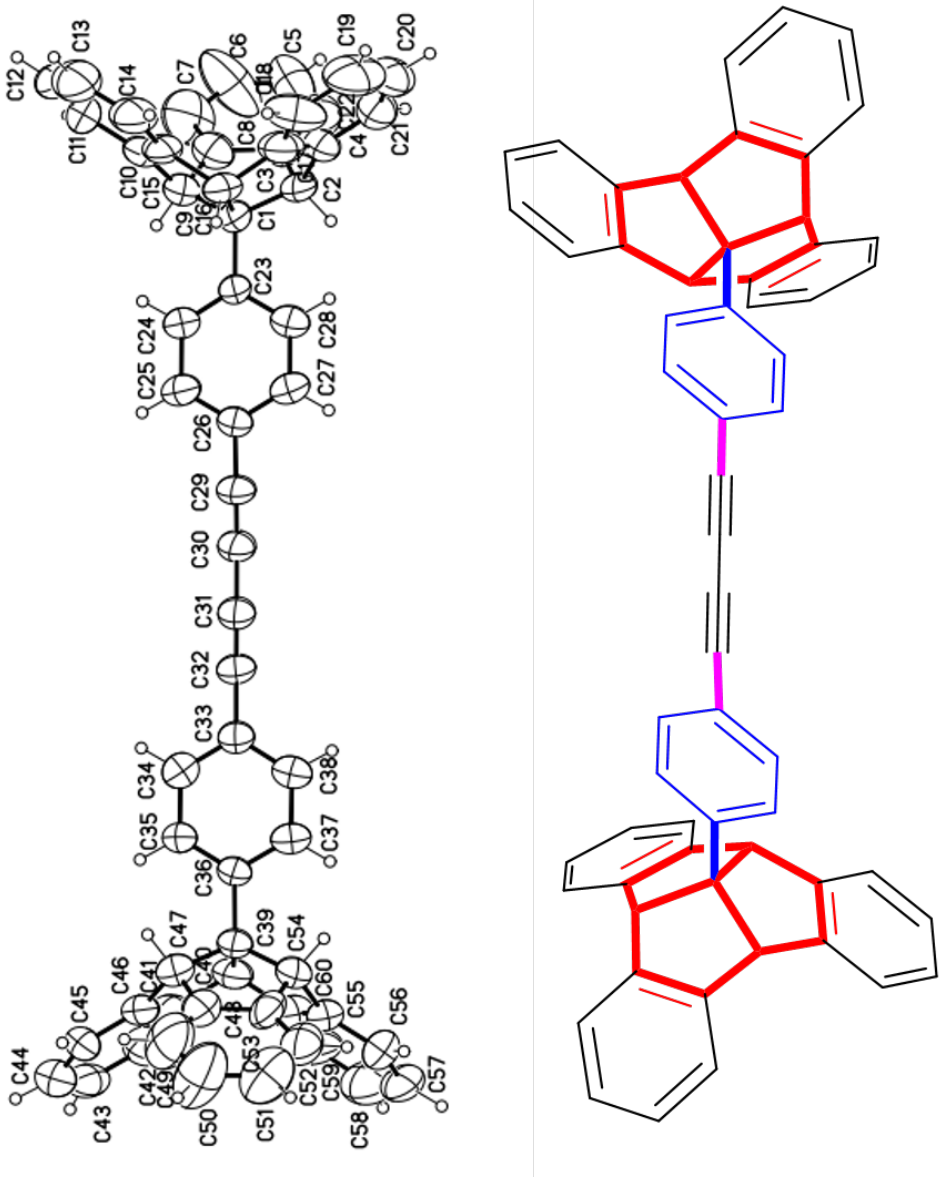

Figure 4.40: Crystal and structure of **2**

Table 4.1: Crystallographic data of compound **1** and **2** acquired with Bruker APEX-II CCD Mo K_α beam. Refined with SHELXL 2014/6.

Compound	**1**	**2**
Temperature/K	100	100
Crystal System	Monoclinic	Monoclinic
Space Group	$P2_1/c$	$P2_1/c$
a/Å	9.5673	20.4290
b/Å	13.7765	13.6848
c/Å	15.493	16.0606
α/Å	90	90
$\beta/^\circ$	104.518	90
γ/Å	90	90
V/Å^3	1976.8	4490.0
Z	4	4
Reflections used	4055	9184
R factor	4.33%	11.45%

References

[1] M. E. Howe and M. A. Garcia-Garibay, "The roles of intrinsic barriers and crystal fluidity in determining the dynamics of crystalline molecular rotors and molecular machines," *The Journal of Organic Chemistry*, vol. 84, no. 16, pp. 9835–9849, 2019.

[2] B. Bredenkötter, M. Grzywa, M. Alaghemandi, *et al.*, "Tribenzotriquinacene receptors for c60 fullerene rotors: Towards c3 symmetrical chiral stators for unidirectionally operating nanoratchets," *Chemistry–A European Journal*, vol. 20, no. 29, pp. 9100–9110, 2014.

[3] G. Markopoulos, L. Henneicke, J. Shen, Y. Okamoto, P. G. Jones, and H. Hopf, "Tribenzotriquinacene: A versatile synthesis and c3-chiral platforms," *Angewandte Chemie International Edition*, vol. 51, no. 51, pp. 12 884–12 887, 2012.

[4] R. Kubo and K. Tomita, "A general theory of magnetic resonance absorption," *Journal of the Physical Society of Japan*, vol. 9, no. 6, pp. 888–919, 1954.

[5] P. D. Jarowski, K. Houk, and M. A. Garcia-Garibay, "Importance of correlated motions on the low barrier rotational potentials of crystalline molecular gyroscopes," *Journal of the American Chemical Society*, vol. 129, no. 11, pp. 3110–3117, 2007.

CHAPTER 5

Explorations on Trigonal Arrangement of Dipoles in Metal-Organic Frameworks

Unpublished work.Synthesis of PEP-2F ligand is conducted by Dr. Erik Leonhardt.

5.1 Introduction

As discussed in previous chapters, ferroelectricity arises from spontaneous polarization and polar point group. Efforts documented before this chapter aim at achieving spontaneous dipolar alignment and understanding rotations of dipoles. In order to give free space to rotors, linear bisethynylphenylene MOF ligands usually yield MOFs with high symmetry such as cubic or tetragonal phase, which means the polarizable material will not be ferroelectric due to the requirement of symmetry. By varying the geometry of organic linker molecules and metal cluster, non-tetragonal MOFs are anticipated. Kagome lattice is one interested template. It has P6 symmetry and trihexagonal tiling. MOFs with 2D Kagome layer has been observed before.[1]–[3] For our study, such arrangement is specially interesting when dipoles are installed in

the edges because they can either lead to a out-of-plane frustrated dipole arrangement or in-plane polarization, depending on orientations of rotors principle axle. Additionally, Kagome lattice can avoid interpenetration in pillar-layered structure. In this chapter, conditions to synthesize Kagome lattice in several MOFs systems are explored and documented.

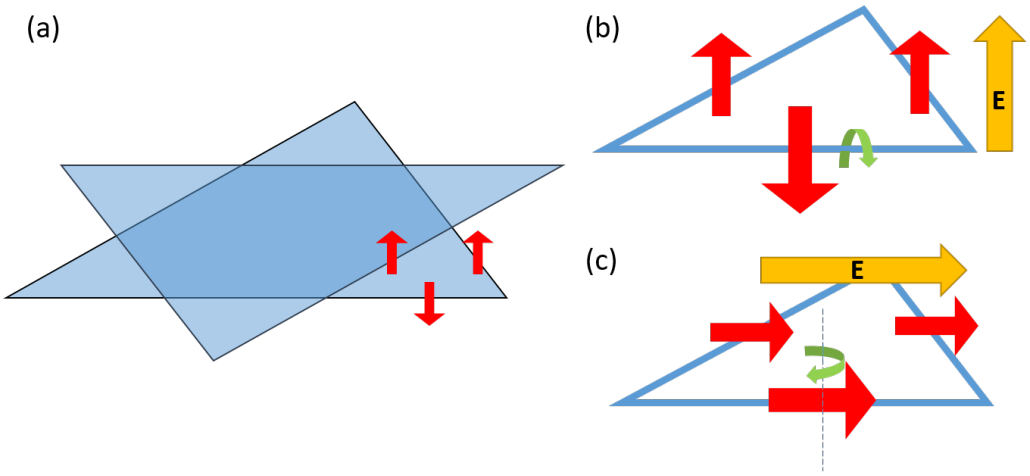

Figure 5.1: 2D Kagome arrangement of hexagonal and trigonal channels(a) and dipole alignment in **kgm**(b) and **csq**(c) topology. Red arrow represents electric dipole, E is eletric field.

5.2 Zinc Pillar layered MOFs with Functionalized BDC and DABCO

As described in Chapter 2, zinc paddle wheel unit can coordinate with both oxygen and nitrogen atoms from diffrent ligands. Therefore, $Zn_2(BDC_2)(DABCO)$ MOF crystals can be synthesized from zinc nitrate, benzoicdicarobxylic acid(BDC) and

1,4-diazabicyclo[2.2.2]octane(DABCO). In fact such MOF can adopt either tetragonal phase or Kagome phase(topology **kgm**). Several studies have reported conditions to access the kinetics-controlled Kagome phase by solvent choice or nucleation temperature control.[4], [5] When dipoles are installed into the MOF structure by functionalization of BDC, the Kagome lattice becomes more interesting due to its special arrangement. When rotary dipoles are installed in three edges of a triangle and the rotational axle are alone with the edges, electric field can induce a net polarization out of plane. However, not all three dipoles are aligned along the direction of electric field because strong dipole-dipole repulsion may prevent such alignment. Fuctionalized BDC in Zn Kagome lattice was never reported before and trials on dimethyl, ...,was documented in [4]. Herein we seek to explore conditions to access Zn Kagome lattice with chlorobenzoicdicarboxylic acid(Cl-BDC) and bromobenzoicdicarboxylic acid(Br-BDC).

In a previous investigation of our group[6], Kagome lattice appeared as impurities after solvothermal synthesis. Therefore starting with similar condition, we aimed at synthesizing Kagome lattice by changing concentrations and solvent combination. Since Zn Kagome MOF has a bigger hexagonal channel, the first PXRD peak are supposed to appear at lower angle(4.7) than tetragonal lattice (110) at 8.3 degree. However, in our initial trials, no such peak was observed and the PXRD pattern agree with tetragonal $Zn_2(BDC)_2(DABCO)$. Next, we followed a controlled-nucleation procedure to access Zn Kagome MOFs from unfuntionalized BDC [5]. 0.01M zinc nitrate, 0.01M Cl-BDC or Br-BDC and 0.005M dabco were added to 3

mL DMF and the mixture was sonicated until dissolution. Then the mixture was heated to 120°C for different periods(1 hour to 12 hours). The resulting MOFs are exclusively tetragonal phase.

The results above prove that incorporating functionalized BDC into Zn Kagome MOF is a very challenging task. In comparison with results presented in previous report, both electron withdrawing and donating functional groups have been attempted thus PK_a of BDC is not likely the deciding factor. A possible explanation is given as follows. In tetragonal phase, four Zn-O coordination bonds are evenly spaced and the angles are 90° between adjacent Zn-O bonds. In Kagome phase, a 60°-120° configuration is required for trigonal and hexagonal 1-D pore. Therefore, the BDC unit will have closer distance with another. Therefore, a functionalized BDC will lead to greater steric hindrance which is not favored in nucleation stage towards Kagome lattice.

5.3 Zinc Pillar-Layered MOFs with BDC and Pyrazine

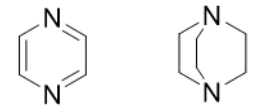

Scheme 5.1: Pyrazine and DABCO

Zn MOFs with pyrazine as pillar ligand is also explored. Similar to BDC, pyrazine has capabilities to coordinate to metal and construct MOFs.[7].Protonated pyrazine

Figure 5.2: Tetragonal $Zn_2(ClBDC)_2DABCO$ MOF in DMF

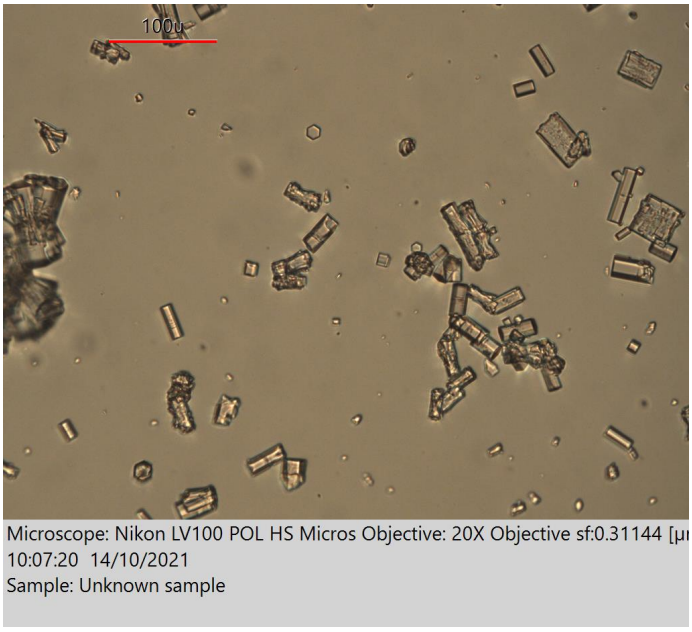

Figure 5.3: Tetragonal $Zn_2(BrBDC)_2DABCO$ MOF in DMF

has a pKa of 0.38 vs 3.0 for dabco.With different charge distribution on nitrogen, thus nucleation/growth in c dimension will be different. And we aim to enable different structure in Zn MOFs with pyrzine.

The initial trials at 120°C yields plate-shape crystals 5.4, the crystals show birefringence. Single crystal data suggests no pyrazine molecules were included. And further heating of pyrazine in DMF-d6 indicates that pyrazine is not stable in DMF after long period of heating(Figure 5.5). Intensity of peaks near 8.7 ppm significantly reduces and impurity peaks shows up. Therefore, procedures at lower temperatures are explored.

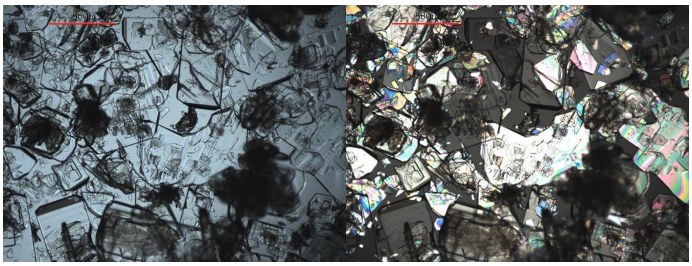

Figure 5.4: Trials with 0.1mM zinc nitrate, 0.1 mM BDC 1 mM pyrazine in DMF at 110°C for 24 hours

The most promising trial is when we lower the temperature to 80°C. Near tetragonal crystals with good diffractions are observed. However, the SCXRD indicates that the crystals only have DMF molecules as insertion between Zn-BDC layers. In other words, we are obtaining Zn-BDC-DMF complex. The polarized microscopic image at a hot stage of wet crystals confirmed such findings: birinfringence starts to fade away when temperature reaches 130°C, which is very close to DMF boiling

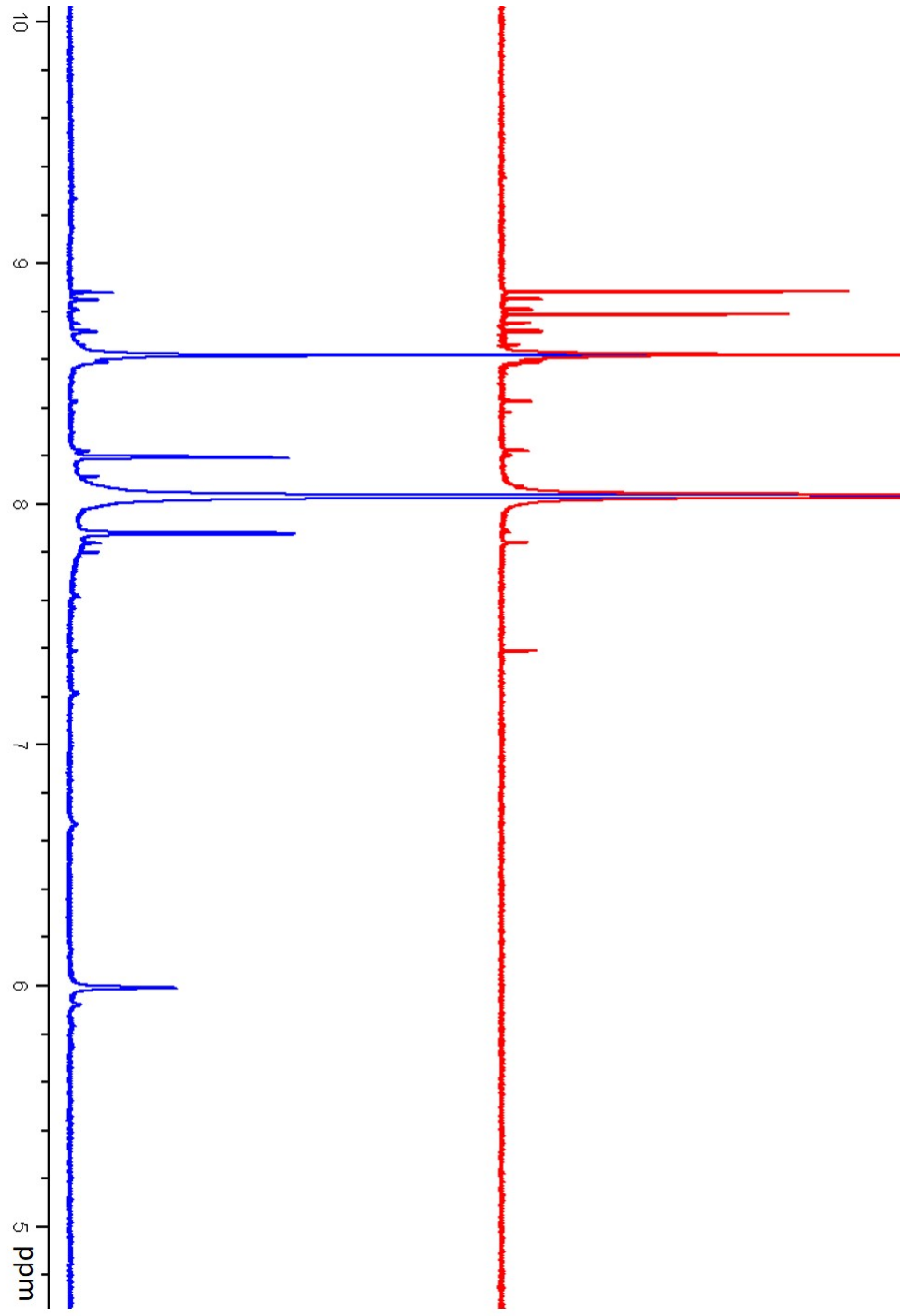

Figure 5.5: ^{1}H (NMR 500 MHz, DMF-d6) of pyrazine unheated(red) and heated at 100°C for 24 hours(blue)

point(Figure 5.6 and 5.7). DSC data indicates two endothermal peak near 130°C, which are corresponding to free DMF and trapped DMF crystals(Figure 5.8). And when DMF escapes from the crystals, the structure collapses and crystllinity is lost.

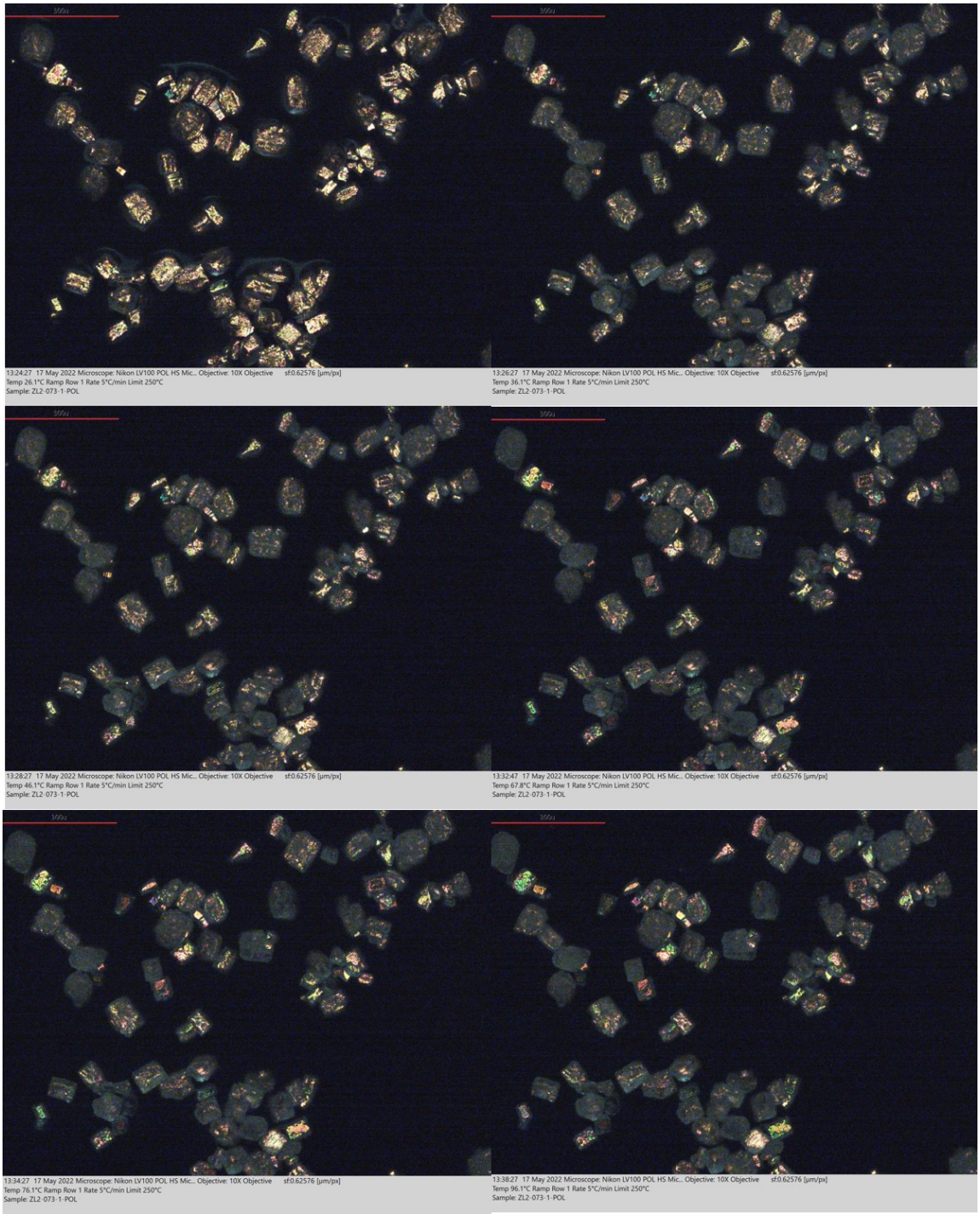

Figure 5.6: Polarized variable-temperature microscopic image of Zn-BDC-Pyrazine trial

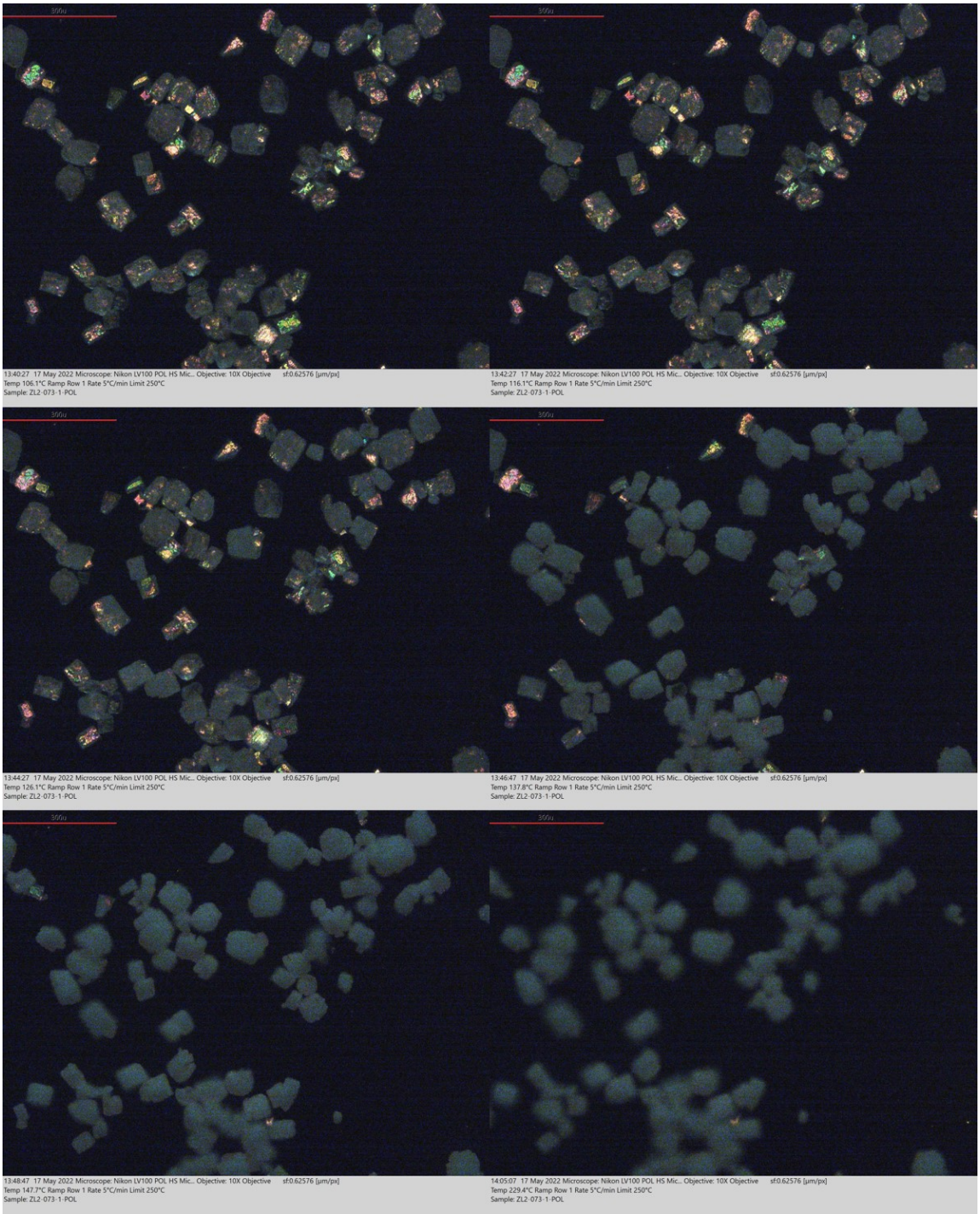

Figure 5.7: Polarized variable-temperature microscopic image of Zn-BDC-Pyrazine trial(continued)

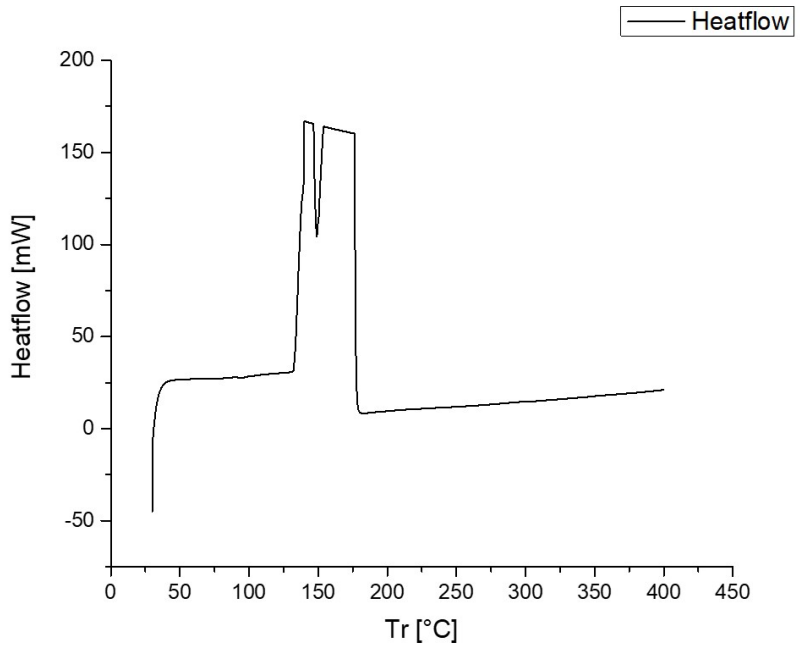

Figure 5.8: DSC curve of Zn-BDC-Pyrazine trial

5.4 Zirconium MOFs with Tetratopic Carboxylate Ligands

Another strategy is to use a tetratopic ligand to construct a MOF with **csq** or **xly** (elongated **csq**) topology. It shows same trigonal and hexagonal channels but does not require a pillar ligand. There are several MOFs reported in such topology and they showed good stability after removal of guest molecules due to strong coordination between Zr and COOH group[8], [9]. Comparing to PIZOF seriers MOFs which are also constructed from linkage between Zr and COOH, the difference is that in **csq**/**xly** topology, Zr SBU is 8-connected and ligand is 4-connected. The remaining Zr coordination sites are capped by OH group. We aim to install electric dipole to the central phenylene ring of (PEP) to construct an isoreticular MOF of SIU-75[9].

Therefore, dipolar phenylene can be polarized in plane (Figure 5.1(c)).

The fuctionalized 5′,5‴′-(2,3-difluoro-1,4-phenylenebis(ethyne-2,1-diyl))bis(([1,1′:3′,1″-terphenyl]-4,4″-dicarboxylate)) (PEP-2F) was synthesized in a similar strategy to literature[9], except that ethyl ester was used to improve solubility.

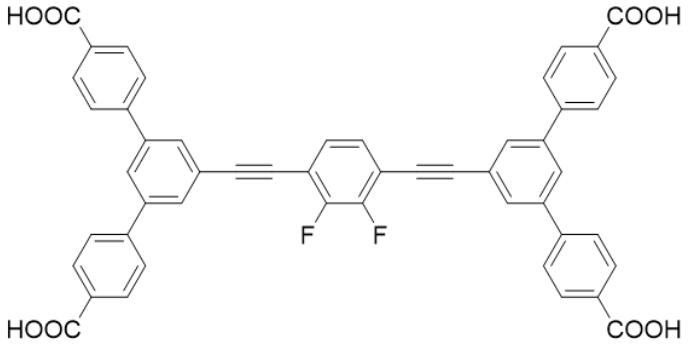

Scheme 5.2: PEP-2F ligand

While trials on synthesizing such MOFs have not been fully optimized, several conditions have shown traces of crystals. After adjusting the concentration of acetic acid, crystals could be found forming after heating(Figure 5.9). In these trials, 0.01mM PEF-2F ligand and 0.005 mM $ZrCl_4$ were dissovled in 1 mL of DEF separately. To the $ZrCl_4$ solution, 80 mg of benzoic acid was also added. Solutions from two vials were then sonicated and mixed together. Acid of 5%, 10%, 15% or 20% acetic acid were added before heated to 120 °C for 12 to 24 hours.

In further trials, by lowering concentrations and programmed heating procedures, we observed crystals with better quality. Specifically, 0.1 mL trifluoroacetic acid was added to 2.5 mL DMF solution of 0.005 mM PEP-2F ligand and 0.0025 mM $ZrCl_4$. The solution was heated to 120 °C for 6 hours and then 100 °C for 48 hours. Crystals

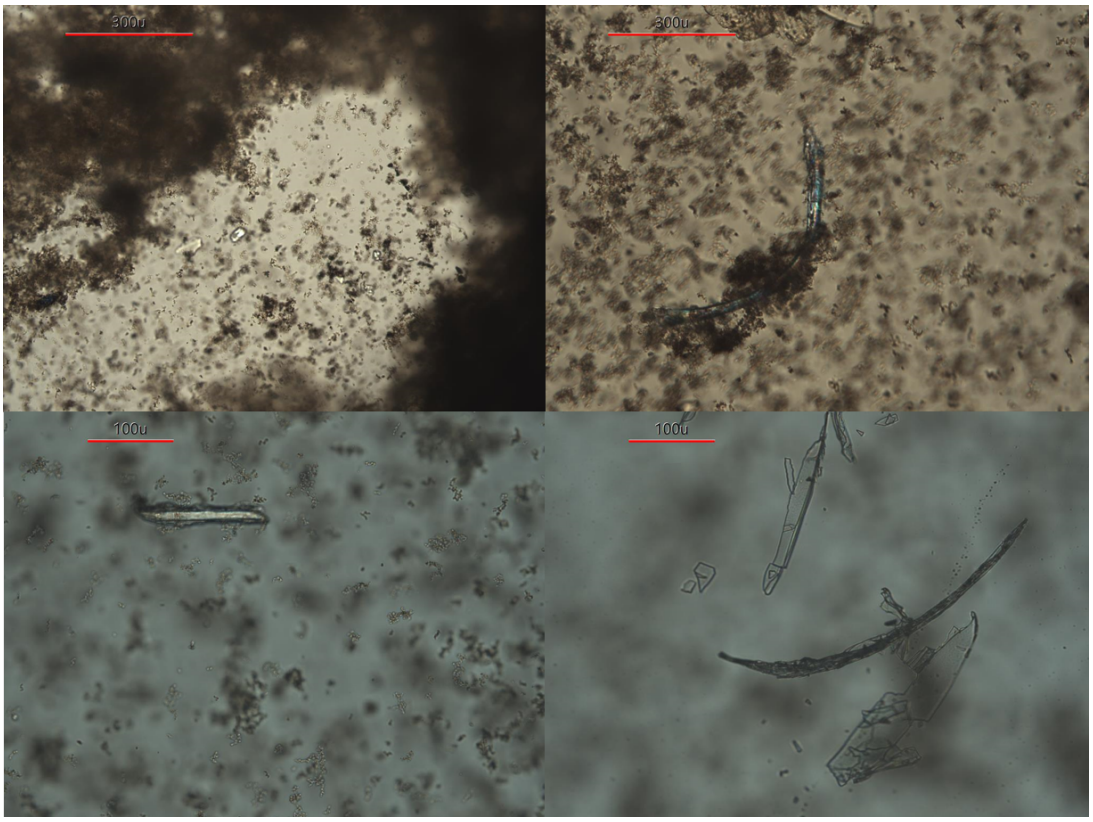

Figure 5.9: Microscopic image of possible crystals Zr-PEP-2F MOF synthesis

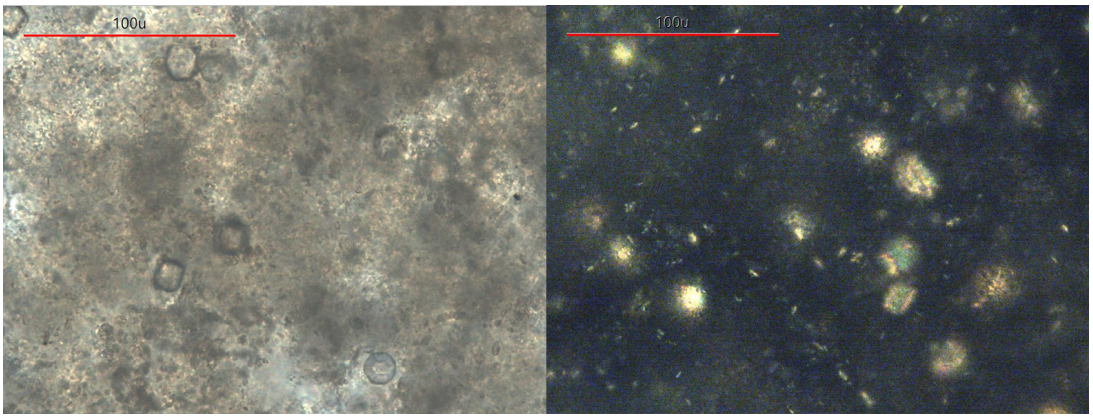

Figure 5.10: Microscopic (birefringence) image with polarization of possible crystals Zr-PEP-2F MOF synthesis synthesized at programmed heating procedure

about 10 μm are observed together with smaller crystals and amorphous impurities. Optimal activating conditions and structural analysis still require further exploration.

References

[1] S. Chen, J. Dai, and X. C. Zeng, "Metal–organic kagome lattices m 3 (2, 3, 6, 7, 10, 11-hexaiminotriphenylene) 2 (m= ni and cu): From semiconducting to metallic by metal substitution," *Physical Chemistry Chemical Physics*, vol. 17, no. 8, pp. 5954–5958, 2015.

[2] M. Fuchs, P. Liu, T. Schwemmer, *et al.*, "Kagome metal-organic frameworks as a platform for strongly correlated electrons," *Journal of Physics: Materials*, vol. 3, no. 2, p. 025 001, 2020.

[3] M. G. Yamada, T. Soejima, N. Tsuji, D. Hirai, M. Dincă, and H. Aoki, "First-principles design of a half-filled flat band of the kagome lattice in two- dimensional metal-organic frameworks," *Physical Review B*, vol. 94, no. 8, p. 081 102, 2016.

[4] J. Hungerford and K. S. Walton, "Room-temperature synthesis of metal–organic framework isomers in the tetragonal and kagome crystal structure," *Inorganic Chemistry*, vol. 58, no. 12, pp. 7690–7697, 2019.

[5] M. Kondo, Y. Takashima, J. Seo, S. Kitagawa, and S. Furukawa, "Control over the nucleation process determines the framework topology of porous coordination polymers," *CrystEngComm*, vol. 12, no. 8, pp. 2350–2353, 2010.

[6] I. Liepuoniute, C. M. Huynh, S. Perez-Estrada, *et al.*, "Enhanced rotation by ground state destabilization in amphidynamic crystals of a dipolar 2, 3-difluorophenylene rotator as established by solid state 2h nmr and dielec-

tric spectroscopy," *The Journal of Physical Chemistry C*, vol. 124, no. 28, pp. 15 391–15 398, 2020.

[7] J.-Y. Wu, S.-H. Jhan, Y.-J. Lin, D.-L. Cai, Z.-J. Hu, and H.-L. Sung, "Polymeric layer framework and chain structure of two three-component cadmium and copper phosphonates embedded with pyrazine," *Journal of Solid State Chemistry*, vol. 291, p. 121 638, 2020.

[8] W. Morris, B. Volosskiy, S. Demir, *et al.*, "Synthesis, structure, and metalation of two new highly porous zirconium metal–organic frameworks," *Inorganic chemistry*, vol. 51, no. 12, pp. 6443–6445, 2012.

[9] J. Yu, R. Anderson, X. Li, *et al.*, "Improving energy transfer within metal–organic frameworks by aligning linker transition dipoles along the framework axis," *Journal of the American Chemical Society*, vol. 142, no. 25, pp. 11 192–11 202, 2020.